



University of Naples "Federico II"

Faculty of Mathematical and Physical Sciences

Department of Physical Sciences

Secondary evolution of galaxies investigated by N-body simulations

Thesis submitted for the degree of

Doctor Philosophiae

SUPERVISORS

Prof. M. Capaccioli

Prof. L. Mayer

Dr. F. La Barbera

Dr. E. D'Onghia

CANDIDATE

Giuseppina Coppola

Contents

Abstract	viii
1 Introduction	1
1.1 The hierarchical scenario of structure's formation	1
1.1.1 Disks in the Λ CDM cosmology	6
1.1.2 Spheroids in Λ CDM cosmology	9
1.2 Gravitational encounters	11
1.2.1 Spherical Systems	12
1.2.2 Disk Systems	13
1.3 N-body simulations	13
1.3.1 Gravity	14
1.3.2 Hydrodynamics and SPH	15
1.4 The N-body codes used in the present work	17
1.4.1 The tree-code	17
1.4.2 GADGET	18
1.4.3 GASOLINE	19
2 Two-component Sérsic models of ETGs	23
2.1 Introduction	23
2.1.1 The Sérsic model	26
2.1.2 The density profile of dark-matter halos	27
2.2 Two-component Sérsic models	29
2.2.1 The de-projected Sérsic model	29
2.2.2 The dark matter component	30
2.2.3 Physical consistency and stability	31
2.3 Physical scales	33
2.4 Discrete realizations	39
2.4.1 Optimal softening length	39
2.4.2 Systems in isolation	43
2.5 The code	47
2.6 Summary	49

3	Dissipation-less merging of ETGs: scaling relations and internal color gradients	51
3.1	The models and the initial conditions of merging simulations	52
3.1.1	One-component models	53
3.1.2	Two-component models	54
3.2	Deriving the <i>observed</i> properties of merging remnants	56
3.3	Surface brightness profiles of N-body systems	58
3.3.1	Fitting the profiles with a Sérsic law	58
3.3.2	Analysis of the surface brightness profiles	59
3.4	Results	62
3.4.1	Fundamental Plane	62
3.4.2	Kormendy relation	72
3.4.3	Faber-Jackson relation	76
3.4.4	The $M_B - n$ relation	80
3.5	Internal color gradients of ETGs	82
3.5.1	Results	89
3.6	Conclusion	92
4	Disk dominated galaxies from major mergers	101
4.1	Introduction	101
4.1.1	Cold and hot accretion	103
4.2	Simulations and initial conditions	104
4.3	Results	105
4.4	Discussion and conclusion	107
5	Formation and evolution of S0's galaxies	111
5.1	Introduction	111
5.2	Formation of S0's: an overview	113
5.3	The morphology-density relation and its evolution with redshift	114
5.3.1	Tidal interactions among galaxies	116
5.3.2	Ram-pressure stripping	118
5.3.3	Strangulation	119
5.4	The morphology-density relation and its evolution with redshift	120
5.5	Our project	121
5.5.1	Numerical method and cluster identification	121
5.5.2	Substructures in hierarchical cosmological simulations	122
5.5.3	AMIGA	124
5.5.4	Following the merger tree	125
5.5.5	Defining E/S0 population	125
5.6	Preliminary results and open issues	126

Abstract

In the Λ CDM cosmology, merging is one of the most important physical processes that drives the formation and evolution of galaxies. In the present work, we use N-body techniques to investigate some of currently open issues related to the formation and evolution of galaxies along the Hubble sequence (see Chapter 1). In particular, we address (i) the role of dissipation-less merging on the scaling relations and internal color gradients of early-type galaxies, by modeling these systems with two-component Sérsic models; (ii) the formation and survival of cold disks in the merging of late-type gas-rich systems, and (iii) the different merging history of galaxy types through cosmological simulations.

We present new spherical, isotropic, non rotating, two-component (dark + stellar matter) models of early-type galaxies (see Chapter 2). In order to realistically describe the observed light profile of early-type systems and the shape of the mass profile of galaxy dark matter haloes predicted by recent numerical simulation results, both components of these models are described by a deprojected Sérsic law. We perform a detailed analysis of structural properties and distribution function of these models, proving that they represent physically admissible and stable systems. The free parameters of the models are derived from observational properties of early-type galaxies. We perform discrete realizations of the two-component Sérsic models, analyzing in detail how to derive an optimal softening length for the gravitational potential of these discrete systems. The models are then used to simulate dry mergers of early-type galaxy systems, by means of the N-body simulation code Gadget-2 (Springel 2005, see Chapter 3). The mergers are performed with progenitors spanning a wide range of galaxy luminosities and with a variety of initial orbital parameters. We find that dissipation-less merging preserves the Fundamental Plane relation of early-type galaxies, in agreement with previous works. However, in contrast to previous findings, we find that dissipation-less merging also moves galaxies along other observed correlations, such as the Kormendy, the Faber-Jackson, and the luminosity–size relations. Hence, we conclude that all the above correlations are preserved after dissipation-

less encounters of early-type galaxies. For the first time, we are also able to perform a detailed analysis of how dissipationless merging affects internal stellar population gradients of ETGs. We find that the metallicity profiles, initially assigned to the merging progenitors, can be significantly flattened after the encounters. The amount of flattening is larger for low mass-ratio mergers (down to a minor-merger ratio of 1:4), and also becomes larger as the mass of the progenitors decreases. Remarkably, this allows the existence of shallow stellar population gradients in ETGs to be explained as a result of galaxy-galaxy merging.

The second issue we have addressed is the possibility of rebuilding late-type systems starting from merging of disk galaxies. Recent pioneering works have shown that, in merger simulations with a significant stellar feedback, even a major merger can produce a disk-dominated remnant. These works show that a combination of strong stellar feedback (in very peculiar conditions) and a large gas content are essential ingredients to the survival of disks after a merging process. However, merger remnants result to have a large bulge component, which can likely describe only early spiral galaxy types. In contrast, our simulations show that disk formation through merging of gas rich systems might be an important ingredient of galaxy formation theories in more general conditions. Using realistic galaxy models (*M33*-like) whose main novelty is that of having a hot gaseous halo component (in addition to cold gas in the disk), we performed a set of hydrodynamical merger simulations. We show that mergers between these progenitors, whose baryonic component mainly consists of gas, produce late-type galaxies rather than elliptical/S0 systems. We interpret this result by the fact that gas cooling from the halo has a crucial role in producing the disk-dominated remnants. In fact, we find that gas particles in the halo have a temperature very close to the peak of the gas cooling function. Hence, the hot gas cools very rapidly after merging, acquiring angular momentum from the orbit, and settles on the final disk.

Finally, we have studied the formation and evolution of different galaxy types, with the main focus of studying the properties of S0 galaxies, in N-body cosmological simulations. From a large cosmological simulation, we have selected a cluster of galaxies with size and velocity dispersion similar to the Virgo cluster, developing an original scheme to identify elliptical, S0, and spiral galaxy candidates. With this scheme, we have derived the morphology-radius relation and the velocity distribution of galaxies in the simulated cluster at redshift $z = 0$, and compared them to observational results. The first results presented in this work show a relatively good match of the simulated and observed morphology-radius relation, but unfortunately, we also find that our simulations suffers of the low resolution problem. The number of sub-

structures that we included in the analysis is lower than that expected from the total abundance of Virgo cluster members. As a future work, we plan to re-do the analysis on different simulated clusters with improved mass and spatial resolution.

Conclusions for each part of the present work are reported at the end of each chapter of the thesis.

Chapter 1

Introduction

In the Λ -cold dark matter (Λ CDM) cosmological model, galaxy merging is an essential and inescapable process for the formation and evolution of galaxies. In this Chapter, we highlight some of the most currently debated issues arising from the comparison of model predictions to the observational picture. We start by presenting an overview of the Λ CDM cosmology (Sec. 1.1), and its prescriptions for the formation of both disk and spheroidal galaxies (Secs. 1.1.1 and 1.1.2, respectively). In particular, we discuss to what extent the model is able to reproduce the observed properties of galaxies. In Sec. 1.2, we summarize the basic physics of gravitational encounters and galaxy-galaxy merging. Since in the present work we address the complex topics of galaxy interactions by making extensive usage of numerical simulation codes, in Sec. 1.3 we shortly describe the state of the art of modern computational N-body and hydrodynamical techniques. Sec. 1.4 describes the simulation codes adopted in this work.

1.1 The hierarchical scenario of structure's formation

In a hierarchical theory of structure formation, systems like galaxies, groups and clusters of galaxies form through the continuous aggregation of non-linear objects into larger and larger units. An analytic theory for the growing of structures in a hierarchical universe was first presented by Press and Schechter (1974). Structures were assumed to grow up from random gaussian density perturbations, with non-linear clumps being identified as over-densities in the linear primordial density field. Press and Schechter (1974) argued that, if an over-density exceeds a given density threshold, δ_c , when smoothed with a top-hat filter of radius R , then the mass inside R

would be incorporated into a non-linear object of mass $M = (4/3)\pi\bar{\rho}R^3$ at later time, where $\bar{\rho}$ is the mean density of the universe at the time of collapse. For gaussian initial conditions, the probability that a given volume of the universe becomes a non-linear clump can be directly determined from the power spectrum of linear density fluctuations. Press and Schechter (1974) were able to derive the multiplicity function (also known as unconditional mass function) of non-linear objects as a function of redshift, i.e. the number of objects per unit volume in a given mass range of M to $M + dM$ at a given redshift z . A development of the Press-Schechter (PS) theory was done by Bower (1991), who derived an analytic expression for the conditional probability that material in an object of mass M_1 at redshift z_1 would end up in an object of mass M_0 at redshift z_0 (with $z_1 > z_0$). In the PS theory, dark matter haloes form from the peaks of the underlying dark matter distribution, with the formation of a given halo being independent of that of other more distant haloes. In other words, the PS theory assumes that dark matter haloes are biased tracers of the underlying dark matter distribution. Starting from this assumption, Sheth and Tormen (1999) presented a simple model to provide a relation between the abundance of dark matter haloes and their spatial distribution on large scales. Their model shows that knowledge of the unconditional mass function provides by itself an accurate estimate of the large-scale bias factor.

The PS formalism has now become a powerful tool for investigating the evolution of galaxies, groups and clusters in models of large-scale structure formation, allowing a direct comparison of theory and observations to be made for several fundamental problems of modern cosmology. We report here just a few examples. Using the PS theory, Narayan and White (1988) calculated the abundance of gravitational lenses as a function of redshift in a biased cold dark matter (CDM) universe, while Cole and Kaiser (1988) computed the Sunyaev-Zel'dovich fluctuations in the CDM cosmology. In White et al. (1993), the PS formula was used to infer the amplitude of the initial density fluctuations from the observed abundance of rich clusters of galaxies. Mo et al. (1996) showed how to constrain both the cosmic density parameter, Ω_0 , and the amplitude of cosmic mass fluctuations, σ_8^1 , from the correlation function determined by the cluster abundance and the spectrum of linear density fluctuations. By using an extension of the PS formalism, Mo and White (1996) developed an analytic model for the gravitational clustering of dark matter haloes, to understand how their spatial distribution is biased relative to that of the halo mass. Mathiesen and Evrard (1998) have examined the likelihoods of different cosmological models and cluster evolu-

¹ σ_8 is the root mean square of mass fluctuations on a scale of $8h^{-1}Mpc$.

tionary histories by comparing semi-analytical predictions of X-ray cluster number counts with the observational data from ROSAT satellite. Cluster abundance is modeled as a function of redshift by using the PS formula. Susa et al. (1994) applied the PS formalism to obtain the probability distribution function for the mass and angular momentum of over-density regions on the protogalactic scale, to investigate the formation of massive black holes at redshift $z \gtrsim 10$. All these studies show that the PS formalism provides a good framework to describe the large-scale distribution of dark matter haloes, by considering merely gravitational processes.

However, since uncondensed gas is present in both clusters of galaxies and individual galaxies, gas dissipation must have likely played an important role in structure formation. The observed sizes and luminosity functions of galaxies can be only explained by introducing gas-dynamical dissipative processes in a purely gravitational clustering scheme. Semi-analytical models of galaxy formation include a simplified physical treatment of gas cooling, star formation, supernova feedback and galaxy merging within the framework of a CDM-like initial power spectrum and the growth and collapse of fluctuations through gravitational instability. A statistical approach is used to follow individual objects and to investigate the scatter in their observed quantities. In this way, semi-analytical models allow one to explore the large parameter space of the unknowns associated to star formation rate, feedback efficiencies, initial mass function, metallicity yield and dust extinction. The first fully semi-analytical model of galaxy formation in a hierarchical universe was developed by White and Rees (1978), who derived the abundance of collapsed dark matter haloes at different redshifts. Galaxies were assumed to form by the cooling and fragmentation of residual gas within the potential well of dark matter haloes. All the gas able to cool in less than one halo dynamical time was turned into stars, with star formation efficiency being regulated by the energy injection from supernova explosion. After one dynamical time, the haloes were assumed to merge into the next level of the hierarchy while the galaxies were assumed to survive intact. All stellar populations were assigned the same mass-to-light ratio. With these quite simple assumptions, White & Rees were able to derive a galaxy luminosity function consistent with the observed one. This model was further developed by White and Frenk (1991) in the case of cold dark matter (CDM) cosmologies. White & Frenk incorporated the extended PS theory derived by Bower (1991), that allows a more appropriate statistical treatment of halo merging. The treatment of gas cooling and star formation was also improved by including a more realistic density structure of dark matter haloes and the cooling flows within them in the equation of the hydrostatic equilibrium of the gas. Feedback and chemical enrichment were included in a consistent way to model the effect of

supernova explosions on the halo gas, and the stellar population models of Bruzual A. (1983) were used to derive luminosities and colors of galaxies.

A semi-analytical model, very similar to that of White & Rees, was presented by Cole (1991), who emphasized the critical role played by feedback processes to predict a galaxy luminosity function consistent with the observations. An approach to galaxy formation in a CDM universe, similar in spirit but different in many details to that of White & Frenk, was also discussed by Lacey and Silk (1991) and Lacey and Cole (1993). Instead of adopting the Press-Schechter formalism, the authors used the statistical properties of the peaks of the initial linear density field to construct a model of halo's formation and merging. They also assumed stars to form primarily as a consequence of the response of neighboring systems to tidal forces, rather than from purely internal galaxy processes.

Semi-analytic methods are now able to reproduce quite well the distribution of galaxy properties and their correlations. For instance, models produce luminosity functions for galaxies that are similar to the observed luminosity function. In addition, galaxy properties such as luminosity, circular velocity, metallicity and colors are shown to be in good agreement with the observed ones (White and Frenk 1991). However, there are several problems still affecting all models of galaxy formation. For instance, models predict a faint-end slope of the cluster luminosity function considerably steeper than that found in most observational studies (e.g., Loveday et al. 1992). This steep slope can be overcome by invoking some mechanism to inhibit the formation of dwarf galaxies, though an unlikely strong suppression seems to be required to solve the problem. A second fundamental problem is to produce galaxies that resemble bright ellipticals. It is intrinsic to the hierarchical clustering scenario that massive, hence more luminous, objects form at later epochs. Thus, a simple expectation would be that more massive systems have younger stellar populations and bluer colors. On the contrary, massive ellipticals are observed to have red colors and old stellar populations (de Vaucouleurs 1961; Faber 1977; Burstein et al. 1984; Efstathiou and Gorgas 1985; Thomsen and Baum 1989; Peletier et al. 1990), implying that some physical process must be able to invert the expected color-luminosity trend (see Sec. 1.1.2 for a more extended discussion).

While semianalytical models try to include the complex physics of the gas component in the PS theory by using relatively simple empirical recipes, in the last fifteen years more and more efforts have also been made to improve our knowledge on the formation and evolution of the dark matter haloes themselves and the baryonic matter within.

The properties of dark matter haloes have been extensively studied by using N-body simulations of gravitational clustering. Among many impor-

tant results, numerical simulations have shown that the average density profile of CDM haloes is typically described by a universal profile. Dubinski and Carlberg (1991) described density profiles by a double power-law Hernquist (1990) model. This empirical model had an inner logarithmic slope of -1 and an outer logarithmic slope of -4 . It was introduced as an analytical approximation to the deprojected form of de Vaucouleurs (1948) profile. Navarro et al. (1997) modified this empirical law, presenting the so-called Navarro-Frenk-White model (NFW), with an outer logarithmic slope of -3 rather than -4 . Moore et al. (1999) argued that an inner logarithmic slope of -1.4 or -1.5 might also be more appropriate. For a given mass, the halo density profiles derived from N-body simulations show a scatter around all these models. This scatter depends on the halo mass accretion history, in the sense that haloes assembled earlier are more concentrated (Avila-Reese et al. 1998; Wechsler et al. 2002). Another important result of N-body simulations on the properties of dark matter halos is that the angular momentum distribution of most of CDM haloes seems to be well parameterized by a universal function. There are two competing mechanisms for the origin of the halo angular momentum, which are (i) linear tidal torques and (ii) orbital angular momentum transfer from merging satellites (Peebles 1969; Maller et al. 2002). The global spin parameter, λ , is approximately independent of the cosmology, of the mass and environment where galaxies reside (e.g., Catelan and Theuns 1996).

Numerical simulations have also been used to address directly the issue of galaxy formation, by modeling the evolution of cooling gas gravitationally coupled to the dark matter component (e.g., Carlberg et al. 1990; Cen and Ostriker 1992; Katz et al. 1992; Evrard et al. 1994; Jenkins et al. 1997). Observations show that dynamical processes involving baryons play an important role in the evolution of astrophysical systems at all length scales. In N-body simulations, stars are usually well-described as a collection of self-gravitating bodies, while the interstellar medium is described by a fluid, largely consisting of gas, that is continually depleted and replenished by the birth and death of stars. A detailed modeling of the physics of baryons within the collapsing and merging dark matter haloes is highly complex. In some cases, instead of the radiative cooling expected in the White & Frenk model, we know that turbulent dissipation dominates in a multi-phase regime, whose description in N-body codes is an extremely hard task. The process is made even more complex when dealing with gravitational fragmentation and consequent transformation of gas into stars (Hernquist and Katz 1989; Evrard et al. 1994; Springel and Hernquist 2002; Wadsley et al. 2004). Stars inject energy and momentum to the gas component producing a feedback process. The feedback regulates the star formation itself. The self-regulation may be

either at the level of the disk inter-stellar medium (hereafter ISM), where, according to the nature of the feedback, a variety of regimes appear, ranging from stationary to bursting star formation (Firmani and Tutukov 1994), or at the level of the whole intra-halo medium, giving rise to a huge hot gas halo around the galaxy (Benson et al. 2000). Star formation also undergoes a bursting regime (Firmani and Tutukov 1994), where feedback is very efficient, during the major merger of dark matter haloes. This phase can strongly change the galaxy morphological type. For example, collisions between galaxies that reside in the same dark matter halo can produce dynamically hot spheroids (Toomre 1974; Schweizer 1996; Barnes 1988; Hernquist 1990; Hernquist and Spergel 1992) in the case of colliding gas rich disk systems. Models including dissipation show that gas can lose angular momentum, the subsequent inflow of gas into the centers of the merger remnants produces a slowly rotating spheroidal stellar component, leaving objects that have essentially no disk component.

In the following sections, we explore in more detail the current picture for the formation of galaxies with different morphological types, underlying some open issues of N-body simulations.

1.1.1 Disks in the Λ CDM cosmology

The conventional theory for the origin of disk galaxies in a Λ CDM cosmology involves the dissipational collapse of gas inside relaxed dark matter haloes formed through hierarchical clustering (White and Rees 1978; Blumenthal et al. 1984). It is common to assume that the gas in a halo is shock-heated during collapse to the virial temperature. The gas then cools radiatively and falls in a free-fall time, t_{ff} , to the center. Since the seminal work by White and Frenk (1991), the infall rate of gas available for the galaxy formation is assumed to be driven either by t_{ff} , if $t_{ff} > t_{cool}$, where t_{cool} is the cooling time, or by the cooling time itself if $t_{ff} < t_{cool}$. The former case applies to haloes of masses smaller than approximately $5 \times 10^{11} M_{\odot}$, while the latter case applies to more massive haloes. The gas, originally distributed in mass and angular momentum as the dark matter halo, cools and collapses until it reaches centrifugal balance in a disk. Therefore, assuming angular momentum conservation, the radial mass distribution of the disk can be calculated by equating its specific angular momentum to the angular momentum of its final circular orbit in centrifugal equilibrium (Fall and Efstathiou 1980). The surface density profile of the disks formed within Λ CDM haloes is nearly exponential, which is a direct consequence of the angular momentum distribution acquired by the haloes by tidal torques and mergers. However, one has also to note that the profiles are expected to be

slightly more concentrated in the center with respect to the exponential law (Firmani and Avila-Reese 2000; Bullock et al. 2001). The cusp in the central disk could produce either a *photometrical* bulge (van den Bosch 2001) or a real kinematical bulge because of disk gravitational instability enhanced by the higher central surface density ² (Avila-Reese and Firmani 2000). In a few cases (high angular momentum, low-concentrated haloes), purely exponential disks can be formed.

The main success of this disk formation model is that the rotation curve of disks within collapsed Λ CDM haloes are in general consistent with observations (Mo et al. 1998; Firmani and Avila-Reese 2000; Zavala et al. 2003) and also reproduce the infrared Tully-Fischer relation and its scatter (Firmani and Avila-Reese 2003). However, there are important unsolved issues. For example, the internal angular momentum (hereafter AM) distribution inferred from observations seems to be in disagreement with the Λ CDM halo AM distribution (van den Bosch et al. 2001) and the shape of the halo profile inferred from the observed rotation curves seems not to match that of the Λ CDM haloes (Persic et al. 1996) (typically a Navarro-Frank-White profile, Navarro et al. 1997). Other studies only partially confirm these claims (Verheijen 1997; Zavala et al. 2003; Catinella et al. 2006). In N-body+hydrodynamical simulations of disk galaxy formation a further difficulty exists, usually known as the 'angular momentum catastrophe'. Simulated disks become too concentrated in the center, apparently due to AM transfer from baryons to dark matter during the gas collapse.

Toomre (1977) was among the first ones to recognize that mergers can drive the evolution of galaxy types by transforming disks into objects that resemble ellipticals. This idea was examined numerically by Barnes (1988, 1992); Hernquist and Spergel (1992) and Hernquist (1993a) in the limit where dissipational effects arising from gas dynamics are negligible, and it was shown that mergers involving equal-mass galaxies (i.e. major mergers) produce remnants with properties similar to those of ellipticals. Simulations including gas dynamics and simple prescriptions for star formation and feedback have further demonstrated that major mergers can drive gas to the center of the remnant (Barnes and Hernquist 1996), triggering starbursts with intensities similar to those observed in ultraluminous infrared galaxies (Mihos and Hernquist 1996).

While major mergers are the most dramatic example of galaxy collisions, minor mergers between galaxies of different masses are probably at least an order of magnitude more frequent (Ostriker and Tremaine 1975; Toomre 1981). Simulations have shown that dissipationless minor mergers between

²This mechanism is known as bulge secular formation

spiral galaxies and smaller companions can cause significant perturbations to disks through dynamical heating (Quinn et al. 1993; Velazquez and White 1999). Even with large mass ratios (10 : 1), if disks contain a small gas fraction ($\sim 10\%$) the damage can be severe because disks of spirals are dynamically cold (Hernquist and Mihos 1995). When it is included in the models stellar populations and star formation histories (e.g., Bender et al. 1989; Trager et al. 2000; McDermid et al. 2006), the kinematic and structural analysis of merger remnants (Schweizer and Seitzer 2007) demonstrate that most of these disks must somehow survive the merger or form very quickly thereafter from cold gas already in the disks before the merging and the hot gas in the galaxy halo. Therefore, although a large portion of a stellar disk has to be destroyed in a major merger, some fraction of the disk must survive, and the value of this fraction is a critical component for predicting many of the photometric and kinematic properties of disks as well as bulge dominated and elliptical galaxies. Moreover, minor mergers, at least those with mass ratio larger than 10 : 1 (below this value, the difference between merger and accretion becomes more and more blurred), are not generally believed to entirely destroy disks. In the Λ CDM cosmology, and as expected from the observed fractions of galaxy satellites, it is unlikely than any disk has survived $\sim 5-10$ Gyr without experiencing a merger with mass ratio larger than 10 : 1. So the question is: which kind of mergers destroy the disks and why? Simulations (Quinn et al. 1993; Hernquist and Mihos 1995; Velazquez and White 1999; Naab and Burkert 2003; Younger and Bryan 2007) and analytic arguments (Ostriker and Tremaine 1975; Toth and Ostriker 1992) suggest that gas-poor minor mergers can convert a considerable fraction of a stellar disk into bulge and cause significant perturbation (puffing up via dynamical heating) to the disk. Given the success of the Λ CDM model on large scales, and the increasing observational evidence in favour of the fact that disks do undergo (and therefore must somehow survive) a large number of mergers, it is likely that the answer lies in our (still relatively poor) understanding of disk galaxy formation. This has led to focus on the problem of forming realistic disks in a cosmological context, with a long debate on the missing elements necessary to produce disks in simulations. Various groups have argued that self-consistent treatment of gas physics and star formation along with implementation of different kinds of feedback is necessary, along with greatly improved numerical resolution (Weil et al. 1998; Sommer-Larsen et al. 2003; Governato et al. 2007; Scannapieco et al. 2008), that would enable disks to survive their destruction through violent mergers, without completely losing angular momentum and transforming into systems that are too compact and have too much bulge mass (when compared to that of observed disks) at redshift $z = 0$. It is well known (e.g., Barnes and Hernquist 1996) that

(also without any feedback mechanism) some fraction of gas can survive even in a major merger of two disks and form a new disk in the remnant. However, early studies of this mechanism were restricted to cases with low gas content (less than 10% in the progenitor disks), most of which was rapidly consumed in star formation, yielding small remnant disks within strongly bulge dominated remnants. In two seminal works, Springel and Hernquist (2005) and Robertson et al. (2006) showed that, in merger simulations with significant stellar feedback that allows the stable evolution of extremely gas rich disks (gas fraction of about one), even a major merger can produce a disk-dominated remnant. This has also been confirmed in the framework of cosmological simulations (Governato et al. 2007). Together with other recent investigations (Hopkins et al. 2008b), these works have led to the growing consensus that a combination of strong stellar feedback and large gas content is essential to the survival of disk galaxies.

1.1.2 Spheroids in Λ CDM cosmology

In the Λ CDM scenario, spheroids are expected to basically form as the result of major mergers of disks. Simulations show that these events lead to the destruction of disks when dissipative effects are neglected (Toth and Ostriker 1992; Quinn et al. 1993; Walker et al. 1996; Velazquez and White 1999). Models of galaxy collisions, including the effect of dissipation (Hernquist and Katz 1989; Barnes and Hernquist 1996), show that during merging events gas loses angular momentum because of gravitational torques. Considering an isothermal and relatively cold ISM, with a small fraction of gas in the model galaxies ($\sim 10\%$ of the total amount of baryons), Mihos and Hernquist (1996) showed that after merging the inflow of gas into the center of the merger remnant and the subsequent increase of gas density produce a roughly spherical stellar distribution, through a luminous star-burst. However, both observations and theory point towards a more complex scenario. From the observational viewpoint, the regular appearance, the dominant old stellar populations, the enhancement of α -elements and the dynamically hot structure of ellipticals seem also to be consistent with a monolithic collapse picture, whereby spheroids formed by an early ($z > 2$) single violent event, with a strong burst of star formation, followed by passive evolution of their stellar populations (Larson 1974a,b; Carlberg 1984). In order to distinguish between the monolithic and hierarchical scenario, it is crucial to determine the formation epoch of spheroids. There are at least two ways of defining such epoch, (1) as the time when most of the stars formed and (2) as the epoch when the stellar component acquired its dynamical properties through violent or secular processes. For the monolithic collapse mechanism

both epochs coincide (Larson 1974b). In the hierarchical scenario, if major mergers occur at high redshifts, when disks are mostly gaseous, then the formation process of the spheroid is close to that of the monolithic collapse. On the other hand, if major mergers occur at later epochs, when galaxies have already transformed a large fraction of their gas into stars, then spheroids assemble by the "classical" dissipationless collision (Avila-Reese 2006).

Besides that, stellar disks may develop spheroids in their centers (bulges) by secular evolution mechanisms, both intrinsic or enhanced by minor mergers and interactions. This channel of spheroid formation should work for late-type galaxies and it is supported by a wealth of observational results (Kormendy and Kennicutt 2004). The picture is even more complex, as galaxy morphology may be continuously changing, depending on the mass accretion history (smooth accretion and violent mergers) and the environment where galaxies reside. A spheroidal galaxy, that formed earlier in the past, should continually accrete gas, with a new younger disk growing around the galaxy itself. Hence, a naive expectation of the Λ CDM scenario would be that massive elliptical galaxies should assemble at later times. It is also expected that disks in galaxies with small bulge-to-disk ratios should be on average redder than those of galaxies with large bulge-to-disk ratios, with this expectation being not confirmed from observations (Avila-Reese 2006).

Though still matter of debate, a more complex picture of spheroidal formation emerged in the past few years, that seems to fit well reconcile observations with the Λ CDM model (e.g., Silk and Rees 1998; Firmani and Avila-Reese 2003; De Lucia et al. 2006). The basic idea is that massive ellipticals formed earlier ($z \sim 3$) and in a short timescale by the merging of gas-rich disks in rare high-peak, clustered regions of the Universe. The complex physics of the merging implies (i) an ultraluminous burst of star-formation obscured by dust (cool ULIRG phase) and the establishment of a spheroidal structure, (ii) gas collapse to the center, which favors the growth of pre-existing massive black holes through an Eddington or even super-Eddington regime (warm ULIRG phase), (iii) switching on of the AGN activity associated to the supermassive black hole above a critical mass, reverting the gas inflow to a gas outflow (QSO phase), (iv) switching off of the AGN activity leaving a giant stellar spheroid with a supermassive black hole in the center and a hot gas corona around (passive evolution phase). In other terms, the energy injected from AGN in the form of radio jets provides the feedback necessary to prevent any further cooling flow into the spheroid. This picture solves the problem of disk formation around elliptical galaxies in the field, as well as the overly extended bright end in the galaxy luminosity function predicted by semianalytical models (Firmani and Avila-Reese 2003; De Lucia et al. 2006). Massive elliptical galaxies are already in place at high redshifts,

while less massive galaxies (collapsing from more common density peaks) assembled later. This model is known as the downsizing or anti-hierarchical galaxy formation picture. Despite of its name, this picture fits well within the hierarchical Λ CDM framework.

Recent observations have shown that an important channel for the formation of massive elliptical is that of mergers between galaxies which are already on the red sequence (van Dokkum et al. 1999; Bell et al. 2006; van Dokkum 2005; Tran et al. 2005). These so-called *dry* mergers are now thought to be the dominant mode of growth of massive ($> \text{several } M_*$) galaxies at $0 < z < 1$, building up the high-mass end of the mass function but not changing the overall mass density of ellipticals (see Chapter 2, Sec. 2.1 for a more extended discussion).

1.2 Gravitational encounters

Since this thesis work is aimed at analyzing merging processes of late- and early-type galaxies, we provide here a short summary of the basic mechanisms governing the physics of mergers. Gravitational interactions among galaxies are by far more common in the Universe than one may think. Far from being isolated systems, galaxies form and evolve by interacting with both their environment and neighboring systems. Gravitational interactions can produce distortions in the disk component of galaxies, giving rise to spiral arms, tidal tails and producing bursts of star formation. The morphology of the galaxy can thus be heavily perturbed, even if the tides are not locally catastrophic. For instance, our Galaxy is interacting with the Magellanic Clouds and it is thought that this interaction was at its peak of intensity about one billion years ago.

During an encounter, the kinetic energy associated with the relative motion of galaxies diminishes, because the internal energies increase. If the initial relative speed of the interacting systems is larger than the escape velocity, v_f , the galaxies reach the point of closest approach with sufficient orbital energy to escape to infinity, otherwise they merge. If the initial speed is much larger than v_f the encounter alters both the orbits and the internal structure of the galaxies only slightly.

Apart from some specific systems (see (Sridhar and Nityananda 1990)), analytic description of encounters among galaxies are possible only in two cases, where perturbation theory can be applied. One of such cases arises in fast encounters (impulse approximation), another one is that of encounters among galaxies of very different masses (dynamical friction approximation). On the contrary, when two galaxies of similar mass collide, at a speed comparable

with the internal velocities of the two systems (slow encounters), the only effective way of analyzing in detail the interaction is that of simulating the encounter numerically, using a suitable N-body code. Numerical simulations show that these encounters often lead to the merging of the two systems. In the next two sections, we shortly describe the physical mechanisms involved in the merging process, considering the cases where progenitors are either spheroidal or disk systems.

1.2.1 Spherical Systems

The simplest N-body model of galaxy merging is the encounter of a pair of spherical systems. In head-on collisions, merging results from the gravitational compression arising when the two galaxies nearly coincide and that causes a slightly greater axial force to be felt between them (Toomre 1974; White 1979; Miller and Smith 1980). By stirring up the material in each galaxy at the expense of their orbital energy, this mechanism determines the rapid merger of even the most centrally concentrated systems in only a few passages. In off-axis collisions, the collective response is dominated by those particles whose orbits lie along the same direction as the passage of two galaxies (White 1978, 1979; Roos and Norman 1979). Such particles are promoted onto less-bound orbits, receiving both energy and angular momentum from the relative motion of the two galaxies, and producing broad tail-like structures. The merging is found to depend strongly on the rotational properties of the galaxies involved. It is more rapid if their spin vectors are aligned with that of their orbit, and it is very slow if this alignment is reversed (White 1979).

Fluctuating gravitational fields during the merging process tend to transfer binding energy between different components of the system, but such fluctuations damp down before a complete redistribution takes place. Therefore, the centers and outskirts of merger remnants tend to remain dominated by particles from the respective centers and outskirts of the interacting galaxies. After a merger, the remnant relaxes progressively outward on a time-scale comparable to the local crossing time. The amount of material which escapes during the merger depends on the structure of the interacting galaxies as well as the parameters of their encounter. In general, the escaping stuff comes from the outskirts of the original galaxies. The material which does not quite escape eventually phase-mixes to form an extended envelope around the body of the remnant, characterized by an r^4 density profile (Jaffe 1987; White 1987).

Mergers of spherical galaxies produce remnants with fairly simple shapes and kinematics (White 1983). Head-on encounters result in prolate rem-

nants with anisotropic velocity dispersions, whereas if the encounter is not quite head-on, the result is a slowly-tumbling triaxial object.

1.2.2 Disk Systems

Mergers between disk galaxies embedded in a dark matter halo were presented by Gerhard (1981); Farouki and Shapiro (1982); Negroponete and White (1983); Barnes (1988, 1992). Moreover, Gerhard (1983); Gerhard and Fall (1983) and Barnes (1989) discussed models in which several disk/halo galaxies merge sequentially.

The dynamics of encounters between such galaxies is largely governed by interactions of their extended dark matter haloes. Hence, even passages where the visible components completely miss each other can lead to rapid orbital decay. The orbital angular momentum of the two haloes is transferred to internal degrees of freedom, imparting spin and creating broad tidal tails. The embedded disks and/or bulges are not much braked by the tidal forces, instead these components loose orbital angular momentum mostly by interacting with their own surrounding haloes, once the latters have been decelerated (Barnes 1992).

As in mergers of spherical systems, the incomplete violent relaxation of disk/halo models only blurs the original ordering in binding energy; the tightly-bound components which contained most of the luminosity in the original galaxies will be found near the center of the merger remnant. Luminous material dominates the central regions of merger remnants because the dense luminous parts of the infalling galaxies remain largely undisturbed until they finally encounter each other and merge within a now-common envelope of halo material (Barnes 1988).

The shapes and kinematics of the remnants of disk galaxy mergers are much more complex than those produced by mergers of spherical systems (see Sec. 1.1.1).

1.3 N-body simulations

Much of our present understanding of galactic dynamics has emerged from numerical models of galaxies and their interactions, which is the main subject of this thesis work. In the next sections, we thus focus on the computational modelling of gravity and we describe the most commonly adopted N-body techniques.

1.3.1 Gravity

The dynamics of a system with N gravitationally interacting particles is completely described from the Newton's law plus, eventually, the presence of an external potential field, ϕ_{ext} . The force \vec{F}_i , acting on particle i with mass m_i and position \vec{r}_i , is:

$$\vec{F}_i = - \sum_{j \neq i} G \frac{m_i m_j (\vec{r}_i - \vec{r}_j)}{|\vec{r}_i - \vec{r}_j|^3} - \vec{\nabla} \cdot \phi_{ext}(\vec{r}_i), \quad (1.1)$$

where G is the gravitational constant. In order to find the position of each particle, one has to solve a set of non-linear second order ordinary differential equations relating the acceleration, $\partial^2 \vec{r}_i / \partial t^2 = \vec{F}_i / m_i$, with the position of all the particles in the system. Once a set of initial conditions is specified (for example the initial positions \vec{r}_i and velocities \vec{v}_i for all particles) it exists a unique solution. It is well known that the solution is analytical only for the two body problem, while larger N requires numerical integration. However, special care must be taken to ensure accuracy in the calculation. In fact, the gravitational force is singular when the distance of two particles approaches 0, which can lead to estimate arbitrarily large relative velocities. The singularity may be avoided by introducing a smoothing length in Eq. 1.1 (Aarseth 1963), that modifies the gravitational interaction at small scales:

$$\vec{F}_i = - \sum_{j \neq i} \frac{G m_i m_j (\vec{r}_i - \vec{r}_j)}{(|\vec{r}_i - \vec{r}_j|^2 + \epsilon^2)^{3/2}}, \quad (1.2)$$

where $\epsilon > 0$ is the softening, or smoothing length, that is a typical distance below which the gravitational interaction is suppressed. To minimize errors in the force computation and the global impact of the softening for distances larger than ϵ itself, finite size kernels are also adopted, with the advantage that the smoothed force has continuous derivatives (Dehnen 2001). This strategy effectively suppresses binary formation and strong gravitational interactions, at the price of slightly altering the dynamics of the system.

N -body simulations demand some computational expense for computing the force acting on each particle of the system. If we consider a set of N particles, we have that the N th particle is acted upon by the remaining $(N - 1)$ particles. Following this direct computation scheme, the amount of computational time required for force estimation is of the order $N^2 - N$, i.e. $\mathcal{O}(N^2)$. Early N -body works used up to 100 particles (Aarseth 1963) and they adopted a direct summation of all the forces exerted on each particle from all the remaining bodies. This direct $\mathcal{O}(N^2)$ approach is impractical for large numbers of bodies. Hence, this technique allows only a rather limited number of particles ($\lesssim 10^4$) to be described. Different strategies can be adopted in order

to achieve a compromise between numerical resources and number of particles. Three main prescriptions exist for evaluating the gravitational force: the particle-mesh (PM), the particle-particle-particle mesh (P3M) and the tree-code schemes. The PM method has been longly used in electrostatics and plasma physics. The gravitational potential of the system is built over a grid starting from the density field and by solving the associated Poisson equation. Particles do not interact directly with each other but only through a mean field. The method solves the Poisson equation on the mesh, calculating the force field from the mesh-defined potential and interpolating the force on the grid to find the force exerted on each particle. The Poisson equation is typically solved using a Fast Fourier Transform algorithm. The main advantage of the PM methods is the improved computation speed, which is of the order $\mathcal{O}(N + N_g \log N_g)$ where N_g is the number of points on the grid. The main drawback is that the PM approach does not build up an adaptive grid, and thus it is not suitable for applications with highly inhomogeneous density distributions and/or very violent dynamical processes.

The P3M method solves this major problem, by coupling a mean field description on large scales with a direct, softened, treatment of the gravitational interactions on distances of the order of or below a few grid spacing. The main drawback of the P3M method is that in presence of strong clustering a large number of particles will interact directly, slowing down significantly the computation to $\mathcal{O}(N^2)$. This problem can be resolved by using adaptive meshes, so that the spatial resolution is refined in regions of high density. Adaptive P3M codes have a computational cost which scales as $\mathcal{O}(N \log(N))$. The tree code method (Barnes and Hut 1986) provides a fast, general integrator for collisionless systems, when close encounters can be neglected and the force contribution from very distant particles does not have to be computed with high accuracy. Small scale, strong interactions are typically softened, while the potentials due to distant groups of particles are approximated by multipole expansions about the group centers of mass. The resulting computation time scales as $\mathcal{O}(N \log(N))$ but the approximations introduce small force errors. Typical implementations of the tree code expand the potentials to quadrupole order and construct a tree hierarchy of particles using a recursive binary splitting algorithm (see Sec. 1.4.1 for details).

1.3.2 Hydrodynamics and SPH

Baryonic matter (stars and gas) in astrophysical systems experiences simultaneously high-energy processes and gravity. Smoothed particle hydrodynamics (SPH) was just invented to simulate this kind of phenomena in astrophysics (Lucy 1977; Gingold and Monaghan 1977). Generally speaking,

SPH is used to model hydrodynamic flows, including possible effects of gravity, by incorporating other astrophysical processes which may be important, such as radiative transfer and magnetic fields.

The SPH method works by dividing the fluid into a set of discrete elements, referred to as particles. These particles have a spatial distance (known as the smoothing length, typically represented in equations by the symbol h), over which their properties are *smoothed* by a kernel function. This means that any physical quantity of any particle can be obtained by summing the relevant properties of all the particles which lie within the range of the kernel. The contributions of each particle to a property are weighted according to their distance from the particle of interest, and their density. Mathematically, this is governed by the kernel function W . Kernel functions commonly used include the Gaussian function and the cubic spline. The latter function is exactly zero for particles further away than two smoothing lengths (unlike the Gaussian, where there is a small contribution at any finite distance away). This has the advantage of saving computational effort by not including the relatively minor contributions from distant particles. Unlike the particle in cell method, SPH does not need a grid to calculate spatial derivatives. The equation for any quantity f at any point \mathbf{r} is given by the equation

$$f(\mathbf{r}) = \sum_j m_j \frac{f_j}{\rho_j} W(|\mathbf{r} - \mathbf{r}_j|, h), \quad (1.3)$$

where m_j is the mass of particle j , f_j is the value of the quantity f for particle j , ρ_j is the density associated with particle j , \mathbf{r} denotes position and W is the kernel function mentioned above. For example, the density of particle i can be expressed as:

$$\rho_i = \rho(\mathbf{r}_i) = \sum_j m_j \frac{\rho_j}{\rho_j} W(|\mathbf{r}_i - \mathbf{r}_j|, h) = \sum_j m_j W(\mathbf{r}_i - \mathbf{r}_j, h), \quad (1.4)$$

where the summation over j includes all particles in the simulation. Similarly, the spatial derivative of a quantity can be obtained by using integration by parts to shift the ∇ operator from the physical quantity to the kernel function,

$$\nabla f(\mathbf{r}) = \sum_j m_j \frac{f_j}{\rho_j} \nabla W(|\mathbf{r} - \mathbf{r}_j|, h). \quad (1.5)$$

By assigning each particle its own smoothing length and allowing it to vary with time, the resolution of a simulation automatically adapts itself depending on local conditions of the fluid. For example, in a very dense region

where many particles are close together the smoothing length can be made relatively short, yielding high spatial resolution. Conversely, in low-density regions individual particles are far apart and the resolution is low, optimizing the computation for those regions.

Often in astrophysics, one wishes to model self-gravity in addition to pure hydrodynamics. The particle-based nature of SPH makes it an ideal tool to be combined with a particle-based gravity solver, such as, for instance, PM, P3M, and Tree-Code. Hybrid codes, combining SPH and particle-based gravity solver are also known as TreeSPH codes.

1.4 The N-body codes used in the present work

In this thesis work, collisionless and hydrodynamical N-body simulations are performed, by using two simulation codes, GADGET-2 and GASOLINE. Both these code are TreeSPH. In this section, we start by providing some details about Tree-codes (already mentioned in Sec. 1.3.1) and then we discuss the key characteristics of GADGET-2 and GASOLINE.

1.4.1 The tree-code

In a tree-code force computation is based on a hierarchical subdivision of space in cubic cells (Barnes and Hut 1986). The *tree* is obtained by starting from a root cell (a cube containing all the N particles), and subdividing it in n cubic sub-cells with half the size of the parent cell. Empty cells are excluded from the tree. Cells with more than one particle are recursively divided in n sub-cells. Cells with only one particle are the leaves of the tree. The gravitational field at a given point is computed considering the exact contribution of the closest leaves by direct summation, and the approximated contribution of sufficiently distant cells by using multipole expansion. As a result of this tree technique, the cost of force computation scales as $O(N\log N)$, resulting remarkably less time consuming than $O(N^2)$ algorithms based on direct summation.

The force between individual particles is smoothed by introducing the standard Plummer softening, i.e., the softened potential produced at a distance r by a particle of mass m :

$$\Phi(r) = -\frac{Gm}{\varepsilon} g_{pl} \left(\frac{r}{\varepsilon} \right), \quad (1.6)$$

where m is the particle mass, r is the mutual distance between the two particles, and the smoothing parameter ϵ is the softening length, and

$$g_{pl}(x) = \frac{1}{(1+x^2)^{1/2}} \quad (1.7)$$

is the Plummer softening kernel.

The concept of sufficiently distant cells, introduced to choose between an approximated and exact force computation, is quantified by adopting an opening criterion that depends on a single dimensionless parameter, θ , the so-called *opening angle*. Let us consider the interaction between a cell of size l and a particle at a distance D from the center of mass of the cell. If:

$$\frac{l}{D} < \theta \quad (1.8)$$

the force exerted by the cell on the particle is calculated with the multipole expansion. Otherwise, the cell is opened and is split in its n sub-cells, which are recursively analyzed with the opening criterion.

1.4.2 GADGET

GADGET-2 Springel (2005) is a simulation code capable of following a collisionless fluid computing gravitational interactions with a hierarchical multipole expansion, and an ideal gas by means of smoothed particle hydrodynamics (SPH) on massively parallel computers. GADGET-2 is a TreeSPH code (Barnes and Hut 1986) where only short-range forces are computed with the tree method while long-range forces are determined with Fourier techniques. In the present work (see Chapter 3), we use GADGET-2 only for dissipationless simulations of interacting galaxy systems with no gas. We mention here only the characteristics of the code which are relevant for the our applications.

The Newtonian gravity is corrected with a cubic spline softening (see 1.6) where the smoothing kernel $g_{spl3}(x)$ is given by:

$$g_{spl3}(x) = \begin{cases} x^2 \frac{16}{3} + \frac{48}{5}x^4 - \frac{32}{5}x^5 + \frac{14}{5}, & (0 \leq x \leq \frac{1}{2}); \\ x^{-1} \frac{1}{15} - \frac{32}{3}x^2 + 16x^3 - \frac{48}{5}x^4 + \frac{32}{15}x^5 + \frac{16}{5}, & (\frac{1}{2} \leq x \leq 1); \\ x^{-1}, & x \geq 1. \end{cases} \quad (1.9)$$

By definition the spline softened potentials are exactly Newtonian for $r \geq h_3$. One has also to note that, owing to their different definitions, the spline softening length, h_3 , and the Plummer softening length, ϵ , are not directly comparable. A Plummer softening length equivalent to a given spline softening

h_3 can be defined, for example, by imposing that the minimum of the potential is the same in the two cases. For the cubic spline kernel, this happens for $\epsilon = h_3/2.8$.

In regards to the multipole order expansion, GADGET-2 uses monopole moments, since they have several advantages with respect to schemes that carry the expansions to higher orders. First of all, gravitational trees with monopole moments can be constructed in an extremely memory efficient way. (Springel 2005).

For what concerns the cell-opening criterion, GADGET-2 usually adopts a relative opening criterion tuned for the use of monopole moments. In particular, a node of mass M and extension l at distance r is considered if:

$$\frac{GM}{r^2} \left(\frac{l}{r}\right)^2 \leq \alpha |\mathbf{a}|, \quad (1.10)$$

where $|\mathbf{a}|$ is the size of the total acceleration obtained in the last time-step, and α is a tolerance parameter. This criterion tries to limit the absolute force error introduced in each particle node interaction by comparing a rough estimate of the truncation error with the size of the total expected force. As a result, the typical relative force error is kept roughly constant, and if needed, the opening criterion adjusts to the dynamical state of the simulation to achieve this goal. The opening angle varies with the distance of the node. The net result is an opening criterion that typically delivers higher force accuracy at a given computational cost compared to a purely geometrical criterion.

1.4.3 GASOLINE

For the hydrodynamical simulations presented in this thesis we used the code GASOLINE, (Wadsley et al. 2004). GASOLINE, a parallel N-body and gasdynamics code, is built on PKDGRAV framework (Stadel 2001) and it is fundamentally a tree code. Stadel (2001) designed PKDGRAV from the start as a parallel code and departing significantly from the original N-body tree code designs of Barnes and Hut (1986) by using 4th (hexadecapole) rather than 2nd (quadrupole) order multipole moments to represent the mass distribution in cells at each level of the tree. This results in less computational expensive for the same level of accuracy: better pipelining, smaller interaction lists for each particle and reduced communication demands in parallel. The current implementation in Gasoline uses reduced moments that require only $n + 1$ terms to be stored for the n th moment.

The local gravity tree is built by recursively bisecting the longest axis of each

cell which keeps the cells axis ratios close to one. At each level the dimensions of the cells are squeezed to just contain the particles. This overcomes the empty cell problem of un-squeezed spatial bisection trees.

Gasoline calculates the gravitational accelerations using the treewalking procedure of the Barnes and Hut (1986) algorithm, except that it collects interactions for entire buckets rather than single particles. This amortizes the cost of tree traversal for a bucket over all its particles. In the tree building phase, Gasoline assigns to each cell of the tree an opening radius about its center of mass. This is defined as,

$$r_{open} = \frac{2B_{max}}{\sqrt{3}\theta} \quad (1.11)$$

where B_{max} is the maximum distance from a particle in the cell to the center of mass of the cell. The opening angle, θ , is a user specified accuracy parameter which is similar to the traditional θ parameter of the Barnes-Hut code; notice that decreasing θ in equation 1.11, increases r_{open} .

As mentioned in section 1.3.2 the basis of the SPH method is the representation and evolution of smoothly varying fluid quantities whose value is only known at disordered discrete points in space occupied by particles. Particles are the fundamental resolution elements comparable to cells in a mesh. The smoothing operation provides a basis from which to obtain derivatives. Thus, estimates of density related physical quantities and gradients are generated. The summation aspect led to SPH being described as a Monte Carlo type method (with $O(1/\sqrt{N})$ errors) however it was shown by Monaghan (1985) that the method is more closely related to interpolation theory with errors $O((\ln N)^d/N)$, where d is the number of dimensions.

Gasoline uses the kernel-average first suggested by Hernquist and Katz (1989),

$$W_{ij} = \frac{1}{2}(|\vec{r}_i - \vec{r}_j|/h_i) + \frac{1}{2}(|\vec{r}_i - \vec{r}_j|/h_j). \quad (1.12)$$

Gasoline employs a fairly standard implementation of the hydrodynamics equations of motion for SPH (Monaghan 1992). Density is calculated from a sum over particle masses m_j ,

$$\rho_i = \sum_{j=1}^n m_j W_{ij}. \quad (1.13)$$

The momentum equation is expressed,

$$\frac{d\vec{v}_i}{dt} = - \sum_{j=1}^n m_j \left(\frac{P_i}{\rho_i^2} + \frac{P_j}{\rho_j^2} + \prod_{ij} \right) \nabla_i W_{ij}, \quad (1.14)$$

where P_j is pressure, \vec{v}_i velocity and the artificial viscosity term \prod_{ij} . The pressure averaged energy equation conserves energy exactly in the limit of infinitesimal time steps but may produce negative energies due to the P_j term if significant local variations in pressure occur. Gasoline employs the following equation (advocated by Evrard 1988, Benz 1989) which also conserves energy exactly in each pairwise exchange but is dependent only on the local particle pressure,

$$\frac{du_i}{dt} = \frac{P_i}{\rho_i^2} \sum_{j=1}^n m_j \vec{v}_{ij} \cdot \nabla_i W_{ij}, \quad (1.15)$$

where u_i is the internal energy of particle i , which is equal to $1/(\gamma - 1)P_i/\rho_i$ for an ideal gas. In this formulation entropy is closely conserved making it similar to alternative entropy integration approaches such as that proposed by Springel and Hernquist (2002).

In astrophysical systems the cooling timescale is usually short compared to dynamical timescales which often results in temperatures that are close to an equilibrium set by competing heating and cooling processes. In Gasoline a range of cases including adiabatic (no cooling), isothermal (instant cooling), and implicit energy integration are implemented. Hydrogen and Helium cooling processes have been incorporated. Ionization fractions are calculated assuming equilibrium for efficiency. Gasoline optionally adds heating due to feedback from star formation, a uniform UV background or using user defined functions. The star formation algorithm is similar to the one proposed in (Katz et al. 1992) and extended in (Katz et al. 1996). They apply criteria to determine which gas particles are eligible to form stars. They then determine which gas particles actually form stars probabilistically such that on average they reproduce a star formation rate formula similar to a Schmidt law (Schmidt 1959). Those gas particles that actually form stars spawn a new star particle of a predetermined mass, reducing their own mass. The new star particle is created with the same velocity, position, and metallicity as its parent gas particle. Star particles can add energy, mass and metals back to gas particles through feedback processes including type II and Ia supernova and stellar winds (Katz et al. 1992, 1996). The energy is added gradually with an exponential decay rate of 20 Myr. It is added at the location of the parent gas particle and is smoothed using the SPH smoothing kernel. Since this thermal energy is typically added to very dense gas, it is quickly radiated away and has little effect on the evolution of the galaxy. Stinson et al. (2006) describe a stronger and perhaps more realistic method for including type II supernovae (SNII) feedback. In order to account for the non-thermal energy budget of the ISM, in this model the timescale during which cooling is shut

off is self-consistently calculated based on a sub-grid model of the blast-wave produced by a supernova explosion. By temporarily preventing the cooling of the hot phase created by supernovae feedback this type of methods naturally produces a two-phase medium with hot bubbles triggered by supernovae explosions ($T > 10^5 K$) surrounded by a colder, filamentary phase ($T \sim 10^4 K$). The radius of the blast-wave as a function of time can be directly computed from the local physical parameters of the ISM. In the numerical implementation such radius defines the size of the volume of gas particles that are unable to cool during the adiabatic phase. The adiabatic phase lasts of order $30 Myr$, after which radiative losses would become efficient and the gas is again allowed to cool radiatively. The blast-wave feedback model has only one free parameter, the efficiency of supernovae feedback, namely what fraction of the energy generated by the supernovae explosions is damped to the gas. In addition (Stinson et al. 2006) also include feedback from type Ia supernovae and stellar winds from planetary nebulae and allow the metals produced in stars to be distributed. The feedback contribution of stellar winds is also significant. Stars with masses below $8 \times M_{\odot}$ return substantial fractions of their mass to the ISM as they evolve and leave behind white dwarf remnants. They base their wind feedback on the work of Kennicutt et al. (1994) who find that the total stellar return fraction is 0.25 to 0.50 of the initial mass depending on the IMF. Because the return rate is so high, this form of feedback can greatly prolong star formation in galaxies without gas inflow. For simplicity, they consider only stars between 1 and $8 M_{\odot}$ and assume that lower mass stars remain uninvolved. To determine the fraction of mass returned for a given stellar mass they use the initial-final mass relation of Weidemann (1987) and then fit his results to a continuous function.

Chapter 2

Two-component Sérsic models of early-type galaxies

We present two-component models of early-type galaxies, consisting of stellar and dark-matter components that follow the de-projected Sérsic law. The models describe spherical, non-rotating, isotropic systems, and their physical parameters (scaling radii and total masses) are uniquely defined by the total B-band luminosity. We describe in detail how the models are constructed, and show that the distribution function is non-negative defined, implying that the models are stable against radial and non-radial perturbation. Discrete model realizations, performed with the software Gadget-2, show that all the model properties remain stable over at least 5 Gyr s. For each model, we are able to define an optimal smoothing length, defined as the softening parameter that minimizes the rms of differences between the true and discrete gravitational potentials. The software code, that is used to realize the models, will be made publicly available. The models are primarily intended as a tool to analyze the effects of dissipationless merging on the internal properties and scaling laws of early-type galaxies (see Chapter 3).

2.1 Introduction

Recent observations have provided evidence in favour of a picture whereby ETGs continuously assemble through mergers between galaxies which are already on the red sequence (van Dokkum et al. 1999; Bell et al. 2006; van Dokkum 2005; Tran et al. 2005). These so-called *dry* mergers are now thought to be the dominant mode of growth of massive ($> M_*$) galaxies at $0 < z < 1$, building up the high-mass end of the mass function but not changing the overall mass density of ellipticals. According to the hierarchical scenario,

star formation and mass assembly are not necessarily concomitant processes in early-type galaxy (ETG) formation: stars may well have formed at very high redshift in relatively small units, but only at lower redshift (e.g., $z \lesssim 1$) they may have merged together to build the massive ETGs that we see in the $z \sim 0$ Universe. According to this scenario Khochfar and Burkert (2003) analyzed the progenitors of present-day ETGs selected from their bulge-disk stellar mass fraction. They found that a large fraction of ETGs are likely formed by the merging between bulge-dominated systems and that the fraction of spheroidal mergers increases with luminosity, suggesting that massive ETGs mainly formed by nearly dissipationless mergers.

Only recently, with the advent of wide-field surveys it has been feasible to reduce the strong variance which affects ETG studies, and place more tight constraints on the evolution of ETGs. Some observational results favour little evolution of these systems. For instance, the VIMOS VLT Deep Survey show that the luminosity function of ETGs is consistent with passive evolution up to $z \sim 1.1$ and the number of bright ETGs decreases by $\sim 40\%$ from $z \sim 0.3$ to $z \sim 1.1$ (Zucca et al. 2006). K-band selected surveys revealed a substantial population of old massive, passively evolving, ETGs at $1 < z < 2$ and showed that their total luminosity and stellar mass function evolve only weakly to $z \sim 0.8 - 1$ (Cimatti et al. 2002; Bundy et al. 2006).

On the other hand, the COMBO-17 (Bell et al. 2004) and DEEP2 (Faber et al. 2005) surveys indicate a stronger evolution of the ETG population characterized by a faster decrease of the number density with redshift. The red sequence of ETGs becomes progressively bluer in the rest frame $U - V$ color, going from $z = 0$ to $z = 1$, consistent with pure passive evolution of stellar populations formed at high redshift (Bell et al. 2004). However, Bell et al. (2004) and Faber et al. (2005) also found that the stellar mass in red sequence ETGs was nearly doubled since $z \sim 1$ to $z \sim 0$ and argued in favour of a major role of ETG-ETG merging (dry merging) in the build up of the ETG population. In agreement with these results, by using SDSS spectroscopic data, Masjedi et al. (2008) found significant evolution in the luminosity function of red galaxies since redshift $z \sim 1$. Recently Whitaker and van Dokkum (2008), analyzing HST images of ongoing mergers and merger remnants at $z \sim 0.1$, also found that red mergers in the nearby universe mostly involve early-type galaxies containing very little cold gas and substantial amounts of hot gas. It appears that this gas is not able to condense and form stars, even during mergers. De Lucia et al. (2006), using semi-analytical models, investigated the predicted number of progenitors as a function of galaxy stellar mass. They found that more massive galaxies are made up of several stellar pieces, with the number of effective progenitors being less than two up to stellar masses of $\simeq 10^{11} M_{\odot}$, increasing up to \sim five mergers for the

most massive galaxies. This indicates that, at adds with massive systems, the formation of low mass systems typically involves only a small number of major mergers.

Since dissipation-less merger might be the most important physical mechanism to form ETGs, it is of fundamental importance to model dissipation-less merging between spheroidal systems and to analyze the properties of merger remnants, in order to see if these predicted properties match the observational scenario. ETGs are known to follow well-defined empirical correlations (scaling-laws) that relate their global observational properties, such as the total luminosity, L , the effective radius, R_e , and the central velocity dispersion, σ . Some of them, are the Faber-Jackson (Faber and Jackson 1976, hereafter *FJ*), the Kormendy (Kormendy 1977, hereafter *KR*), and the fundamental plane (Djorgovski and Davis 1987, hereafter *FP*) relations. These scaling relations provide valuable information about the formation and evolution of ETGs and set tight constraints to galaxy formation models (Cimatti et al. 2006). The impact of dry merging on the scaling law of ETGs has been investigated in several works. In particular Capelato et al. (1995) and Dantas et al. (2003) investigated the origin of the *FP* correlation, showing that it can arise naturally from dissipationless galaxy-galaxy mergers. Evstigneeva et al. (2004) run several simulations to examine dissipationless mergers of low-mass systems and to analyze whether merger remnants still lie on the Kormendy relation. They observe that final products of the merging between small objects are not along the *KR* and they conclude that *ETGs* cannot be formed by merging dwarfs, unless a considerable amount of dissipation is involved. On the other hand, simulating the merging of objects on the *KR*, they obtain that end products lye on the *KR* provided that the observational scatter is taken into account. In a recent work, Nipoti et al. (2003) explored the effect of dissipationless merging on the scaling laws. They found that repeated merging of gas-free galaxies is unable to reproduce the observed scaling laws, since merger products are characterized by an unrealistically large effective radius and a mass-independent velocity dispersion. Ciotti et al. (2007) suggested that gas dissipation is necessary to avoid all problems posed by dry merging. By using analytical arguments and numerical simulations, they showed that massive ETGs cannot be formed by merging of low-mass spheroidal galaxies, even in the presence of substantial gas dissipation, while wet merging in the same population of low-mass progenitors leads to galaxies that are in much better agreement with the observed scaling laws. According to this, Hopkins et al. (2008a) found that dissipation is both necessary and sufficient to explain the *FP* tilt and differences between disk and elliptical scaling relations.

We note that in all previous works, the stellar component of model galaxies

is always described by either a de Vaucouleurs surface brightness profile (de Vaucouleurs 1948) or a King model (King 1962), while dark matter haloes are described by either a Navarro-Frenk-White profile (Navarro et al. 1995) or an Hernquist profile (Hernquist 1990). However, it is now clear that the observed properties of ETGs can be only described by using the Sérsic 1968 law (Caon et al. 1993; D’Onofrio et al. 1994; Graham et al. 1996), and recent results from N-body simulations have shown that the galactic-sized halos are also well described by a de-projected Sérsic profile (Graham et al. 2006a) as well. Thus, it is important to analyze if using more suitable models for both the luminous and dark matter components can bring new insights into our understanding of how dissipationless merging affects the properties of ETGs. To this aim, in this work, we built new two-components models, where both components are described by the Sérsic law.

In the following sections we introduce the Sérsic model (Sec. 2.1.1), and summarize previous results about the dark matter halo density profiles (Sec. 2.1.2). In Sec. 2.2 we present in details the properties of two-component Sérsic models and we discuss their stability, while in Sec. 2.3 we show how we choose their physical scale parameters. In Sec. 2.4 and Sec. 2.5 we present our method to define an optimal smoothing length and the code used to realize the models.

2.1.1 The Sérsic model

The $R^{1/4}$ -law:

$$I(R) \propto \exp \left[- \left(\frac{R}{R_e} \right)^{1/4} \right] \quad (2.1)$$

was firstly introduced by de Vaucouleurs (1948) and it has been used to describe remarkably well (Capaccioli 1989; Capaccioli et al. 1990) the projected luminosity density (or surface brightness) profile, $I(R)$, of elliptical galaxies as function of the two-dimensional projected radius R . The $R^{1/4}$ -law depends on two physical scales: a characteristic linear scale, R_e , (that contains half of the total galaxy luminosity) and the central surface brightness of the galaxy, I_0 . A natural generalization of this empirical law was proposed by Sérsic (1968), as the $R^{1/n}$ -law:

$$I(R) \propto \exp \left[- \left(\frac{R}{R_e} \right)^{1/n} \right]. \quad (2.2)$$

In this law, the parameter n , called the Sérsic index, controls the degree of curvature of the profile, in the sense that for large n , the profile is more

strongly peaked in the center. When $n = 1$ we have the exponential law which is a good description of dwarf elliptical galaxies and spiral galaxy disks. Most of ETGs are well fitted by Sérsic profiles with indices in the range $2 < n < 10$ (see Blanton et al. 2005). The best-fit value of n correlates with galaxy luminosity, in the sense that brighter galaxies tend to have larger n (Caon et al. 1993; Graham et al. 1996; Graham and Guzmán 2003b), indicating *structural non-homology* in the class of ETGs, i.e. the fact that the profile slope of ETGs changes systematically along the galaxy sequence (see e.g. Davies 1988; Capaccioli 1989; Caon et al. 1993; Young and Currie 1994; D’Onofrio et al. 1994; Prugniel and Simien 1997).

2.1.2 The density profile of dark-matter halos

In the past, virialized halos have been often modeled by using the isothermal sphere profile, characterized by two parameters, the central dark matter density, $\rho_{0_{DH}}$, and the core radius, r_c :

$$\rho_{DH}(r) = \frac{\rho_{0_{DH}}}{1 + (r/r_c)^2}, \quad (2.3)$$

where r is the three-dimensional radius of the system. N-body simulations of galactic halos (Dubinski and Carlberg 1991; Warren et al. 1992; Navarro et al. 1995) indicate that dark matter halos are not well described by isothermal spheres but they possess a logarithmic slope as in the model proposed by Hernquist (1990) for the stellar component of elliptical galaxies (Hernquist law):

$$\rho_{DH}(r) \propto \frac{1}{r(1 + r/r_s)^3}, \quad (2.4)$$

or as in the model introduced by Navarro et al. (1995) (NFW) to describe the X-ray profile of clusters of galaxies:

$$\rho_{DH}(r) \propto \frac{1}{r(1 + r/r_s)^2}. \quad (2.5)$$

These profiles are singular in the center (although the potential and the mass converge for $r \rightarrow 0$) and possess a scale radius, r_s , where the profile changes shape. N-body simulations of Cole and Lacey (1996) provided support for the NFW profile, although small but systematic differences began to emerge as the numerical resolution of the simulations improved (Fukushige and Makino 1997; Moore et al. 1999; Ghigna et al. 2000; Fukushige and Makino 2001, 2003). These authors reported slopes that increase systematically inwards with respect to that of the NFW model. Moore et al. (1999)

favoured a profile that diverges near the centre as $r^{-1.5}$ (instead of r^{-3} as for the NFW profile):

$$\rho_{DH}(r) = \frac{\rho_M}{(r/r_M)^{1.5}[1 + (r/r_M)^{1.5}]} . \quad (2.6)$$

Recognizing that galaxies appear to have flat inner density profiles (Flores and Primack 1994; Moore 1994), Burkert (1995) introduced a density model having an inner slope of zero and an outer profile dropping as r^{-3} . His model is given by:

$$\rho_{DH}(r) = \frac{\rho_0 r_s^3}{(r + r_s)(r^2 + r_s^2)} , \quad (2.7)$$

where ρ_0 is the central density and r_s is a scale radius. Application of this model reveals that, with only two free parameters, it is impossible provide a good fit to the profiles of dark matter halos (Graham et al. 2006a).

Recently Graham et al. (2006a) explored the suitability of *generalized* Sérsic model to describe the mass-density profile, $\rho_{DH}(r)$, of dark matter halos of galactic size. They define the model as such:

$$\rho_{DH}(r) = \rho_e \exp \left\{ -d_m \left[(r/r_e)^{1/m} - 1 \right] \right\} \quad (2.8)$$

The term d_m is a function of m such that ρ_e is the density at the half-mass radius, r_e , that defines a volume containing half of the total dark-matter mass. The central density is finite and given by $\rho_{DH}(r=0) = \rho_e \exp \{d_m\}$. Graham et al. (2006a) compared the ability of 2-parameter models and 3-parameter models to describe the density profiles of a sample of simulated dark matter halos. Not surprisingly, they found 3-parameter models to perform better than 2-parameter models such as the Burkert (1995) and the NFW models. They also found that both the generalized and the de-projected Sérsic models provide a better description of the data than the NFW model. Fitting both the Sérsic and NFW models to the halo profiles, they calculated the rms of the residuals, Δ . They found a value of $\Delta \sim 0.015$ dex for the de-projected Sérsic model, while using the NFW profile gave $\Delta \sim 0.05$ dex. Generalized Sérsic model was used also in Navarro et al. (2004) to fit simulated dark matter halos. They obtained a best fitting value of $n \sim (6 \pm 1.1)$. Subsequently, Merritt et al. (2005) showed that generalized Sérsic model gave better fits for the dwarf- and galaxy-sized halos, obtaining $n \sim (5.6 \pm 0.7)$. For a sample of galaxy-sized halos, Prada et al. (2006) obtained similar values from 6 to 7.5. For what concerns the de-projected Sérsic model, Graham et al. (2006a) obtained an average of the shape parameter for galaxy-size haloes of $n = 3.59 \pm 0.65$. Accordingly,

Merritt et al. (2005) found a value of 3.40 ± 0.36 for their sample of galactic halos. Thus, they concluded that Sérsic models perform significantly better than NFW law.

2.2 Two-component Sérsic models

The models described here consist of spherical, isotropic, non-rotating systems, having both a stellar and dark-matter components. Both components are described by a de-projected Sérsic law. In Sec. 2.2.1, we provide the basic equations that we use to de-project the Sérsic law, and calculate the corresponding density-potential pair. Sec. 2.2.2 describes how the global density-potential pair of the two-component models is obtained, while Sec. 2.2.3 discuss the physical *consistency* and the stability of these models.

2.2.1 The de-projected Sérsic model

The observed properties of ETGs, are well described by the Sérsic law (Cappacioli et al. 1992; Caon et al. 1993; D’Onofrio et al. 1994):

$$I(R; n) = I_0 \exp \left[-b_n (R/R_e)^{1/n} \right], \quad (2.9)$$

where I_0 is the central surface brightness of the galaxy, R is the two-dimensional projected radius, R_e is the equivalent scaling radius of the model, n is the so-called Sérsic index (shape parameter), and b_n is a function of n , defined in such a way that R_e is the effective radius of the galaxy, enclosing half of its total luminosity (Ciotti 1991). The quantity $b(n)$ is given, in first approximation, by the power-law relation $b(n) \sim 2n - 1/3$, and, with an accuracy better than 1%, by the formula $b(n) \sim \exp[0.6950 + \ln(n) - 0.1789/n]$ (e.g. Ciotti and Bertin 1999).

Under the assumption of spherical symmetry, for a constant stellar mass-to-light ratio, \mathcal{M}_L/L , the three-dimensional mass density profile, ρ_L , of the stellar component is obtained by solving the Abel integral equation (Binney and Tremaine 1994), $\rho_L(r) = -\frac{1}{\pi} \int_r^\infty \frac{dI}{dR} \frac{dR}{\sqrt{R^2 - r^2}}$, where r is the three-dimensional distance to the galaxy center. As shown in Appendix A, the Abel equation provides the following expression for the de-projected density profile

$$\rho_L(r; n) = \rho_{0L} \tilde{\rho}(x; n) = \rho_{0L} \frac{b}{\pi n} x^{\frac{1}{n}-1} \int_0^1 \frac{u^{-1/n} \exp[-bx^{1/n}u^{-1/n}] du}{\sqrt{1-u^2}}, \quad (2.10)$$

where $x = r/R_e$ is the three-dimensional distance to the galaxy center in units of R_e , $\tilde{\rho}(x; n)$ is the dimensionless de-projected profile, and $\rho_{0L} = \frac{M_*}{L} \frac{I_0}{R_e}$ is the scaling factor of the luminosity density of the model in physical units.

The mass profile is then obtained by solving the following one-dimensional integral:

$$\mathcal{M}_L(r; n) = M_{0L} \widetilde{M}(x; n), \quad (2.11)$$

with

$$\widetilde{M}(x; n) = \frac{4}{b^{2n}} \int_0^1 \frac{u^2}{(1-u^2)^{1/2}} \gamma \left(2n+1, b \left(\frac{x}{u} \right)^{1/n} \right), \quad (2.12)$$

where $\widetilde{M}(x; n)$ is the dimensionless mass profile and $M_{0L} = I_0 R_e^2$ is the corresponding scaling factor in physical units.

Using the second Newton theorem, after some algebra (see Appendix A), one finds the following expression for the gravitational potential:

$$\varphi(r; n) = \varphi_{0L} \widetilde{\varphi}(x; n) \quad (2.13)$$

with

$$\widetilde{\varphi}(x; n) = -\frac{\mathcal{M}_L(x)}{x} - \frac{4}{b^n} \int_0^1 u(1-u^2)^{-\frac{1}{2}} \widetilde{\gamma} \left(n+1, b \left(\frac{x}{u} \right)^{\frac{1}{n}} \right) du, \quad (2.14)$$

where $\widetilde{\varphi}(x; n)$ is the dimensionless gravitational potential, and $\varphi_{0L} = \frac{GM_L}{R_e}$ is the corresponding scaling factor in physical units.

In La Barbera et al. (2008) these one-component models are used to investigate the tilt of the Fundamental Plane of the ETGs.

As shown in the following sections, Eqs. 2.10, 2.11, and 2.13 are the fundamental ingredients to construct the two-component Sérsic models.

2.2.2 The dark matter component

Since the de-projected Sérsic law provides an accurate description of the density profile of dark matter haloes at galaxy's mass scales (see Graham et al. 2006a), we adopt the same kind of density profile for both the luminous and dark matter components of the models. The dark matter profile is described by a Sérsic model with shape parameter $n = 3$, in agreement with the value found by Graham et al. (2006a).

The density-potential pair and the mass profile of the dark matter com-

ponent are then obtained from the following equations:

$$\rho_D(r) = \frac{\mu}{x_D^3} \rho_{0L} \tilde{\rho} \left(\frac{x}{x_D}; n = 3 \right) \quad (2.15)$$

$$\mathcal{M}_D(r) = \mu M_{0L} \tilde{M} \left(\frac{x}{x_D}; n = 3 \right) \quad (2.16)$$

$$\varphi_D(r) = \frac{\mu}{x_D} \varphi_{0L} \tilde{\varphi} \left(\frac{x}{x_D}; n = 3 \right) \quad (2.17)$$

where the dimensionless density-potential pair $\tilde{\rho}, \tilde{\varphi}$, is provided by Eqs. 2.10 and 2.13, while the dimensionless mass profile, \tilde{M} is given by Eq. 2.11. Here, we denote as $\mu = \frac{\mathcal{M}_D}{\mathcal{M}_L}$ the ratio of the total halo mass, \mathcal{M}_D , to the total stellar mass \mathcal{M}_L , and as $x_D = \frac{R_{eD}}{R_{eL}}$ the ratio of the effective radii of the dark matter and luminous components.

The mass density profile of the two component model is $\rho(r) = \rho_L + \rho_D$ and is proportional to the dimensional factor ρ_{0L} . Due to the linearity of the Laplace equation, the total potential is equal to $\varphi = \varphi_L + \varphi_D$, and is proportional to the dimensional quantity φ_{0L} . The global density-potential pair is then completely defined, in dimensionless units, from the a-dimensional parameters x and μ , describing the relative extension of the halo to the stellar profile and the mass ratio of the two components.

2.2.3 Physical consistency and stability

In order to understand if a given density-potential pair can describe a physically admissible, stationary, system, we have to prove that the corresponding distribution function (hereafter DF) is non-negative for all possible values of the phase space coordinates. As shown by Ciotti (1991), one-component spherical, non-rotating, isotropic Sérsic models are always physically admissible, while in the anisotropic case, a minimum anisotropy radius exists for the model to be admissible, with this radius depending on the Sérsic index n (Ciotti and Lanzoni 1997). In order to understand if two-component Sérsic models describe admissible physical systems, we study here the properties of the corresponding DFs.

For a general collisionless system, the DF, f , or phase space density, is the solution of the collisionless Boltzmann equation, and it depends on phase space variables and on time. The f is related to the density ρ of the system by the equation $\rho(\mathbf{x}, t) = \int f(\mathbf{x}, \mathbf{v}, t) d^3\mathbf{v}$, where the integral is extended to the whole velocity space. If the system is stationary, f depends on the phase space coordinates only through the isolating integrals of motion

(Jeans Theorem), and moreover, if the system is spherical and its velocity dispersion tensor is isotropic, f depends only on the binding energy per unit mass. Generally, one introduces the relative binding energy of the system, \mathcal{E} , which is defined as the negative value of the binding energy per unit mass, and the absolute value of the potential, $\Psi(r)$ ¹. For a given density-potential pair, (ρ, Ψ) , $f(\mathcal{E})$ can be obtained by the Eddington formula (Eddington 1916):

$$f(\mathcal{E}) = \frac{1}{\sqrt{8\pi^2}} \left[\int_0^{\mathcal{E}} \frac{d^2\rho}{d\Psi^2} \frac{d\Psi}{\sqrt{\mathcal{E} - \Psi}} + \frac{1}{\sqrt{\mathcal{E}}} \left(\frac{d\rho}{d\Psi} \right)_{\Psi=0} \right]. \quad (2.18)$$

However, the Eddington inversion does not guarantee the distribution function to be non-negative, and, thus, for a given (ρ, Ψ) pair, one has to verify *a posteriori* that the condition $f(\mathcal{E}) \geq 0$ holds for $\mathcal{E} \geq 0$. The double $R^{1/n}$ -models are characterized by three parameters, i.e. the Sérsic index n , and the dimensionless parameters μ and x_D . Hence, one has to derive the f for different combinations of these parameters.

First, one can show that the second term in Eq. 2.18 vanishes. This follows directly by the fact that, for single Sérsic models, the quantity $(d\rho/d\Psi)_{\Psi=0} = \lim_{r \rightarrow \infty} (d\rho/dr)(dr/d\Psi) \rightarrow 0$ is always equal to zero for any positive value of n (Ciotti 1991). The distribution function is then computed from the integral at the second member of Eq. 2.18. Fig. 2.1 plots the function $f(\mathcal{E})$ for different sets of n , μ and x_D values. In order to calculate $f(\mathcal{E})$, we have used a set of FORTRAN codes using the NAG Fortran Library to numerically solve the integral in Eq. 2.18. The value of μ is varied in the range of zero (i.e. no dark matter halo) to a value of 10^6 , describing the cases where the stellar component is negligible and the system is completely dark matter dominated. We consider values of x_D from 0.1 to 10^2 , corresponding to the two extreme cases where the dark matter component is either more concentrated or significantly more extended than the luminous one. For all combinations of x_D and μ , different values of n are also plotted. We clearly see that for positive values of the relative binding energy the condition $f(\mathcal{E}) \geq 0$ is always verified. Thus, we conclude that the two-component Sérsic models are always physically admissible.

Following Ciotti (1991), in order to verify that the two-component Sérsic models describe stable physical systems, we analyze the sign of the first derivative of the distribution function. According to Antonov theorem (see Binney and Tremaine 1994, pag. 237), if $\frac{df}{d\mathcal{E}} \geq 0$, the system is stable against both radial and non-radial perturbations. This condition is equivalent to

¹One defines $\Psi(r) \equiv -\varphi(r) + \varphi_0$ and $\mathcal{E} \equiv -E + \varphi_0$, where φ_0 is a suitably defined constant (see Binney and Tremaine 1994).

require that the derivative of $\frac{d\rho}{d\Psi}$ is positive. We can write:

$$\begin{aligned} \frac{d^2\rho}{d\Psi^2} &= \frac{d^2\rho}{dr^2} \left(\frac{d\Psi}{dr}\right)^{-2} - \frac{d\rho}{dr} \left(\frac{d\Psi}{dr}\right)^{-3} \frac{d^2\Psi}{dr^2} = \\ &= \left(\frac{d\Psi}{dr}\right)^{-3} \left[\frac{d^2\rho}{dr^2} \left(\frac{d\Psi}{dr}\right) - \frac{d\rho}{dr} \left(\frac{d^2\Psi}{dr^2}\right) \right] \geq 0. \end{aligned} \quad (2.19)$$

Since $\Psi = -\Phi$ is a decreasing function of r , its first derivative is negative, and the last member in Eq. 2.19 is positive if and only if the following condition holds:

$$g(r; n, \mu, x_D) = \left[\frac{d^2\rho}{dr^2} \left(\frac{d\Phi}{dr}\right) - \frac{d\rho}{dr} \frac{d^2\Phi}{dr^2} \right] \geq 0. \quad (2.20)$$

For the two-component Sérsic models, the expression of $g(r)$ can be directly derived by a numerical computation of the dimensionless function $\tilde{\rho}(x)$, its first and second derivatives, and the corresponding mass profile $\tilde{\mathcal{M}}(x)$. Details are given in Appendix A. Fig. 2.2 plots $g(r)$ as a function of r for the same sets of n , μ , and x_D values considered in Fig. 2.1. The condition $g(r) \geq 0$ is always verified, implying that the two-component Sérsic models also describe stable physical systems.

2.3 Physical scales

The double Sérsic model consists of a stellar component following the Sérsic law and of a dark matter halo with the same mass distribution as the luminous component, but with a different physical scale. There are five fundamental physical parameters in the model, which are the mass of the stellar component, \mathcal{M}_L , its effective radius, R_{eL} , and Sérsic index, n , the mass of the dark matter halo, \mathcal{M}_D , and its effective radius, R_{eD} . Here, we show how all these quantities can essentially be expressed as a function of one single parameter, the absolute magnitude of the stellar component (hereafter we refer to this component as 'the galaxy'). We adopt the absolute magnitude in the B band, M_B , since most of the relations we use in the following are expressed in that band.

The R_{eL} parameter is obtained by using the Kormendy relation (Kormendy 1977; Capaccioli et al. 1992):

$$\log R_{eL} = \alpha < \mu >_e + \beta. \quad (2.21)$$

In order to set α and β , we use the values obtained for the Coma cluster ($z = 0.023$) by Graham and Guzmán (2003b) (see Fig. 2.3). The figure

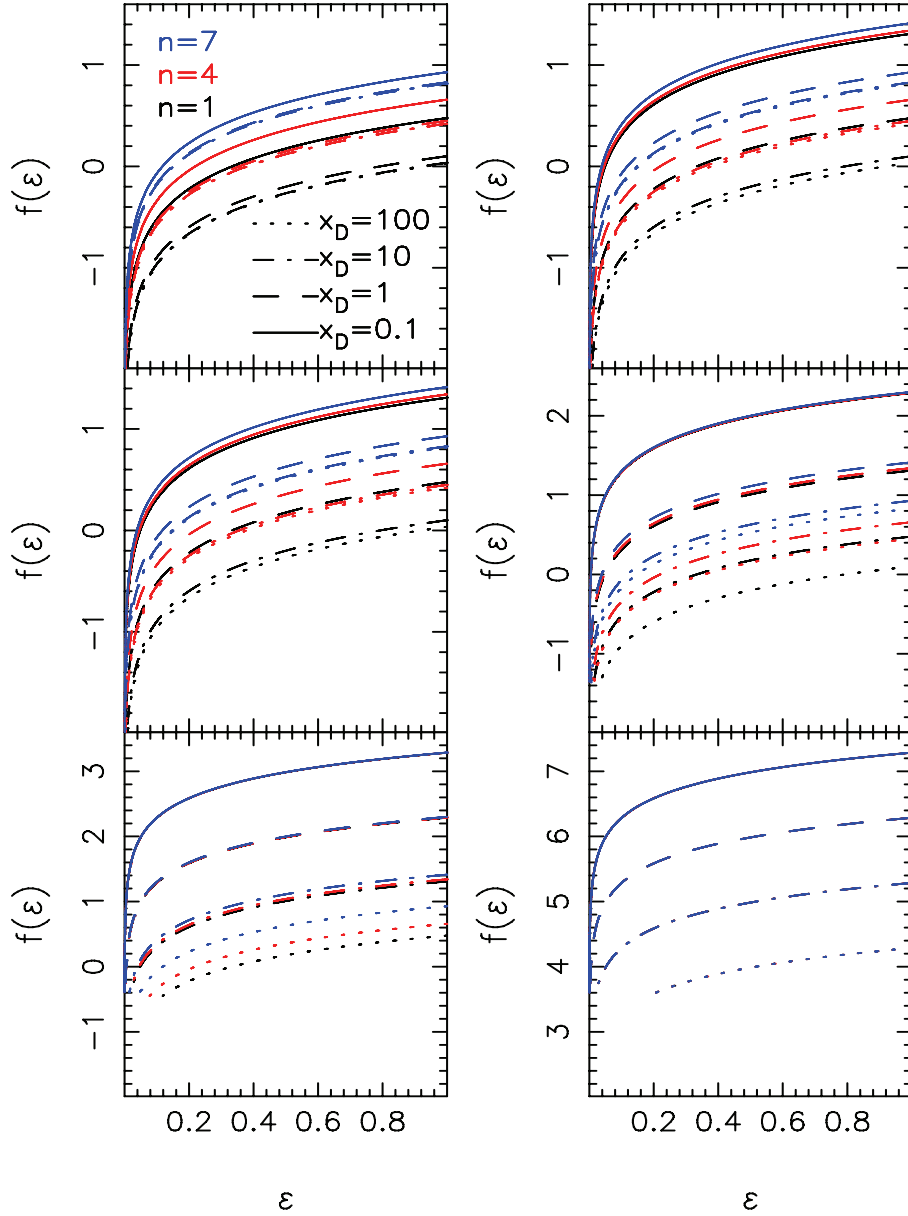


Figure 2.1: Distribution function of the two-component Sérsic models. Different panels correspond to different values of the halo to stellar mass ratio, μ . From left to right and top to bottom, the values of μ are 0, 0.1, 1, 10, 10^2 , 10^6 . For each plot, as shown in the upper-left panel, curves with different colors correspond to different values of the Sérsic index, while different line types denote different values of the ratio of halo to stellar effective radii, x_D .

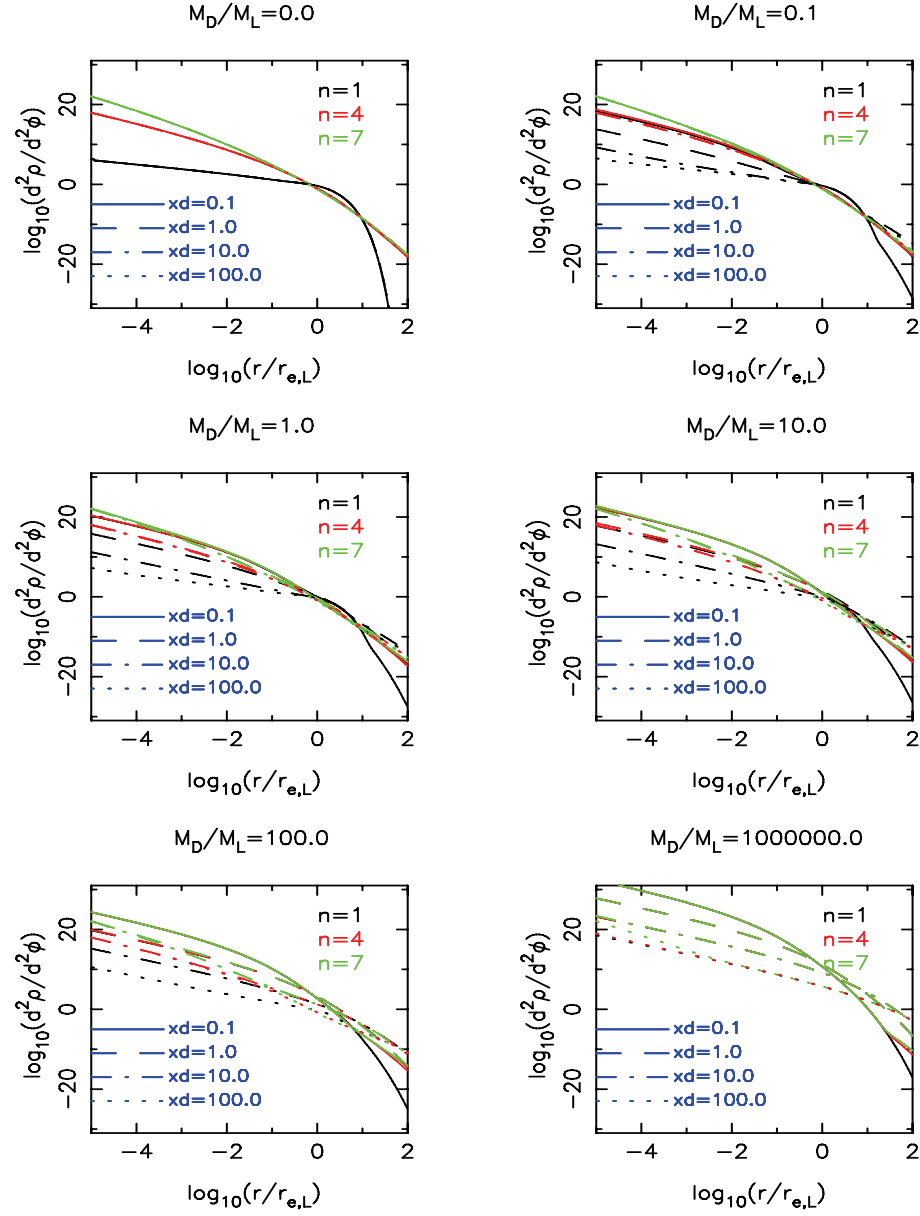


Figure 2.2: The quantity $g(r)$ (see Eq. 2.19) is plotted as a function of the logarithm of the dimensionless radius, $x = r/r_{e,L}$. Colors and line types are the same as in Fig. 2.1.

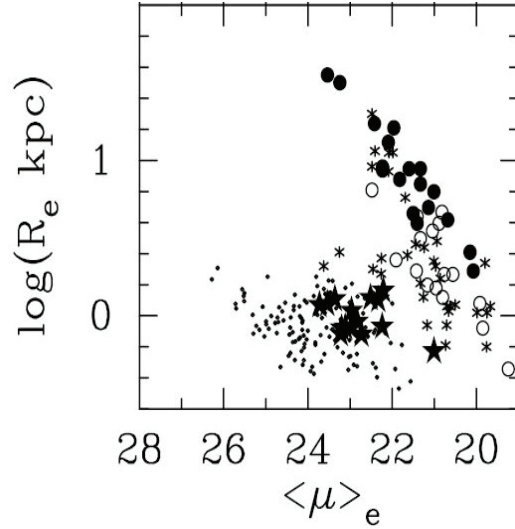


Figure 2.3: The Kormendy relation from Graham and Guzmán (2003b). Dots represent dwarf elliptical galaxies (dEGs) from Binggeli and Jerjen (1998), triangles represent dEGs from Stiavelli et al. (2001), five-pointed stars represent the Coma dEGs from Graham and Guzmán (2003b), asterisks represent intermediate-to-bright EGs from Caon et al. (1993) and D’Onofrio et al. (1994), open circles represent the so-called power-law EGs from Faber et al. (1997), and filled circles represent the *core* EGs from these same authors.

clearly shows a different trend for bright and *ordinary* ETGs in the plane $\log R_e - \langle \mu \rangle_e$. By a linear fit of the data in this figure, we obtain $\alpha = 0.35$ and $\beta = -6.75$ for bright galaxies and $\alpha = -0.02$ and $\beta = 0.45$ for *ordinary* galaxies. We put the threshold between these two families at $M_B = -20$ as can be deduced from Fig. 2.3

In order to set the Sérsic parameter n for the stellar component in our models, we use the $M_B - n$ relation by Trujillo et al. (2004), as shown in Fig. 2.4:

$$\log n = -0.12 \cdot M_B - 1.6829 \quad (2.22)$$

where the slope and the zero-point of this relation are obtained from a linear fit of the data in that figure.

To determine R_{eD} , we consider the Kormendy relation for dark matter halos in Graham et al. (2006b), defined as the correlation between the effective radius, R_{eD} , and the average projected surface density inside of R_{eD} , $\langle \mu \rangle_{eD}$. This relation is obtained for a sample of simulated galaxy-sized halos whose density profiles are extracted fitting Prugniel-Simien models (Prugniel and Simien 1997). In Fig. 2.5 we show this relation. From a linear fit of the data in figure, we obtained a zero-point of $\delta \sim 10/3$ and a slope of $\gamma \sim 1/3$.

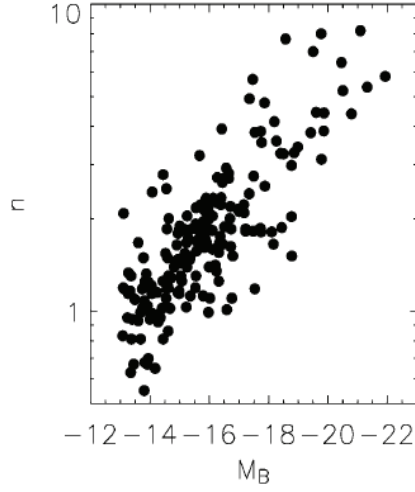


Figure 2.4: Sérsic index n as a function of the absolute magnitude from 911 morphologically selected ETGs from a combined SDSS/2MASS galaxy catalog from Trujillo et al. (2004).

We then use the relation between the mean mass surface density within R_{e_D} and the total mass of the halo:

$$\langle \mu \rangle_{e_D} = -2.5 \log(\mathcal{M}_D) + 2.5 \log(2\pi) + 5 \log(R_{e_D}), \quad (2.23)$$

from which we obtain:

$$R_{e_D} = 10^{\frac{2.5}{2} \log(\mathcal{M}_D) - \frac{2.5}{2} \log(2\pi) - \frac{25}{2}}. \quad (2.24)$$

According to Graham et al. (2006a) (their figure 1, panel *b*) we set $R_{e_D} = 1 \text{ kpc}$ for all dark matter halos with $\mathcal{M}_D \leq 10^{10} M_\odot$. Then, we express the stellar and halo masses as function of the total B-band luminosity:

$$\frac{L_B}{L_{B_\odot}} = 10^{[-0.4(M_B - M_{B_\odot})]}, \quad (2.25)$$

where we adopt a B-band absolute magnitude for the Sun of $M_{B_\odot} = 5.51$ (Fukugita et al. 1995). We use the result of Cappellari et al. (2006), who found a correlation between the dynamical mass-to-light ratio in *I*-band and the total mass of elliptical and lenticular galaxies in the SAURON project (Bacon et al. 2001):

$$\left(\frac{\mathcal{M}}{L_I} \right)_{dyn} = (1.78 \pm 0.16) \left(\frac{\mathcal{M}}{10^{10} M_\odot} \right)^{(0.27 \pm 0.03)}. \quad (2.26)$$

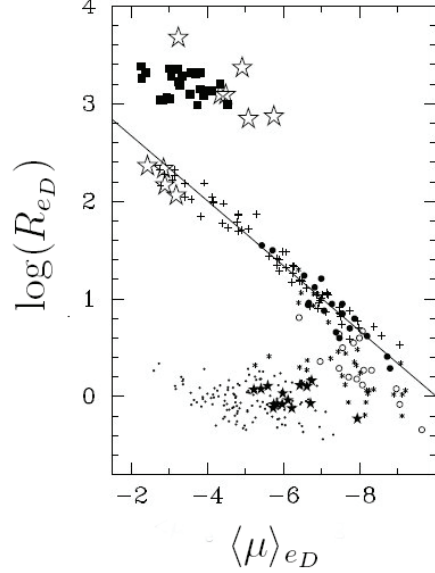


Figure 2.5: The Kormendy relation for the dark halo. The open stars represent N-body, dark matter halos from Graham et al. (2006b), open plus signs are the galaxy clusters from Graham and Guzmán (2003a), the dots are the dwarf elliptical galaxies from Binggeli and Jerjen (1998), the filled stars are the dwarf elliptical galaxies from Graham and Guzmán (2003b), the asterisk are the intermediate to bright elliptical galaxies from Caon et al. (1993) and D’Onofrio et al. (1994), open and filled circles are the *power-law* and *core* elliptical galaxies from Faber et al. (1997).

We invert this relation to obtain the total mass, \mathcal{M} , of the galaxy as function of the total luminosity in I -band, L_I :

$$\mathcal{M} = 10^{\frac{\log(L_I) + \log(1.78) - 2.7}{1 - 0.27}} . \quad (2.27)$$

We express \mathcal{M} as a function of M_B , by using the Eq. 2.25 and by using a $(B-I)$ color term of 2.23 and according to Fukugita et al. (1995) $M_{I_\odot} = 4.08$. We note that from figure 17 of Cappellari et al. (2006) the stellar mass-luminosity ratio is 16% smaller than dynamical mass-to-light ratio. Hence we write:

$$\mathcal{M}_L = \left(\frac{\mathcal{M}}{L_I} \right)_L 10^{\{-0.4(M_I - M_{I_\odot})\}} . \quad (2.28)$$

and we derive the dark matter mass of the galaxy as the difference:

$$\mathcal{M}_D = \mathcal{M} - \mathcal{M}_L . \quad (2.29)$$

To summarize, using Eqs. 2.29, 2.28 and 2.27 we are able to express \mathcal{M}_D and \mathcal{M}_L as function of M_B . Then using Eq. 2.24, we also obtain R_{eD} from M_B . Finally, from Eqs. 2.21 and 2.22 we obtain also R_{eL} and n as function of M_B . In Tab. 2.1 we show the values of \mathcal{M}_L , R_{eL} , \mathcal{M}_D , R_{eD} and n for different values of the magnitude M_B , as obtained with the above procedure. The values of M_B are those adopted to perform simulations of dissipationless merging between two-component Sérsic models (see Chapter 3).

M_B	\mathcal{M}_L ($10^{10} M_\odot$)	R_{eL} (kpc)	\mathcal{M}_D ($10^{10} M_\odot$)	R_{eD} (kpc)
-21.0	27	6.3	12	19.5
-20.2	11	2.8	4.8	6.2
-19.5	4.3	1.2	1.9	2.0
-18.0	0.7	1.1	0.3	1.0
-17.2	0.3	1.0	0.1	1.0
-16.5	0.1	1.0	0.05	1.0

Table 2.1: The columns report the magnitude in B -band, M_B , the stellar mass, \mathcal{M}_L , in units of $10^{10} M_\odot$, the effective radius of the stellar component, R_{eL} , the dark matter halo mass, \mathcal{M}_D in units of $10^{10} M_\odot$ and effective radius of the dark matter halo component, R_{eD} , (see text for details) for two-component Sérsic models used as progenitors in simulations of dissipationless merging (see Chapter 3).

2.4 Discrete realizations

We mainly aim to apply the two-component Sérsic models to studying how dissipation-less merging affects the observed properties of early-type systems. In order to address this issue, one has to use N-body simulation codes, producing discrete realizations of a given model. As a common practice, the discretization procedure requires to choose a given number of particles and to adopt a given gravitational *softening* parameter, that ultimately define the mass and spatial resolutions of the system. Here, we describe how we set these parameters for the Sérsic models in an objective way. The *softening* parameter also depends on the kind of *softening* function used in the simulation code. We refer here to the case of the smoothing kernel of Plummer (Binney and Tremaine 1994).

2.4.1 Optimal softening length

Mass and spatial resolutions are the crucial parameters that define the capability of N-body codes to describe properties of gravitationally bound

systems. Mass resolution is fixed by the total number of particles, while spatial resolution is related to the problem of computing gravitational forces. For a given mass density profile, ρ , the gravitational potential, ϕ , and the corresponding gravitational force are obtained by solving the Poisson equation. Since numerical simulations involve discrete realizations of ρ , with a finite number of particles, it is common practice to calculate the total force on the i -th particle, $\mathbf{F}_i = -\nabla\phi$, in terms of the contribution due to all the other particles in the system, $\mathbf{F}_i = \sum_{i \neq j} GM_j(\mathbf{r}_i - \mathbf{r}_j)/|\mathbf{r}_i - \mathbf{r}_j|^3$, where \mathbf{r}_j and M_j are the position and mass of the j -th particle, respectively. The gravitational force is usually smoothed on a given scale ϵ in order to (i) avoid divergences in force computation and to (ii) minimize two-body collisions that arise only from the discreteness of N -body realizations, and that introduce an undesired energy dissipation in the system. The ϵ parameter is called the softening (smoothing) length, and determines the spatial resolution of the simulation. In the case of cosmological simulations, spatial resolution is related to the ratio of the simulation box size to the smoothing length. Considering the Plummer smoothing kernel, the force exerted on the i -th particle from the j -th particle of an N -body realization is given by the following formula:

$$\mathbf{F}_{ij} = \frac{Gm^2(\mathbf{x}_j - \mathbf{x}_i)}{(\epsilon^2 + |\mathbf{x}_j - \mathbf{x}_i|^2)^{3/2}}, \quad (2.30)$$

where both particles are assumed to have the same mass m , and ϵ is the softening length, describing the level of smoothing in \mathbf{F}_{ij} . The maximum force intensity is $2Gm^2/(3^{3/2}\epsilon^2)$ and occurs at $|\mathbf{x}_j - \mathbf{x}_i|^2 = \frac{1}{2}\epsilon^2$.

In previous studies, the value of ϵ is often chosen in an *ad hoc* way, by using different physical recipes involving the desired resolution and the total number of simulated particles.

Merritt (1996) showed that the softening length of an N -body system can be chosen in an *optimum* way by minimizing the average error in the force computation over the whole space. He found that the mean value of the integrated square error in the force computation contains contributions from two terms. The first one (the bias) is the mean deviation of the computed force at some point from the true force and the second (the variance) is the mean square deviation of the force estimation from its mean value. Merritt (1996) showed that the bias increases with the softening length while the variance falls off because a greater amount of smoothing produces smaller average fluctuations in the forces but also tends to smooth over real features at small scales. Thus, for N -particles realizations of a given model there is an optimal choice of softening length, derived by minimizing the sum of these two contributions.

Following a similar approach, we choose ϵ by minimizing the average error in the computation of the gravitational potential.

We proceed as follows. For a given Sérsic index and a given number of particles, N , we generate several realizations of the deprojected Sérsic model. For each of them, we calculate the gravitational potential at the position of particle i :

$$\phi_i = -Gm \sum_{j=1}^N \frac{1}{\sqrt{\epsilon^2 + |\mathbf{x}_j - \mathbf{x}_i|^2}}. \quad (2.31)$$

At the same position in the space, there is also a *true* value of the potential, $\phi_{true}(\mathbf{x}_i)$:

$$\phi_{true}(\mathbf{x}_i) = -G \int \frac{\rho(\mathbf{x}') d\mathbf{x}'}{\sqrt{|\mathbf{x}' - \mathbf{x}_i|^2}}, \quad (2.32)$$

where ρ is given by the Eq. 2.10. In Fig. 2.6 we plot for two different discrete realizations of a Sérsic model with $n = 4$, the rms of relative differences between the true and the discrete potentials, $\Delta\phi/\phi$, as function of ϵ .

The plot demonstrates that there is a minimum in the relative error and this minimum depends on the adopted number of particles. thus, we calculate the value of the optimal softening length, ϵ_{best} , by minimizing the root mean square of differences between ϕ_i and $\phi_{true}(\mathbf{x}_i)$:

$$\sigma_{\phi_i} = \frac{1}{N} \sum_{i=1}^N |\phi_i - \phi_{true}(\mathbf{x}_i)|^2, \quad (2.33)$$

where the sum runs over all the particles. We adopt as optimal softening length the mean value of ϵ_{best} , computed from 100 realizations. Fig. 2.7 plots the optimal value of ϵ for different values of n as a function of N . As shown in the figure, the trend of ϵ vs. N can be modeled by the following power laws:

$$\epsilon = \frac{\beta}{N^\alpha}, \quad (2.34)$$

where both α and β change as a function of the Sérsic index. The optimal softening length turns out to decrease as a function of both n and the number of particles in the simulation. The trend of ϵ with n , at fixed N , can be explained by considering how the value of n is related to the mean particle distance, d_N , in the simulation. For a given number of particle, if n decreases, the model is less concentrated in the center and the value of d_N increases.

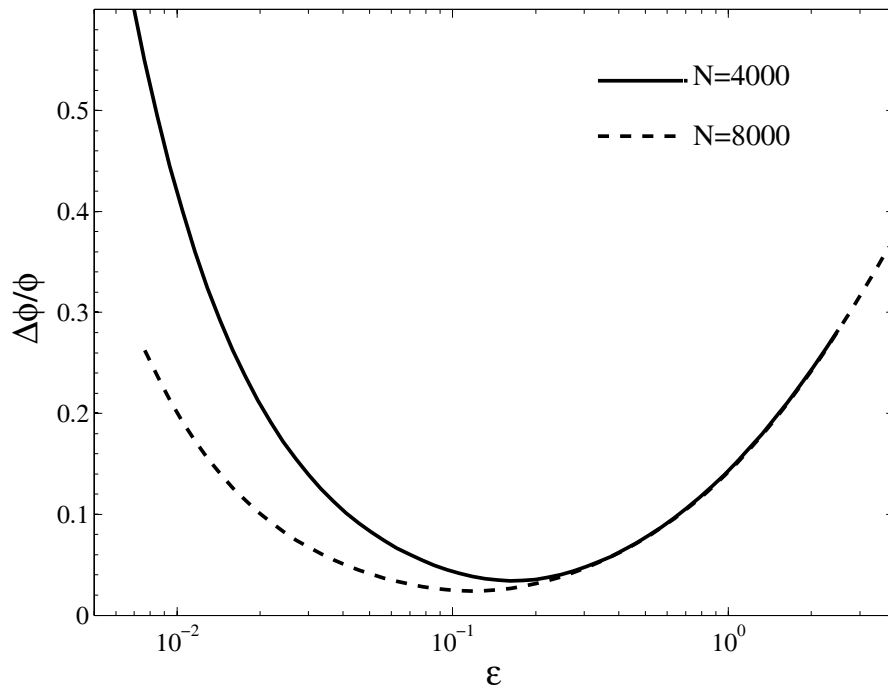


Figure 2.6: Relative root mean square error in the potential calculation as a function of ϵ values for two different discrete realizations of a one-component Sérsic model with $n = 4$. The number of particles is $N = 4000$ and $N = 8000$ for the dashed and solid curves, respectively, as shown in the upper right corner of the figure.

Therefore in order to minimize the effect of collisions, the optimal smoothing parameter has to be increased.

For what concerns the trend of ϵ with N , we can observe that when N increases, at fixed n , the average particle distance decreases and the optimal value of ϵ has to decrease as well.

We have also estimated the relative error $\delta\phi/\phi$, due to the use of the optimal ϵ in the potential calculation. As shown in the Fig. 2.8, $\delta\phi/\phi$ depends on the number of particles, N , and on the Sérsic index, n . For a given Sérsic model, the error decreases when N increases. In particular, as expected performing a linear fit, we found the power-law trend $\delta\phi/\phi \sim N^{1/2}$.

2.4.2 Systems in isolation

For the discrete realizations of two-component Sérsic models, we adopt a different softening length for the stellar and dark matter models, according to the optimal definition presented above. However, these softening parameters represent an optimal choice only for one-component Sérsic models, and we are not guaranteed that they represent also an accurate choice for the two-component models. In order to address this issue, we made several tests by running some discrete realizations of the two-component models in isolation and we compare the results with those obtained for one-component models. As example, we present here the results obtained for two given one- and two-component models. For the one-component model, we adopt $\mathcal{M}_L = 10^{10}M_\odot$, $R_{e_L} = 10kpc$, $n = 4$, $N_L = 50000$, where N_L is the number of particles. For the two-component model, the parameters are: $\mathcal{M}_D = 10^{12}M_\odot$, $R_{e_D} = 100kpc$, $N_D = 100000$ and $\mathcal{M}_L = 10^{10}M_\odot$, $R_{e_L} = 10kpc$, $n = 4$, $N_L = 50000$ for the dark and stellar components, respectively. Both simulations were run for $5Gyrs$. On the basis of the criteria discussed in Sec. 2.4.1, we adopt the following value of the softening length for the dark and stellar component: $\epsilon_D = 0.75kpc$ and $\epsilon_L = 0.2kpc$.

In the upper panel of Fig. 2.9 the quantity $|\Delta E/E| \equiv |E - E_0|/|E_0|$ is plotted as a function of time. We note a small slow secular drift in the total energy, E . However, we can see that the total energy of the system is preserved within 2% over $5Gyrs$. The lower panel of the figure shows the evolution of the virial ratio $|2T/W|$, where T and W are the total kinetic energy and potential energy of the system. Deviations from the equilibrium value $2T/W = 1$ is smaller than 2% in modulus and do not show any significant trend over the whole simulation. The same result were obtained when analyzing the one-component models.

In Fig. 2.10 we plot, for the one-component model, the dynamical profiles, (mass, velocity dispersion and anisotropy) at $T = 0Gyr$ (left panels). In the

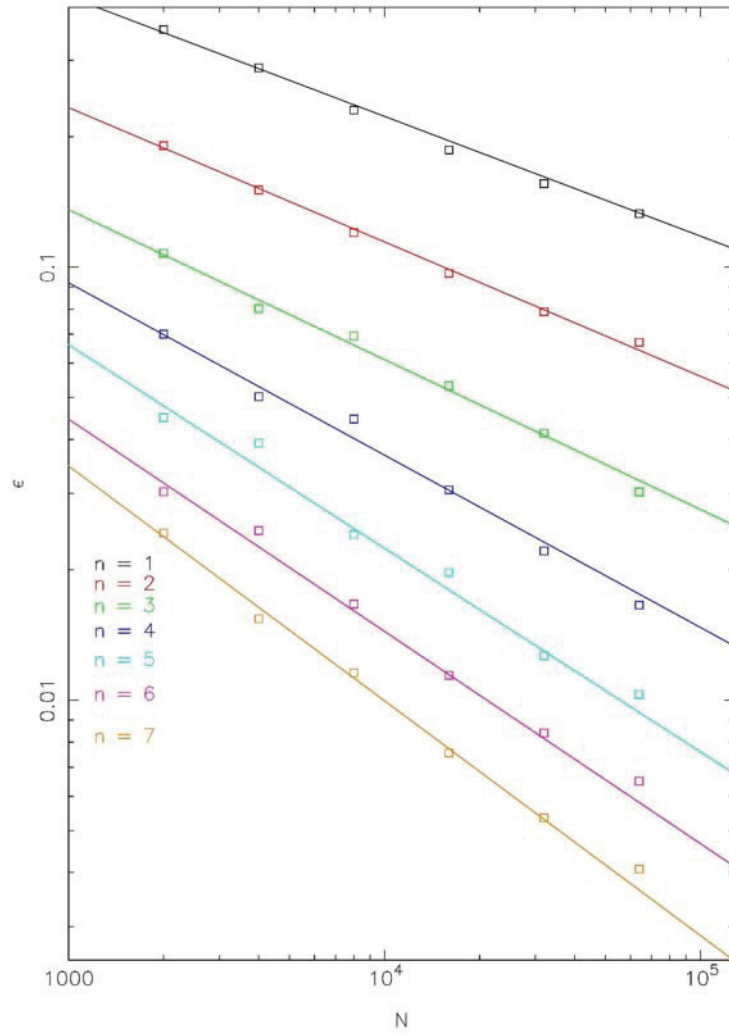


Figure 2.7: Dependence of the optimal softening length ϵ on the number of particles, N , for different galaxy models. The best-fitted power law relations in Eq. 2.34 are indicated by solid lines, with different colors corresponding to different Sérsic indices as shown in the lower-left part of the figure.

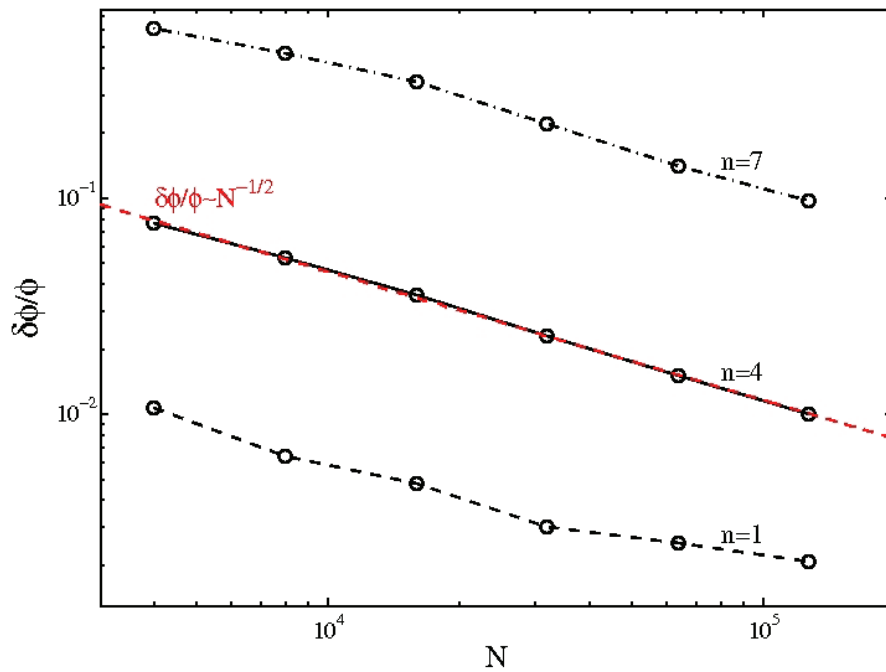


Figure 2.8: The relative error in the potential calculation as a function of the number of particles, N , for three different discrete realizations of a Sérsic model with $n = 1$ (dashed line), $n = 4$ (solid line) and $n = 7$ (dot-dashed line). The red line is obtained from a linear fit of the data in the case $n = 4$.

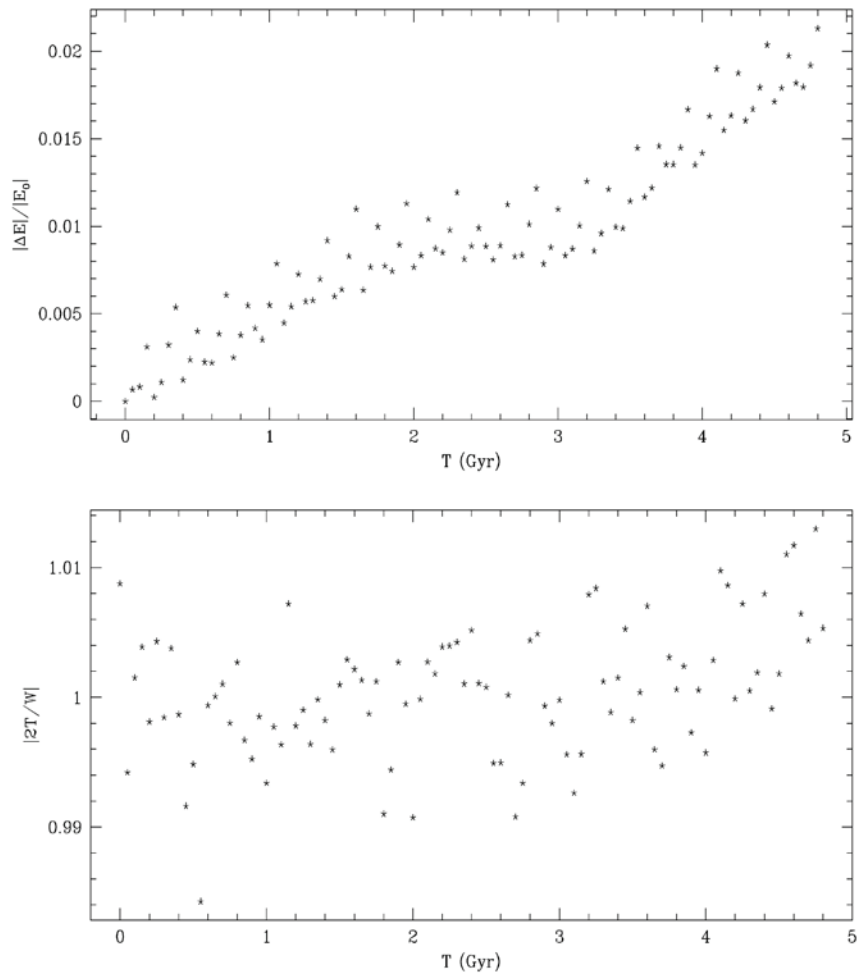


Figure 2.9: Total energy and virial ratio as function of the time for a given two-component model in isolation.

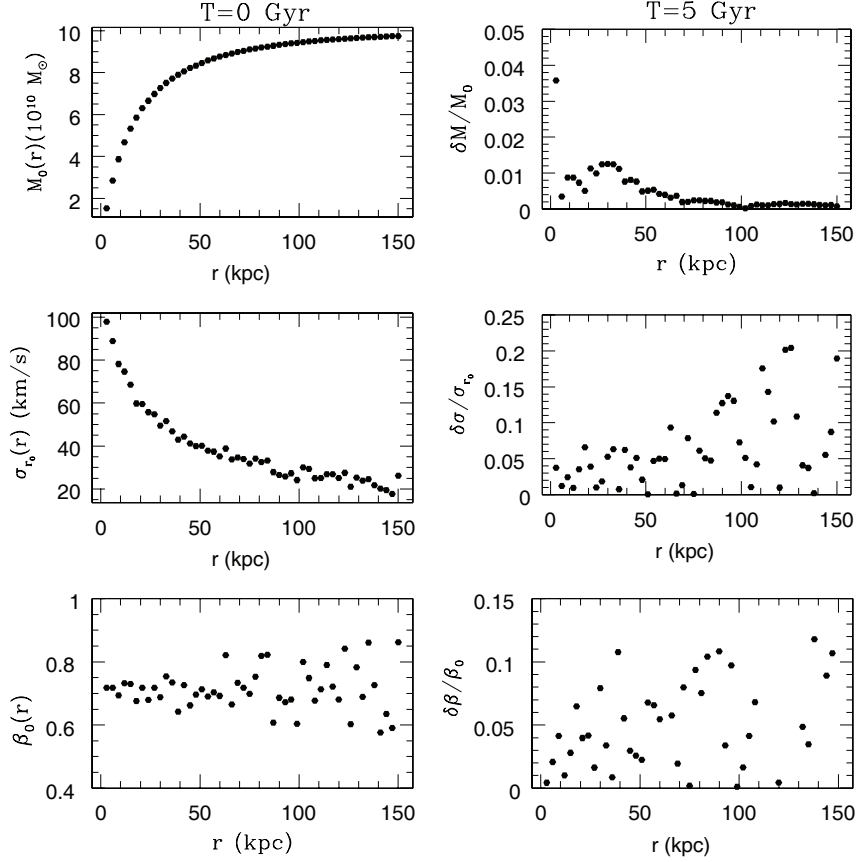


Figure 2.10: Mass (top), velocity dispersion (middle) and anisotropy (bottom) profiles for a one-component model at $T = 0$ Gyr (left panels). In the right panels, we plot the relative variation of the same quantities at $T = 5$ Gyr respect to the initial values.

right panels of the figure we plot the relative variation of the same quantities after 5 Gyr. In Fig. 2.11 and 2.12 we plot the same profiles as in Fig. 2.10 for the stellar and the dark matter components of the two-component model. Remarkably, all the profiles remain stable for systems in isolation, over at least 5 Gyr

2.5 The code

In order to build the discrete realizations of Sérsic two-component models we have written FORTRAN programs using the NAG Fortran Library (<http://www.nag.co.uk/numeric/FL/fldescription.asp>). Since the computation of the density-potential pair is very time-consuming, we proceeded as

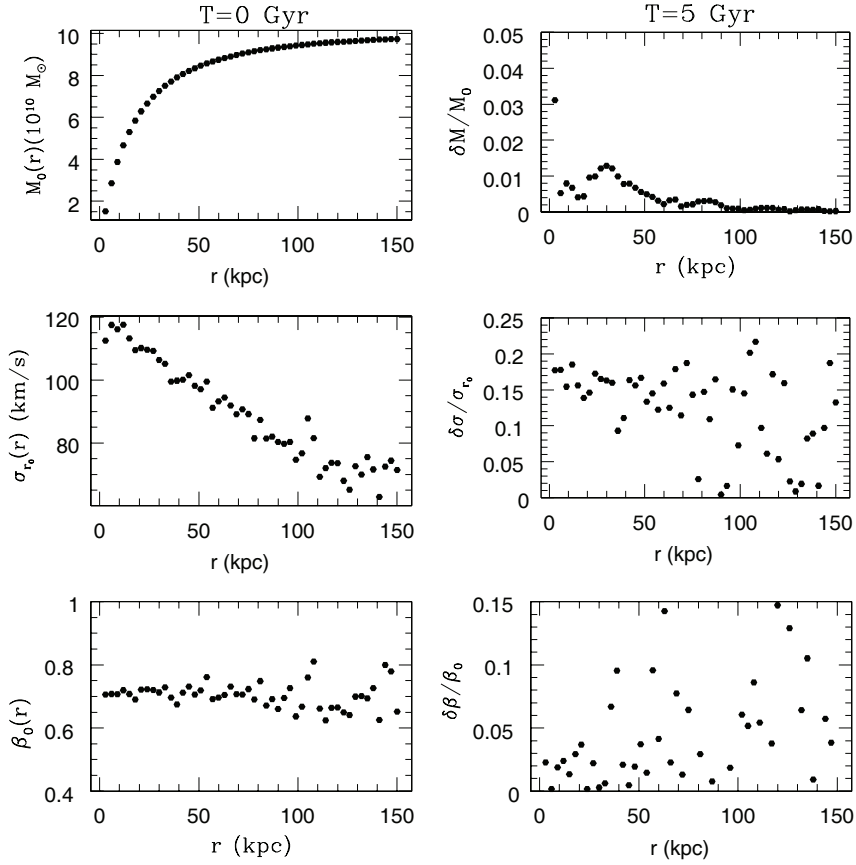


Figure 2.11: Same as Fig. 2.10 but for the luminous component of the two-component model.

follows::

1. for different values of the Sérsic index n , we realize a table including values of the mass, density, potential and their first and second derivatives as a function of the radius r , according to Eqs. 2.11, 2.10 and 2.13.
2. For any given model, with assigned n , μ and x_D parameters, we use the above tables to calculate by interpolation, the global density-potential pair and the distribution function.
3. We randomly extract a given number of stellar and dark matter particles from the given global density profile.
4. For each particle, using the corresponding global potential φ (see Eq. 2.13), we randomly assign a velocity \mathbf{v} according to the distribution

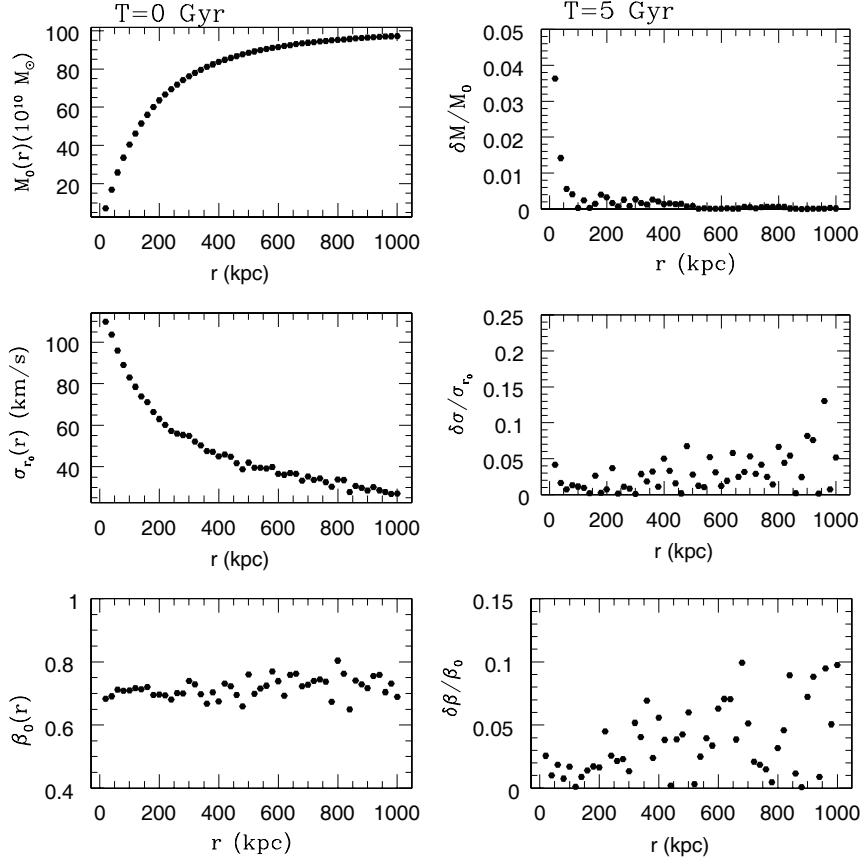


Figure 2.12: Same as Fig. 2.10 but for the dark matter component of the two-component model.

function $f(\mathcal{E})$ (see Eq. 2.18).

2.6 Summary

We have built discrete realizations of non rotating, isotropic and spherical systems containing a stellar component and a dark matter halo to study how observable properties of ETGs change during dissipationless merging. In order to reproduce the observed properties of ETGs the stellar component is modelled by using the deprojected Sérsic law. In agreement with recent results from N-body simulations, we use the same model to build the halo component. We provide the basic equations for de-projecting the Sérsic law, and to calculate the corresponding density-potential pair. We describe in detail how the models are constructed, in particular we show that their total

distribution function is always non-negative. This implies that the models are stable against radial and non-radial perturbation. In order to verify the physical consistency of our models we also show that the first derivative of the total distribution function is non-negative for all possible pairs of (ρ, Ψ) , this implies that $f(\mathcal{E})$ is a physical solution of the collisionless Boltzmann equation. We set up physical parameters (scaling radii and total masses) by using the observed relations among them for ETGs at redshift $z \sim 0$. Physical parameters are uniquely defined by the total B-band luminosity. For each model, we are able to define an optimal smoothing length, defined as the softening parameter that minimizes the rms of the discrete and true gravitational potential of each system.

Chapter 3

Dissipation-less merging of early-type galaxies: scaling relations and internal color gradients

We analyze the effect of dissipation-less merging on scaling laws and internal color gradients of early-type galaxies (hereafter ETGs), by performing N-body merging simulations of the one- and two-component Sérsic models described in Chapter 2. The outline of the Chapter is as follows. In Sec. 3.1 we describe the initial conditions of the merging simulations, and how the simulations are done with the software GADGET-2. In particular, we describe how the number of particles is chosen, and how we set the corresponding softening parameter for each simulation. In Sec. 3.2, the properties of merger remnants are derived. We discuss how the structural parameters and velocity dispersion of merger remnants are estimated. In Sec. 3.3, we analyze the surface brightness profile of the merging end-products and we describe how we fit them with a Sérsic law. In Secs. 3.4, we analyze the correlations among the properties of merger remnants, i.e. the Fundamental Plane relation (Sec. 3.4.1), the Kormendy relation (Sec. 3.4.2), the Faber-Jackson relation (Sec. 3.4.3), and the luminosity-size relation (Sec. 3.4.4). Finally, Sec. 3.5 deals with the internal structure of merger remnants. We analyze how stellar population gradients of model galaxies are changed from the encounters.

3.1 The models and the initial conditions of merging simulations

We performed two sets of merging simulations, with (1) Sérsic models with a single, stellar component and (2) two-component Sérsic models, including both a stellar and dark-matter component. As described in Chapter 2, all the models describe spherical, isotropic, non-rotating galaxy systems. Two-component models are characterized by five parameters, which are the mass of the stellar component, \mathcal{M}_L , the mass of the dark matter component, \mathcal{M}_D , the half-light radius of the stellar component, R_{eL} , the half mass radius of the dark-matter component, R_{eD} , and the Sérsic index, n , of the luminous component. As shown in Sec. 2.3, observed correlations of properties of ETGs, we allow us to derive each of these quantities from the total B-band luminosity. In other terms, each model is completely characterized by the B-band magnitude, M_B , with all the model parameters being assigned as a function of M_B .

For both sets of simulations, we consider six merger progenitors, spanning the magnitude range from -21 to -16.5 in B-band. The magnitude of each model and the corresponding model parameters are listed in Tab. 3.1. Each model is identified by a running number from one to six. Models one and four have magnitudes of -21 and -18 , which are chosen to describe typical bright and ordinary ETGs, respectively (Capaccioli et al. 1992). The magnitudes of models two and three are chosen in order to have a luminosity ratio of $1 : 2$ and $1 : 4$ with respect to model one. In the same way, models five and six are chosen to have a luminosity ratio of $1 : 2$ and $1 : 4$ with respect to model four. In Secs. 3.1.1 and 3.1.2, we describe how we choose the pairs for merging simulations and how the merging is performed by creating discrete realizations of the one- and two-component models.

For each merger pair, we assign the initial conditions of the encounter by initially placing the progenitors on four different orbits. Following Binney and Tremaine (1994, chapter 7, pag. 454), each orbit is characterized by two dimensionless parameters:

$$E \equiv \frac{E_{orb}}{\frac{1}{2}\langle v^2 \rangle} \quad \text{and} \quad L \equiv \frac{L}{r_h \langle v^2 \rangle^{1/2}}, \quad (3.1)$$

where r_h is the geometric mean of the three-dimensional half-light radii and $\langle v^2 \rangle$ is the geometric mean of the internal mean-square velocities of the two merging galaxies. E_{orb} and L are the energy and the angular momentum per unit mass of the orbit, defined as the orbital energy and angular momentum of two point masses equivalent to the merger galaxies. According to Binney

and Tremaine (1994, chapter 7, pag. 454), galaxies can merge on a time scale smaller than the Hubble time only in a given region of the $E_{orb} - L$ plane (see their Fig. 7 – 9). For a given value of E_{orb} there is a maximum value of L above which two systems do not merge. Moreover, as shown by Khochfar and Burkert (2003), cosmological simulations show that galaxy encounters on hyperbolic orbits are extremely rare. We thus considered only cases with $E = 0$ (parabolic orbits) and $E < 0$ (elliptic and circular orbits). To cover a wide range of initial conditions in the allowed region defined by Binney and Tremaine (1994), we considered mergers with two values of the orbital energy, $E = 0$ and $E = -3$. For each energy, two values of the angular momentum were considered: $L = 0$ and $L = 2$, respectively, resulting in a total of four different initial orbits for each merger pair. Following previous works (Dantas et al. 2003), in the case of parabolic orbits, the initial separation of the models was set to $\sim 4r_h$, while for elliptic orbits the apocentric position was adopted. These initial separations are chosen considering that the merging galaxies should be neither too close (implying that tidal effects would be artificially disregarded owing to the spherical symmetry of the initial models) nor too far away (so that one can avoid too time-consuming CPU runs).

<i>Models</i>	M_B	\mathcal{M}_L ($10^{10} M_\odot$)	R_{eL} (kpc)	\mathcal{M}_D ($10^{10} M_\odot$)	R_{eD} (kpc)	n
(1)	(2)	(3)	(4)	(5)	(6)	(7)
1	-21.0	27	6.3	12	19.5	7.55
2	-20.2	11	2.8	4.8	6.2	6.11
3	-19.5	4.3	1.2	1.9	2.0	4.95
4	-18.0	0.7	1.1	0.3	1.0	3.25
5	-17.2	0.3	1.0	0.1	1.0	2.63
6	-16.5	0.1	1.0	0.05	1.0	2.13

Table 3.1: For each progenitor, the columns report (1) the identification number, (2) the B -band magnitude, M_B , (3) the stellar mass, \mathcal{M}_L , in units of $10^{10} M_\odot$, where M_\odot is the solar mass, (4) the effective radius of the stellar component, R_{eL} , in units of kpc , (5) the dark matter halo mass, \mathcal{M}_D in units of $10^{10} M_\odot$, (6) the effective radius of the dark matter halo component, R_{eD} , in units of kpc , and (7) the Sérsic index n of the stellar component. All the parameters are assigned as a function of the B.band magnitude as described in Chapter 2.

3.1.1 One-component models

For merging simulations of one-component models, we consider six model pairs. This is illustrated in columns 2 and 3 of Tab. 3.2, where we report the

identification numbers of galaxy models in each merger pair (as in Tab. 3.1). The brightest galaxy model (model one in Tab. 3.1) is merged with itself (mass and luminosity ratio of 1 : 1), and with models two and three, allowing us to describe the case of *minor mergers* with a luminosity ratio of 1 : 2 and 1 : 4, respectively. As shown in Tab. 3.2, these luminosity ratios correspond to mass ratios of $M_R = 1 : 2$ and $M_R = 1 : 6$, respectively. As detailed above, for each pair, we run four simulations according to different pairs of orbital parameters E and L . This results in a total of 24 merging simulations. All the simulations are run by using the parallel version of the software code GADGET-2. All the N-body simulations were performed on the *zBox2* supercomputer (<http://www-theorie.physik.unizh.ch/dpotter/zbox2/>) at the University of Zurich. Each simulation was performed by using 16 CPU with a typical run time of 6 (24) hours for one-(two-)component simulation. The number of particles and the softening parameter of model galaxies in each merging pair are chosen as follows. For each pair, we set the number of particles of the low-mass progenitor as equal to $N_{L2} = 50000$ and we obtain the softening parameter, ϵ_L , from the relation between number of particles and optimal softening length presented in Sec. 2.4.1 (see Eq. 2.34). Given this softening value, we invert Eq. 2.34 to establish the number of particles of the most-massive progenitor, N_{L1} . This procedure allows us to keep the relative mean error on the discrete gravitational potential of each merging galaxy below $\sim 15\%$ (see Fig. 2.8), without overly increasing the computation time required for running the simulations. Each merging pair is identified by a different label as shown in column one of Tab. 3.2, with the quantities N_{L1} , N_{L2} , and ϵ_L being reported in columns two and three of the same table. We found that all merging pairs, with the exception of the pair $ML-6$ in the case $E = 0$ and $L = 0$, made merging after a time of $5 Gyr$ s. Although the initial conditions of the simulations were chosen according to the Binney and Tremaine (1994) prescription, for the pair $ML-6$ with $E = 0$ and $L = 0$, we found that the two model galaxies do not merge even when running the simulation over an Hubble time. The fact that for some initial conditions a given pair does not merge is explained by the fact that the allowed merging region of Binney and Tremaine (1994) is not uniquely defined by the values of $E = 0$ and $L = 0$, but depends also on the internal dynamical structure of the merging models (see e.g. Dantas et al. 2003, for a more extended discussion). Thus, we decided to simply remove the above case from the analysis.

3.1.2 Two-component models

For the two-component models, the characteristics of each merging pair are tabulated in Tab. 3.3. For each pair, columns two and three report the

Models (1)	G_1 (2)	G_2 (3)	N_{L1} (4)	N_{L2} (5)	ϵ_L (kpc) (6)	M_R (7)	L_R (8)
<i>ML</i> – 1	1	1	50000	50000	0.018	1 : 1	1 : 1
<i>ML</i> – 2	1	2	23436	50000	0.040	1 : 2	1 : 2
<i>ML</i> – 3	1	3	8365	50000	0.069	1 : 6	1 : 4
<i>ML</i> – 4	4	4	50000	50000	0.034	1 : 1	1 : 1
<i>ML</i> – 5	4	5	16696	50000	0.052	1 : 2	1 : 2
<i>ML</i> – 6	4	6	6912	50000	0.070	1 : 6	1 : 4

Table 3.2: Properties of discrete realizations of merging pairs in the case of one-component Sérsic models. *Col.* 1: label of the merging pair. *Cols.* 2 – 3: labels of the two progenitors in a given merging pair, according to the first column of Tab. 3.1. *Cols.* 4 – 5: number of particles in the stellar components of the two progenitors (see the text). *Col.* 6: softening length, ϵ_L , in units of *kpc*. *Col.* 7: progenitor mass ratio, M_R . *Col.* 8: progenitor luminosity ratio, L_R .

identification numbers of the two model galaxies, according to Tab. 3.1. As in the case of one-component models, for each pair we run four simulations according to the different pairs of initial orbital parameters E and L . Model one (four) is merged with itself and with models two (five) and three (six). Moreover, in order to investigate some further cases of merging between models resembling bright and ordinary early-type galaxies, we added two further merging pairs, consisting of models two and three and models three and four, respectively. This results in a total of eight two-component merging pairs, leading to 32 merging simulations. As for the one-component models, each pair is identified by a label, which is reported in Tab. 3.3.

The softening length and the number of particles of each merging model are chosen as follows. For the two progenitors in a given pair, we fix the number of particles of the corresponding dark matter haloes to $N_{D1} = 75000$ and $N_{D2} = 75000$, and we obtain the softening length of the dark matter component, ϵ_D from Eq. 2.34. The softening length of the stellar components, ϵ_L , is obtained as in the case of one-component models (fixing the number of particles of the less-massive progenitor to 50000, and then deriving the corresponding optimal smoothing length and the number of particles of the companion model galaxy from Eq. 2.34). For each pair, all the relevant quantities that characterize the discrete realization of the model galaxies are reported in Tab. 3.3.

As for one component models, all simulations are run for 5 *Gyrs*, since we found that simulations producing merged systems always do merge before this time, leading to virialized end-products. Only for the pair *MD* – 4 in

the case $E = -3$ and $L = 0$ and for the all the pairs with $E = 0$ and $L = 0$, we found that merging does not take place over an Hubble time. As discussed before, this can be explained by the dependence of the allowed merging regime from the internal dynamical structure of the progenitors. In the following, we do not analyze the cases that do not lead to form merged systems.

Models (1)	G_1 (2)	G_2 (3)	N_{L1} (4)	N_{L2} (5)	N_{D1} (6)	N_{D2} (7)	ϵ_L (kpc) (8)	ϵ_D (kpc) (9)	M_R (10)	L_R (11)
<i>MD</i> – 1	1	1	50000	50000	75000	75000	0.018	0.193	1 : 1	1 : 1
<i>MD</i> – 2	1	2	23436	50000	75000	75000	0.040	0.086	1 : 2	1 : 1
<i>MD</i> – 3	2	3	8365	50000	75000	75000	0.069	0.038	1 : 2	1 : 2
<i>MD</i> – 4	1	3	8365	50000	75000	75000	0.069	0.038	1 : 6	1 : 4
<i>MD</i> – 5	3	4	5521	50000	75000	75000	0.069	0.033	1 : 6	1 : 4
<i>MD</i> – 6	4	4	50000	50000	75000	75000	0.034	0.033	1 : 1	1 : 1
<i>MD</i> – 7	4	5	16696	50000	75000	75000	0.052	0.032	1 : 2	1 : 2
<i>MD</i> – 8	4	6	6912	50000	75000	75000	0.070	0.031	1 : 6	1 : 4

Table 3.3: Properties of the discrete realizations of merging pairs in the case of two-component Sérsic models. *Col.* 1: label of the merging pair. *Cols.* 2 – 3: labels of the two progenitors in a given merging pair, according to the first column of Tab. 3.1. *Cols.* 4 – 5: number of particles in the stellar components of the two progenitors. *Cols.* 6 – 7: number of particles in the dark matter halo components of the two progenitors. *Col.* 8: softening length of the stellar component, ϵ_L , in units of *kpc*. *Col.* 9: softening length of the dark matter halo, ϵ_D , in units of *kpc*. *Col.* 10: progenitor mass ratio, M_R . *Col.* 11: progenitor luminosity ratio, L_R .

3.2 Deriving the *observed* properties of merging remnants

We want to determine the structural and kinematic properties of the end-products of the merging simulations and compare them with observed properties of ETGs. To this aim, we start from the set of positions and velocities in each simulation output file produced by GADGET-2, applying the following procedure.

For both one- and two-component merging remnants (hereafter MRs), we select only the sub-set of (stellar and dark matter) particles which are still *bound* at the end of the simulation. A particle i is considered to be bound if

the following condition is fulfilled:

$$E_i = \frac{1}{2}|\mathbf{v}_i|^2 + \Phi(\mathbf{x}_i) \leq 0, \quad (3.2)$$

where \mathbf{x}_i and \mathbf{v}_i are the position and velocity vectors of the particle i and $\Phi(\mathbf{x}_i)$ is the gravitational potential of the system at the given position. Hereafter, all the quantities \mathbf{x}_i and \mathbf{v}_i are intended as computed with respect to the center of mass of the N-body system ¹.

In order to derive the scaling relations of merger remnants and their progenitors (see Sec. 3.4), we have to compute for each system the effective radius, R_{eL} , the mean effective brightness within this radius, $\langle\mu\rangle_e$, and the central velocity dispersion σ_0 . To this aim, for a given N-body system (either a progenitor or a MR), we first project the positions and velocities of all the particles on a given plane. We consider three different projections, corresponding to the three planes with cartesian coordinates (x, y) , (x, z) , and (y, z) . In other words, we mimic three cases where the line-of-sight of the observer would correspond to the three cartesian axes x , y and z . Using the luminosity of each particle (as derived from the numbers of particles and total luminosities reported in Tabs. 3.1, 3.2 and 3.3), we calculate the total B-band luminosity of the system, L_B . Then, we order all particles of stellar matter according to their distance to the center, and for each particle we calculate the luminosity enclosed within its projected radius. In this way, we obtain the growth curve of the luminosity of the system. We define the circularized effective (half-light) radius of the system, R_{eL} , as the projected radius that contains half of the its total luminosity. The mean effective surface brightness within R_{eL} is computed, according to its definition, as $\langle\mu\rangle_e = -2.5\log(L_B)/2\pi R_{eL}^2$. We note that the quantities R_{eL} and $\langle\mu\rangle_e$ provide non-parametric estimates of the structural properties of a given system. In the next section, we also discuss how alternative estimates of the effective radius and the corresponding mean surface brightness are derived by fitting a Sérsic law to the surface brightness profile of progenitors and merger remnants.

For a given adopted line-of-sight direction, γ , we calculate the projected central velocity dispersion, σ_0 , with the following formula:

$$\sigma_0 = \sqrt{\frac{1}{N_A} \sum_{i=1}^{N_A} (v_{\gamma_i} - \bar{v}_\gamma)^2}, \quad (3.3)$$

¹We use the expression N-body system to denote either a progenitor or a merger remnant.

where N_A is the number of the stellar particles within a given projected circular aperture of radius A , v_{γ_i} is the velocity of the i -th particle projected along the line-of-sight, and \bar{v}_γ is the mean velocity along the line-of-sight. To compare the properties of merger remnants with observational findings from previous works, we consider two apertures, a fixed size aperture of $A = A_J = 0.595/0.7 \text{ kpc}$, which is the one adopted from Jorgensen et al. (1996) when deriving the fundamental plane relation of ETGs in nearby clusters (transformed to a cosmology with $H_0 = 70 \text{ km s}^{-1} \text{ Mpc}^{-1}$), and an adaptive aperture of $A = A_B = R_{eL}/8$, which is to the aperture used from Bernardi et al. (2007) when deriving the Faber-Jackson relation of ETGs in the Sloan Digital Sky Survey (SDSS). We note that Eq. 3.3 is implicitly neglecting seeing effect on the velocity dispersion estimates.

For each progenitor and merger remnant, we take the average of all the measured quantities with respect to the three above mentioned projections, with the corresponding standard deviation providing an estimate of the *uncertainty* on each quantity.

3.3 Surface brightness profiles of N-body systems

3.3.1 Fitting the profiles with a Sérsic law

For a given N-body system, we derive the circularized surface brightness profile by applying a similar procedure to that outlined in the previous section. We order the particles of the stellar component according to their projected distance to the center. Then, we bin the projected distances, with each bin having the same number of particles. We considered 100 particles for each bin, verifying that the results do not change when varying the number of particles from 50 to 200. For each bin, we calculate the mean projected radius of the particles in that bin, R . The corresponding surface brightness value, $\mu(R)$, is obtained by dividing the total luminosity of the particles in the bin by its area. Hereafter, we refer to $\mu(R)$ as to the circularized surface brightness profile.

For a given N-body system, the circularized profile is fitted by a Sérsic law (see Sec. 2.2.1). The fit is performed by minimizing the χ^2 function:

$$\chi^2 = \sum_{i=1}^N \frac{[\mu(R_i) - \mu_{Sersic}(R_i)]^2}{(N - N_{par})}, \quad (3.4)$$

where N is the number of radial bins selected for the fitting (see below), and $N_{par}(= 3)$ is the number of free parameters of the Sérsic law, μ_{Sersic} , which are

the central surface brightness of the model, $\mu_{0_{best}}$, its effective radius, $R_{e_{best}}$, and the Sérsic index, n_{best} . The mean surface brightness with $R_{e_{best}}$, $\langle\mu\rangle_{e_{best}}$, is then computed from $\mu_{0_{best}}$ and $R_{e_{best}}$ using Eq. 23 in Ciotti and Bertin (1999). In the following analysis of correlations involving the effective radius and the mean surface brightness of model galaxies, we test the robustness of our results by adopting either the non-parametric quantities R_{e_L} and $\langle\mu\rangle_e$, or the best-fitted Sérsic parameters $R_{e_{best}}$ and $\langle\mu\rangle_{e_{best}}$. The Sérsic parameters are derived by fitting a given range of the surface brightness profile, from a minimum radius R_{min} to an outer radius R_{max} . Since the inner part of the profile is blurred by the softening parameter of the simulations, the value of R_{min} is set equal to three times the softening length ϵ_L . For the maximum radius R_{max} , we considered two cases. In the first case, we adopt an adaptive value of $R_{max} = 5 \cdot R_{e_L}$. This is the typical outer radius for the determination of the surface brightness profile of ETGs in very deep observations. Since from the observational viewpoint the surface brightness profile of ETGs is more often derived with a constant surface brightness threshold rather than adopting an adaptive maximum radius, we also fit the profiles by a value of R_{max} corresponding to a surface brightness limit of $\mu_B < 27 \text{ mag arcsec}^{-2}$. In the following sections, we show that the results do not change significantly when fitting the profiles within either one or other radial range.

3.3.2 Analysis of the surface brightness profiles

Fig. 3.1 shows the surface brightness profiles of the progenitors for merging simulations with one-component models. For each progenitor, we show the measured and fitted profiles, as well as the fitting residuals in units of mag arcsec^{-2} . The fit was performed with $R_{max} = 5 \cdot R_{e_L}$. Fig. 3.2 shows the fitting results for the same progenitors, when a constant surface brightness cut is applied. In both cases, as expected by construction, the Sérsic fit well reproduces the estimated surface brightness profiles. We verified that this holds for all the one-component progenitors. The best-fitting parameters of the Sérsic law, $R_{e_{best}}$ and n , turned out to be fully consistent, within a few percent, with the input parameters of the simulations. We also found that the best-fitting parameters of the Sérsic model do not change significantly (by less than 1%), when adopting different choices of R_{max} .

For the two-component progenitors, we performed the same tests as for the one-component case. Fig. 3.3 show the surface brightness profiles of the progenitors. The fit is performed in the radial range $3 \cdot \epsilon_L < R < 5 \cdot R_{e_L}$, while in Fig. 3.4 we show the fitting results when a constant surface brightness threshold of $27 \text{ mag arcsec}^{-2}$ is adopted. As expected, structural parameters are fully consistent with the input parameters of the models, and do not

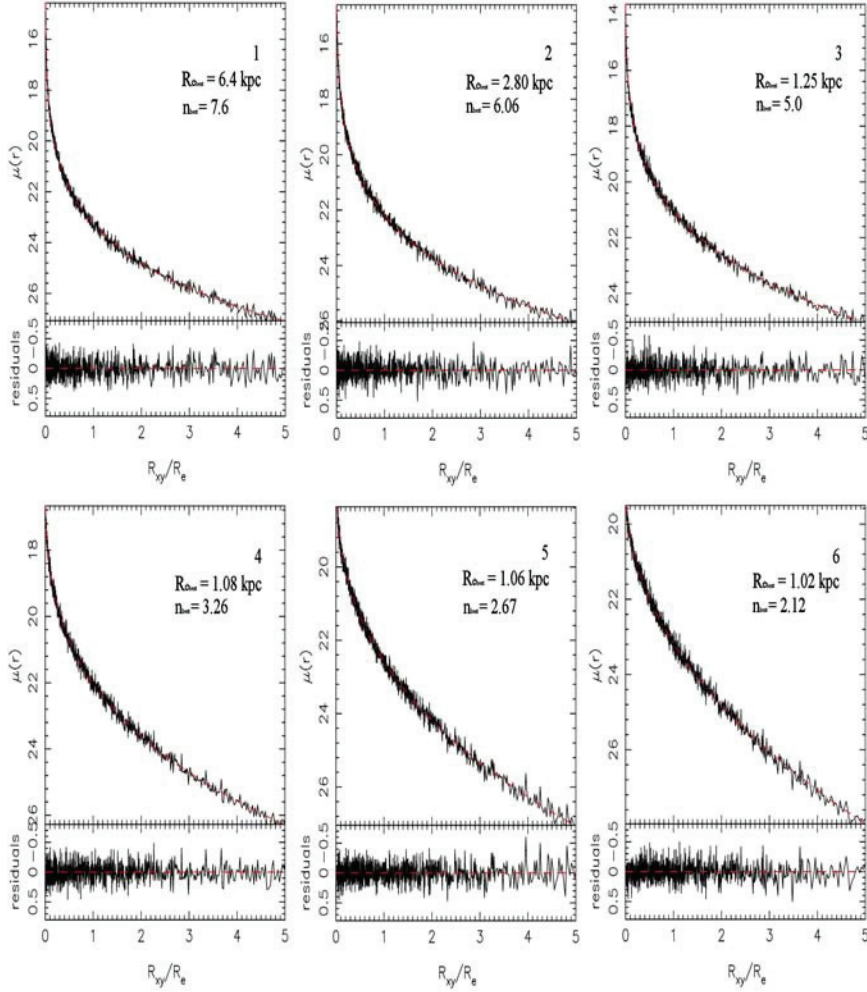


Figure 3.1: Surface brightness profile, $\mu(R)$, for all one-component progenitors. Red curves represent the best fitted Sérsic profile in the radial range $3 \cdot \epsilon_L < R < 5 \cdot R_{eL}$ (kpc). Bottom panels show the residuals between the profile and the best fit. The label of each progenitor (see Tab. 3.1) is reported in the upper-right corner of each plot together with the best fitting parameters $R_{e_{best}}$ and n_{best} .

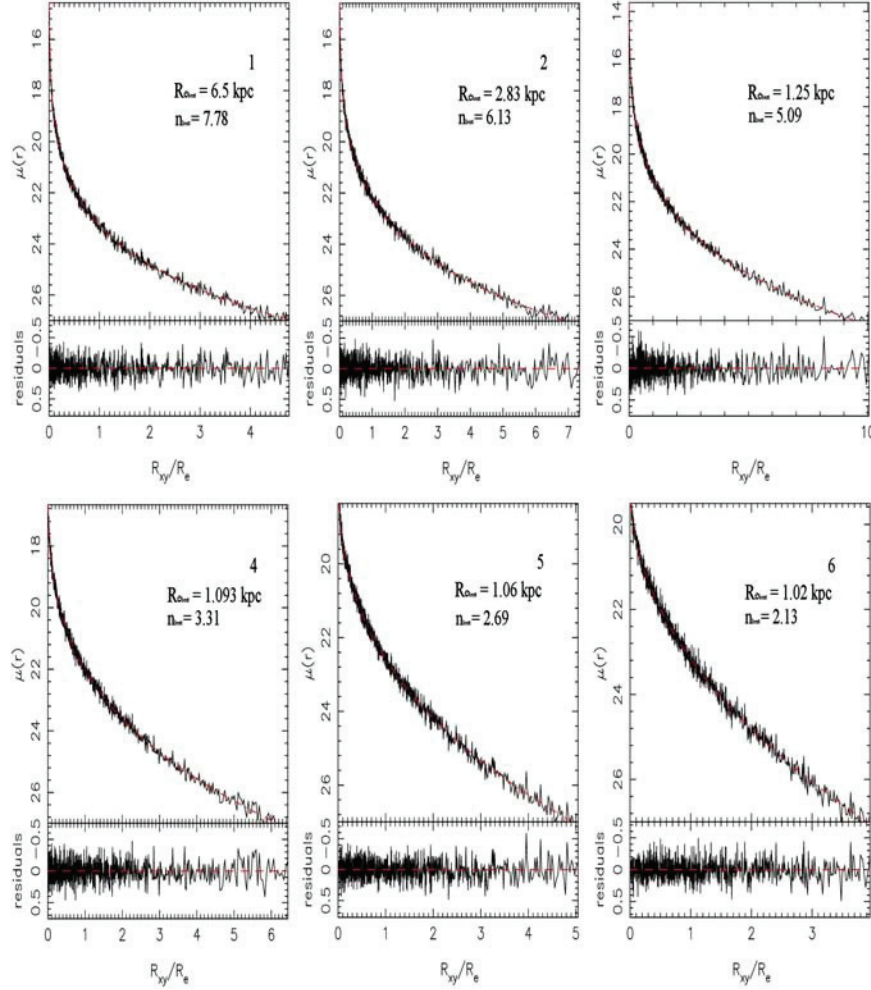


Figure 3.2: Surface brightness profile, $\mu(R)$ for all one-component progenitors. Red curves represents the best fitted Sérsic profile performed on particles with $\mu_B < 27 \text{ mag arcsec}^{-2}$. The label of each progenitor (see Tab. 3.1) is reported in the upper-right corner of each plot together with the best fitting parameters R_{best} and n_{best} .

change when applying a different radial range to fit the profiles. As also expected from the symmetry of the models for both one- and two-component progenitors, we found that all fitted quantities do not depend on the two-dimensional projection where the surface brightness profile is derived.

The surface brightness profiles of the MRs of one-component simulations were analyzed in the same way as the progenitors. Some fitting examples are presented in Figs. 3.5 and 3.6 (Figs. 3.7 and 3.8) for initial conditions $E = -3$ and $L = 0$ ($E = 0$ and $L = 2$) for the two fitted radial ranges, respectively. The figure shows that fitting residuals are always smaller than a few tenths of magnitude, with no systematic trend as a function of R . This implies that the remnants are well described by the Sérsic law, with this result holding for all the merger remnants analyzed here. All best fitted parameters, $R_{e_{best}}$, $\langle\mu\rangle_{e_{best}}$ and the Sérsic index n_{best} , were found not to depend significantly on the fitting method as shown in the following section.

For the two-component simulations, we basically found the same results as in the one-component case. Some fitting examples of MR's surface brightness profiles are shown in Figs. 3.9 and 3.10. All the profiles turn out to be well described by the Sérsic law and also in this case we found that best fitted parameters do not change significantly for different choices of R_{max} .

3.4 Results

It is well known that observed properties of ETGs, such as radius, luminosity, shape parameter, and velocity dispersion, are tightly correlated. In this section, we derive several correlations for the merger remnants of the one- and two-component Sérsic models, comparing them with observational results from previous works.

3.4.1 Fundamental Plane

One the most well known scaling laws of ETGs is the so-called Fundamental Plane relation (hereafter FP), which is usually expressed as a relation among R_e , $\langle\mu\rangle_e$ and the line-of-sight central velocity dispersion σ_0 (Djorgovski and Davis 1987; Dressler et al. 1987). The main characteristics of the FP are its small intrinsic dispersion, in the range of 0.06 – 0.13dex in R_e (Jorgensen et al. 1996; Pahre et al. 1998), and its tilt, i.e. the deviation of the FP slopes from those expected for a virialized family of homologous systems with constant mass-to-light ratios (Busarello et al. 1997). The origin of the tilt is still not clear, with possible explanations involving (i) a variation of the mass-luminosity ratio of ellipticals as a function of mass (Djorgovski

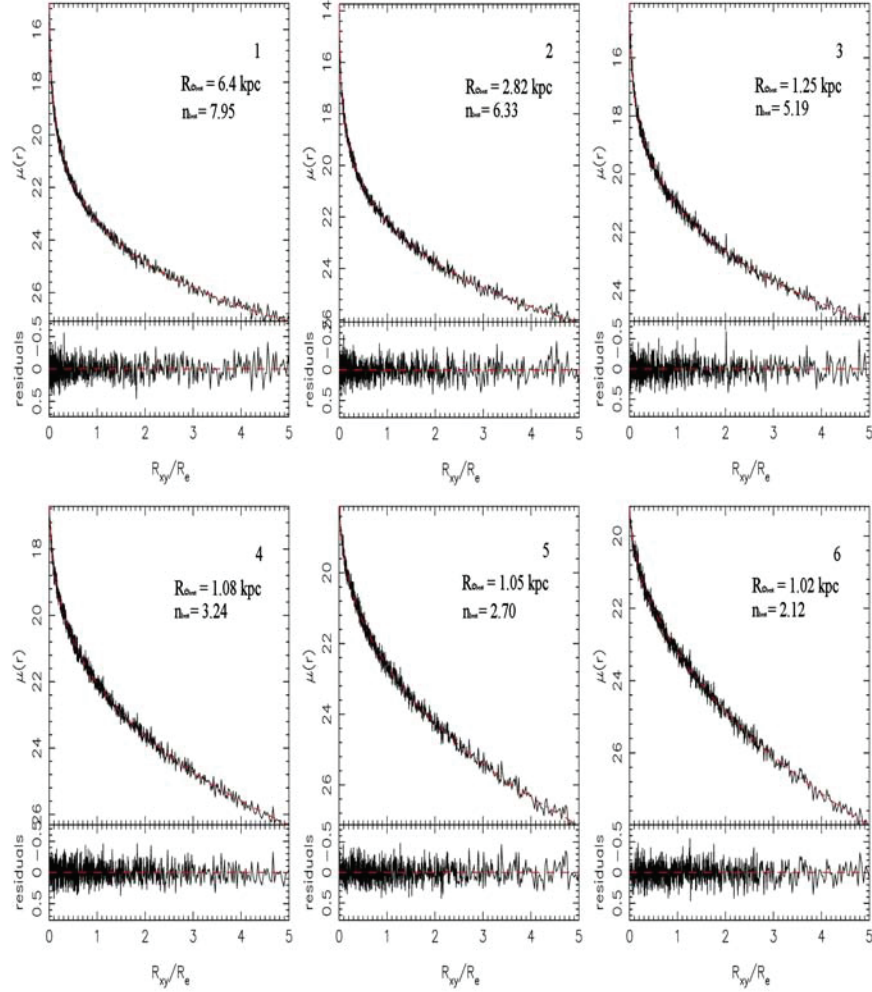


Figure 3.3: Surface brightness profile, $\mu(R)$, for all two-component progenitors. Red lines represents the best fitted Sérsic law in the radial range $3 \cdot \epsilon_L < R < 5 \cdot R_{e_L}$ (kpc). Bottom panels show the residuals between the profile and the best. The label of each progenitor (see Tab. 3.1) is reported in the upper-right corner of each plot together with the best fitting parameters $R_{e_{best}}$ and n_{best} .

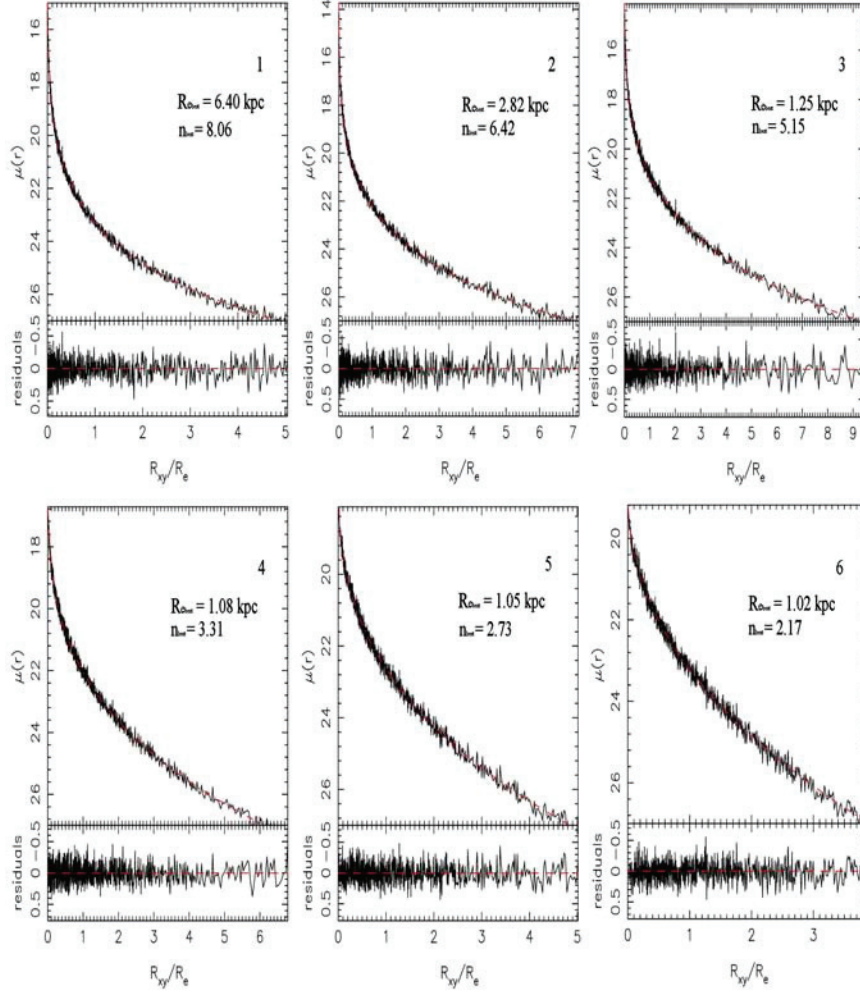


Figure 3.4: Surface brightness profile, $\mu(R)$ for all two-component progenitors. Red curves represent the best fitted Sérsic profile performed on particles with $\mu_B < 27 \text{ mag arcsec}^{-2}$. Bottom panels show the residuals between the profile and the best fit. The label of each progenitor (see Tab. 3.1) is reported in the upper-right corner of each plot together with the best fitting parameters $R_{e,best}$ and n_{best} .

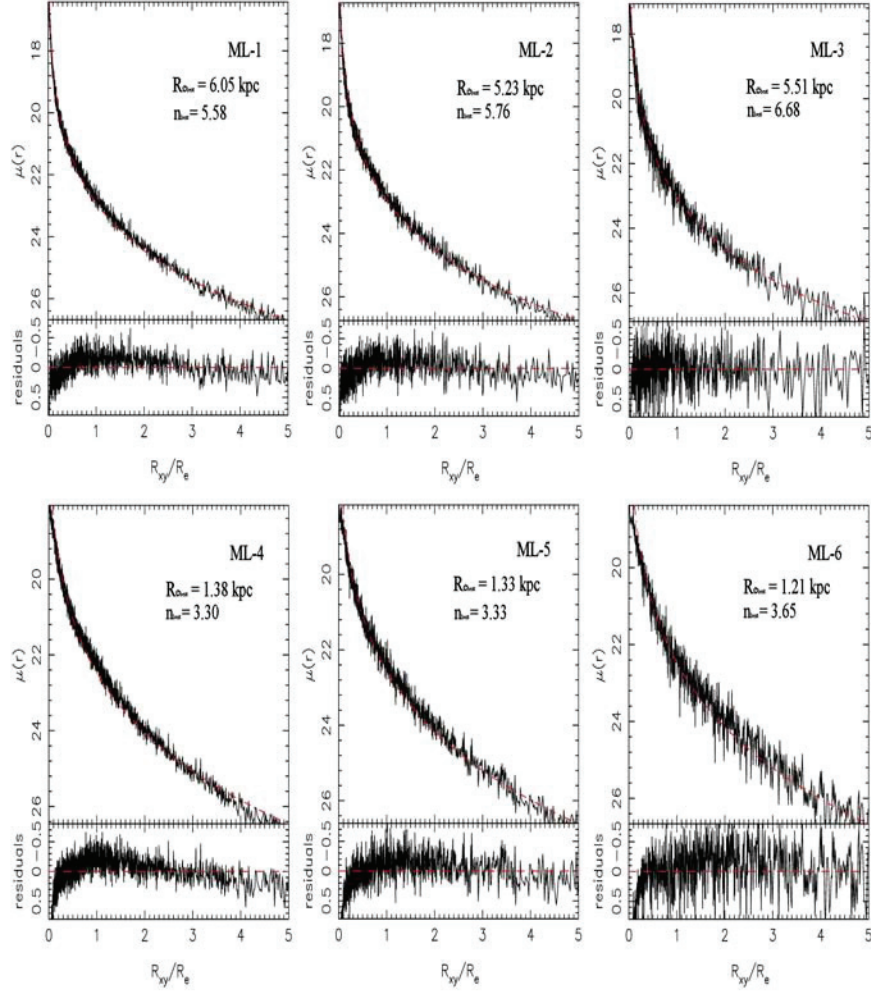


Figure 3.5: Surface brightness profile, $\mu(R)$, for one-component MRs. Simulations are performed setting the initial orbital parameters as $E = -3$ and $L = 0$. Red lines represents the best fitted Sérsic profile performed on the radial range $3 \cdot \epsilon_L < R < 5 \cdot R_{e_L}$ (kpc). Bottom panels show residuals between the profile and the best fit profile. The label of each progenitor (see Tab. 3.2) is reported in the upper-right corner of each plot together with the best fitting parameters R_{best} and n_{best} .

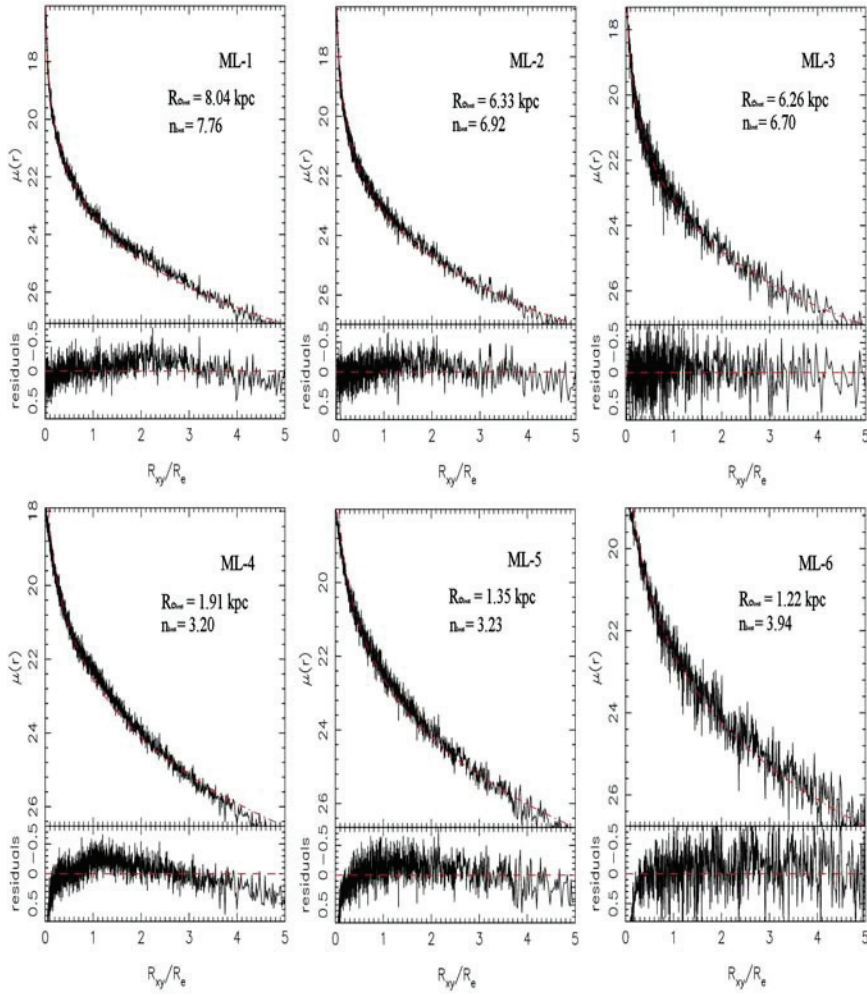


Figure 3.6: Same as Fig. 3.5 but for initial orbital parameters as $E = -3$ and $L = 2$.

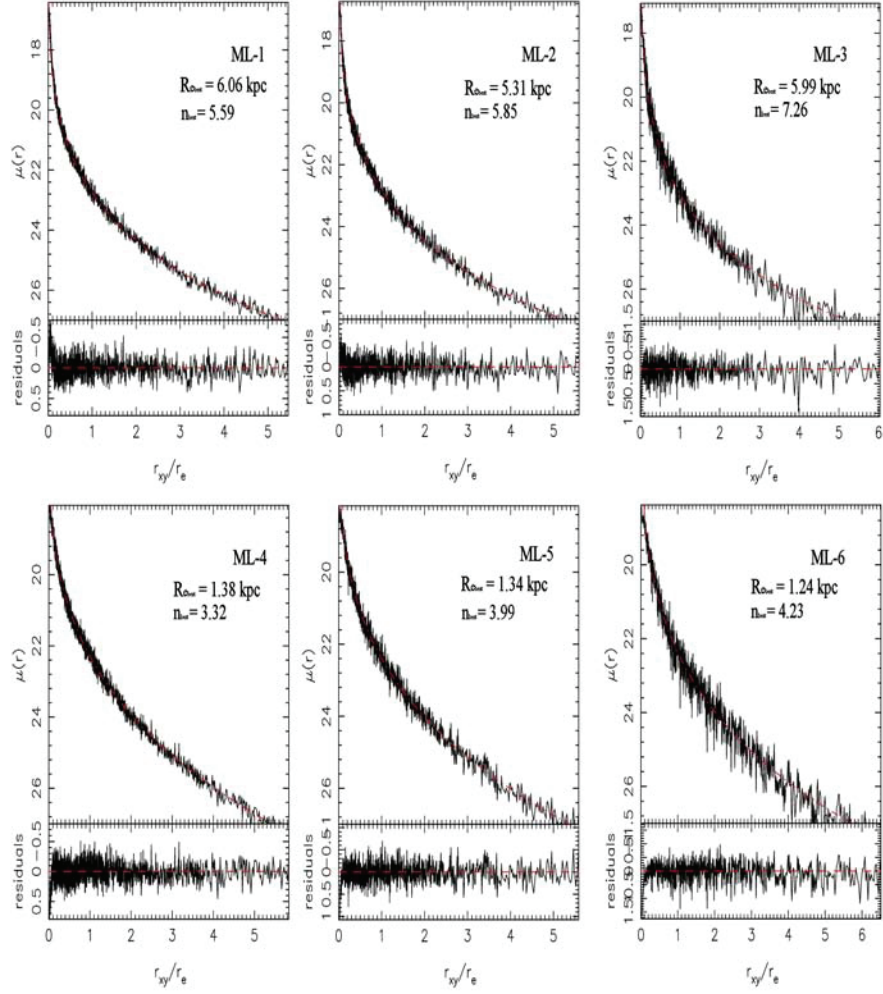


Figure 3.7: Surface brightness profile, $\mu(R)$, for one-component MRs. Simulations are performed setting the initial orbital parameters as $E = -3$ and $L = 0$. Red lines represents the best fitted Sérsic profile performed on particles with $\mu_B < 27 \text{ mag arcsec}^{-2}$. Bottom panels show the residuals between the profile and the best fit. The label of each progenitor (see Tab. 3.2) is reported in the upper-right corner of each plot together with the best fitting parameters $R_{e_{\text{best}}}$ and n_{best} .

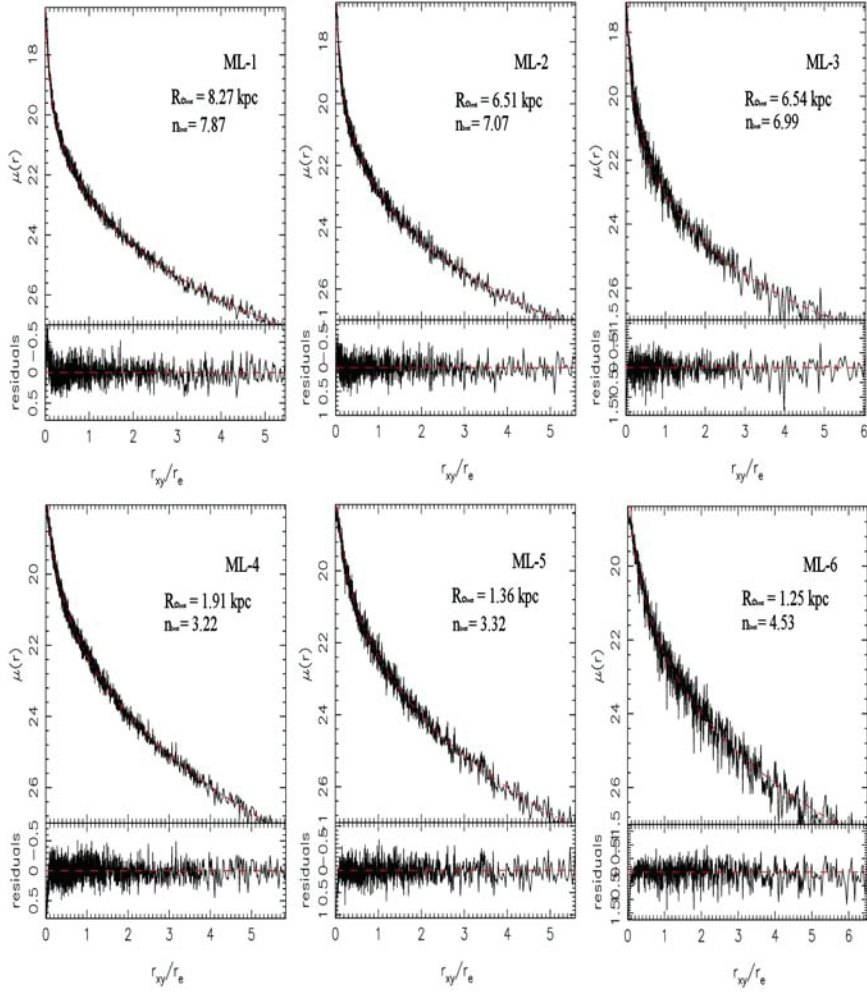


Figure 3.8: Same as Fig. 3.7 but for initial orbital parameters as $E = -3$ and $L = 2$.

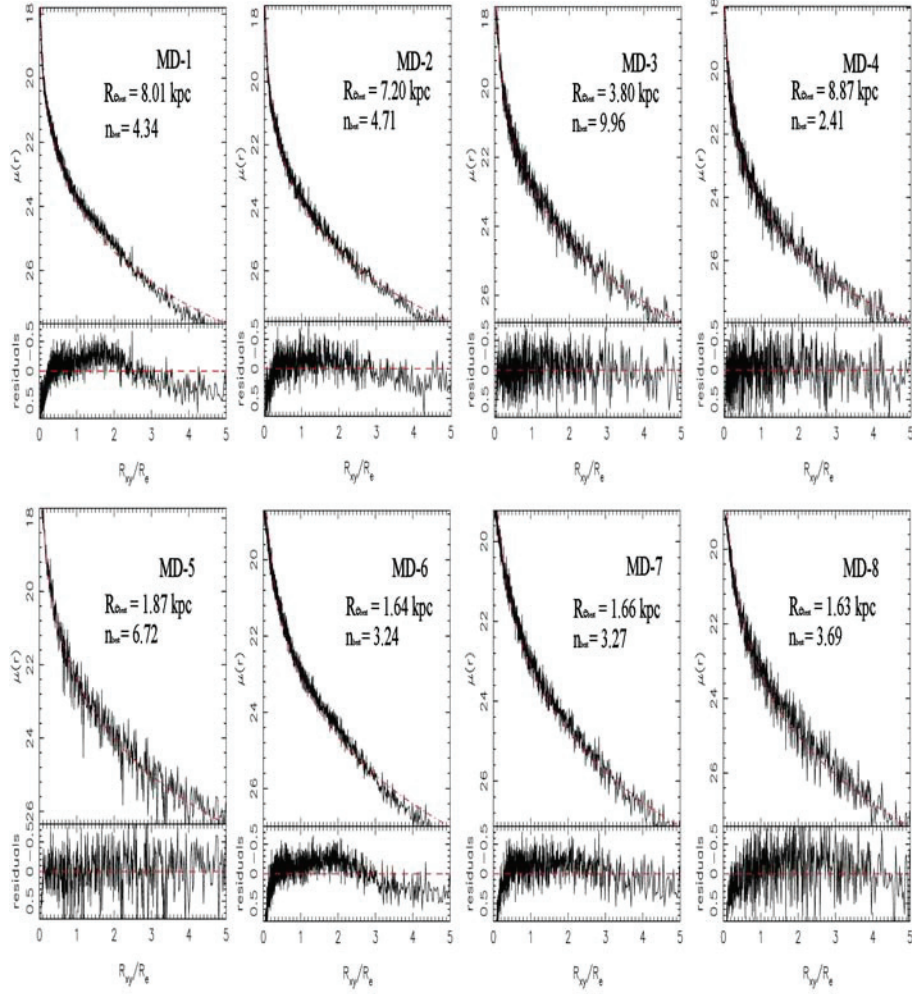


Figure 3.9: Surface brightness profile, $\mu(R)$, for two-component MRs. Simulations are performed setting the initial orbital parameters as $E = -3$ and $L = 0$. Red lines represents the best fitted Sérsic law in the radial range $3 \cdot \epsilon_L < R < 5 \cdot R_{eL}$ (kpc). Bottom panels show the residuals between the profile and the best fit. The label of each progenitor (see Tab. 3.3) is reported in the upper-right corner of each plot together with the best fitting parameters $R_{e_{best}}$ and n_{best} .

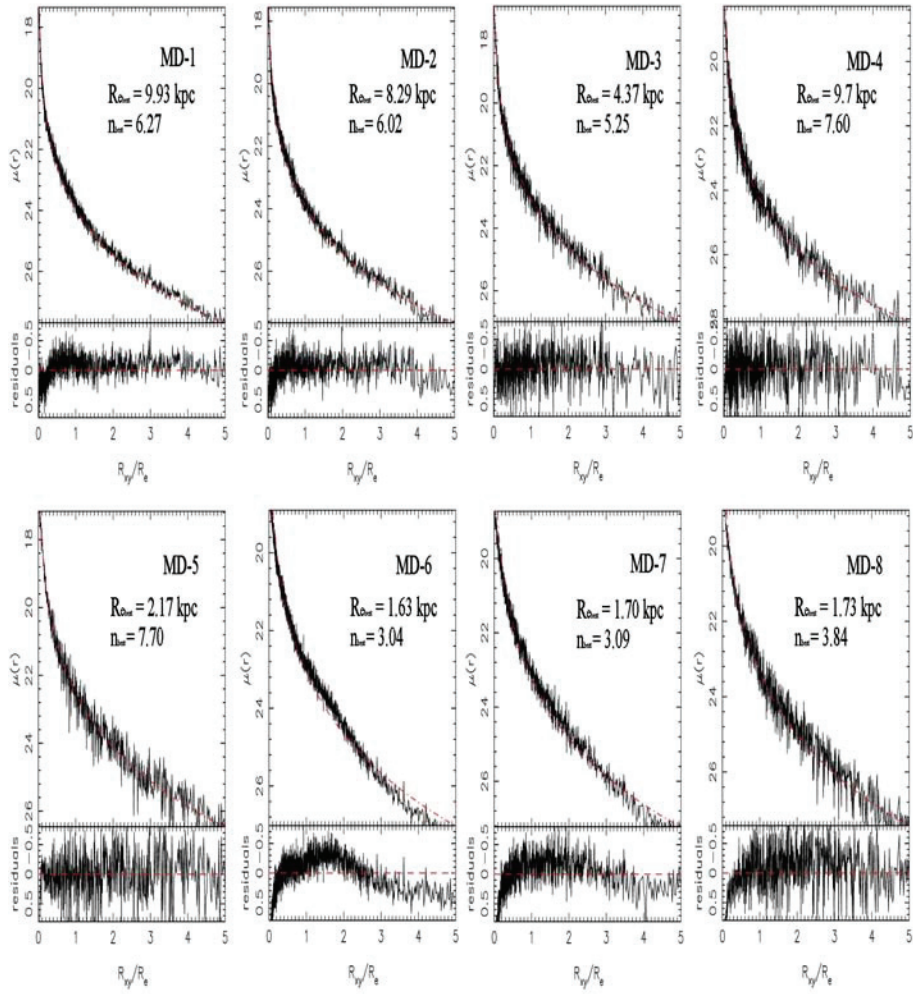


Figure 3.10: Same as Fig. 3.9 but for initial orbital parameters as $E = -3$ and $L = 2$.

and Santiago 1993; Pahre et al. 1995), and/or a breaking of the homology assumption (e.g. Ciotti et al. (1996); Busarello et al. (1997); Graham and Colless (1997); Bekki (1998)). Several works have addressed the origin of the FP relation using N-body simulations. Capelato et al. (1995) showed that the FP can naturally arise from dissipationless galaxy-galaxy merging. They considered only one-component galaxy models following the King profile. On the other hand, Dantas et al. (2002) showed that single collapse events of spherical, one-component systems produce nearly homologous families of objects. Dantas et al. (2003) extended the investigation of Capelato et al. (1995), analyzing the dissipation-less merging of two-component Hernquist models up to two merging generations. They still found that the two-component merger remnants follow a relation similar, but significant steeper, than the observed FP. Nipoti et al. (2003) also explored the effect of dissipationless merging on the FP. They produced several merging generations, starting from progenitors described by equal-mass, spherical, isotropic and one-component Hernquist models. Merging generations were obtained by repeating the merging of the end products obtained from the previous merging step. They also investigated to some extent the merging of seed galaxies described by two-component Hernquist models, with a dark matter halo more massive and less concentrated than the stellar component. Nipoti et al. (2003) also showed that merging end-products well reproduce the observed FP.

In Fig. 3.11, we present the edge-on projection of the FP for all the progenitors and MRs obtained for both the one- and two-component models. The effective parameters are estimated from the non-parametric approach described in Sec. 3.2. In order to consistently compare the simulation results with the observational findings of Jorgensen et al. (1996), velocity dispersions of both progenitors and merger remnants were derived here in fixed size aperture, as detailed in Sec. 3.2. In the figure, progenitors are represented by using black circles while other colors refer to different values of the initial orbital parameters, as indicated in the bottom right corner of the figure. Open symbols indicate one-component models, while filled symbols represent two-component systems. The solid and dashed blue lines represent the FP and its $1-\sigma$ scatter, as measured from Jorgensen et al. (1996) for ETGs in clusters of galaxies at $z \sim 0$ in the r-band. To convert the luminosities of our model from B-band to r-band we used the color-magnitude relation from Mercurio et al. (2006), derived for galaxies in the Shapley super cluster ($z \sim 0.05$). Figs. 3.13 and 3.12 are the same as Fig. 3.11, but show effective parameters derived from the Sérsic fitting of the surface brightness profiles, for the case where $R_{max} = 5R_{eL}$ and the case where a fixed surface brightness cut in the profile is adopted (see Sec. 3.3.1). In agreement with previous

studies (see above), the figures show that dissipationless merging of one- and two-component models is able to reproduce the observed FP of elliptical galaxies. MRs follow a FP relation parallel to that of the progenitors, though slightly offset towards the bottom-right part of the plot. However, all the points are well within the observed scatter of the FP. The result is the same for both one- and two-component models, and does not depend on the initial merging conditions (values of E and L).

3.4.2 Kormendy relation

One projection of the FP is the correlation between $\langle\mu\rangle_e$ and $\log(R_e)$ also known as Kormendy relation (hereafter KR Kormendy 1977). The distribution of ETGs in the $\langle\mu\rangle_e - R_e$ plane (or equivalently in the plane $M - \langle\mu\rangle_e$), reveals the existence of two distinct families: the *ordinary* family of ellipticals, and the *bright* family, consisting of the most luminous ETGs (Capaccioli et al. 1992). As suggested by Capaccioli et al. (1992), the $\langle\mu\rangle_e - \log(R_e)$ diagram might be interpreted as an Hertzsprung-Russell diagram for ETGs, with elliptical galaxies reaching the bright end of the $\langle\mu\rangle_e - R_e$ relation through successive mergers of low-mass systems, according to a hierarchical merging scenario where small galaxies are the building blocks of more massive systems. Using numerical simulations, Evstigneeva et al. (2004) investigated if dissipationless merging of low-mass systems is able to produce systems that lie on the KR of bright galaxies. They modeled dwarf ETGs with a luminous component embedded in more extended dark matter halo. The luminous component was modelled using the potential-density pair of Hernquist (1990), while the dark halo density profile was represented as a truncated isothermal sphere (Hernquist 1993b). They found that final merging products are not moved along the KR, concluding that ETGs are not formed by merging dwarfs, unless a considerable amount of dissipation is involved in the merging. On the other hand, simulating the merging of galaxy pairs that lie on the KR of bright galaxies, they found the end products to still lie on the KR, once the observational scatter is taken into account. Using N-body simulations, Nipoti et al. (2003) also concluded that merging end-products of bright ETG models do not reproduce the KR, having too large effective radii.

In Fig. 3.14 we present the $M_B - \langle\mu\rangle_e$ relation for all progenitors and MRs, considering both the one- and two-component simulations. The effective parameters are obtained from the non parametric approach described above (see Sec. 3.2). Symbols are the same as in Fig. 3.11, with solid and dashed blue lines representing the KR and its observational scatter in the B-band from Graham and Guzmán (2003b). In Figs. 3.15 and 3.16, we also show the

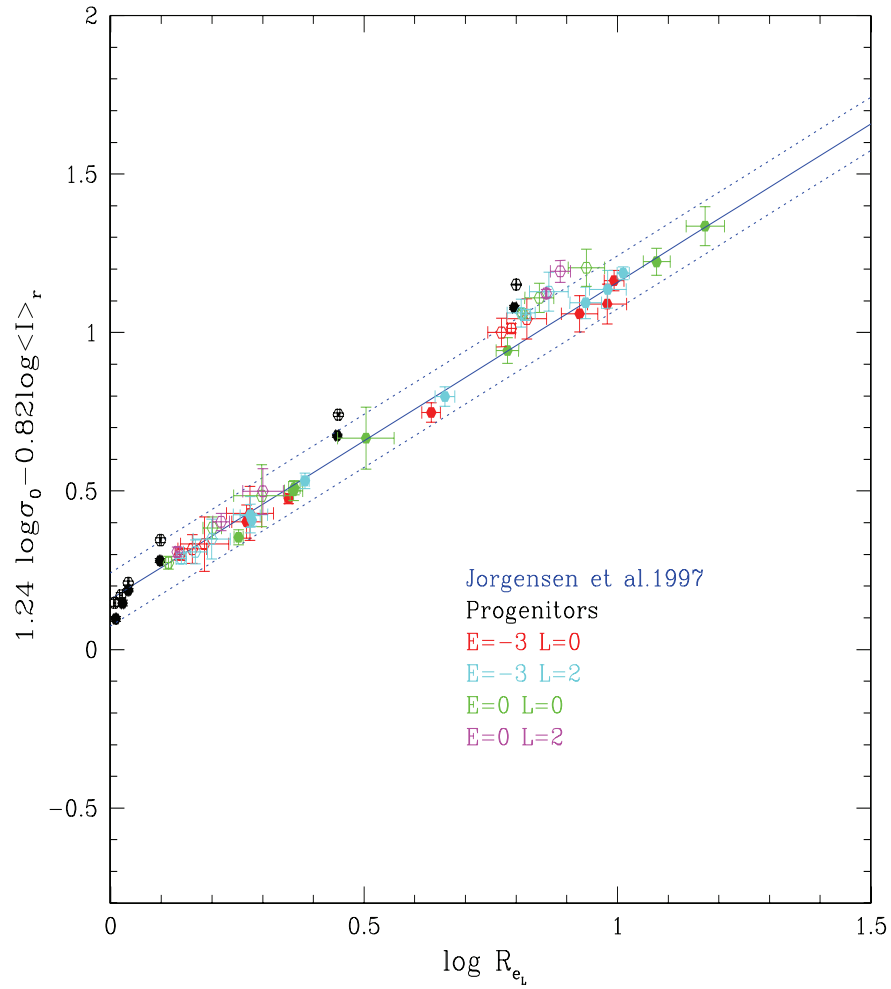


Figure 3.11: The edge-on fundamental plane relation for all progenitors and MRs obtained from non-parametric estimates of effective parameters. Open symbols represent one-component progenitors and MRs, while filled points represent two-component progenitors and MRs. In the bottom right corner of the figure we report the meaning of different colors. The solid and dashed lines represent the observed FP relation and its scatter from Jorgensen et al. (1996).

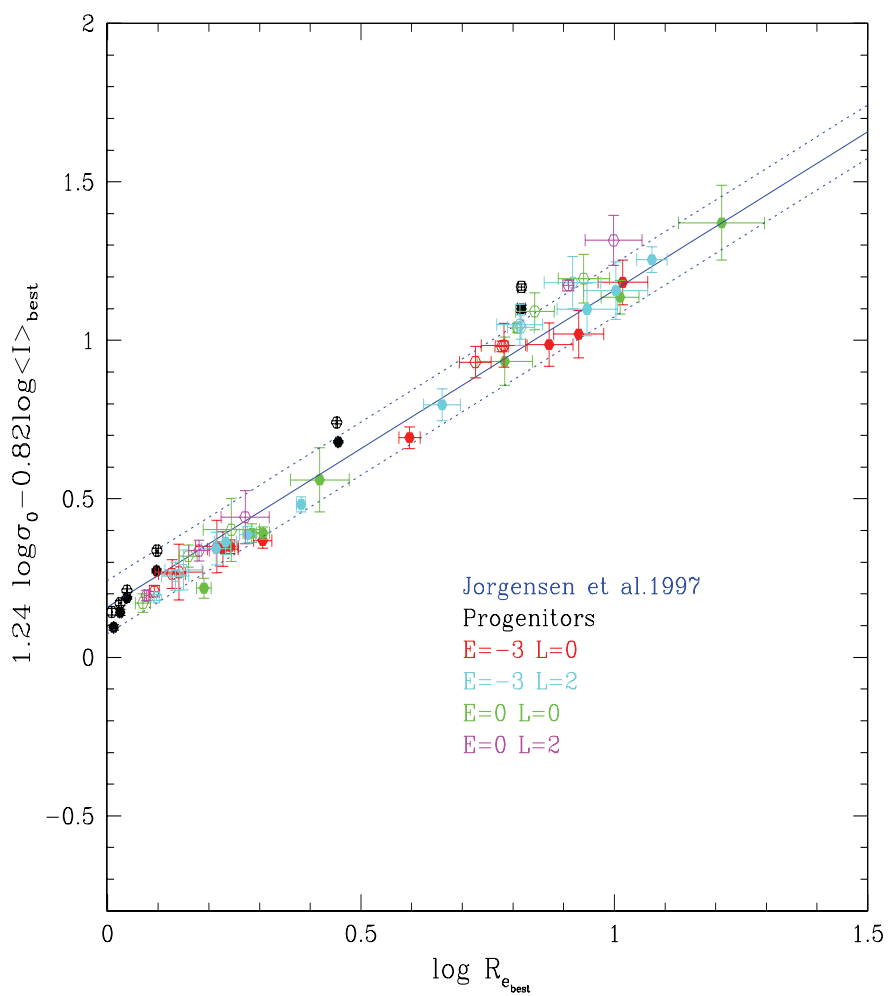
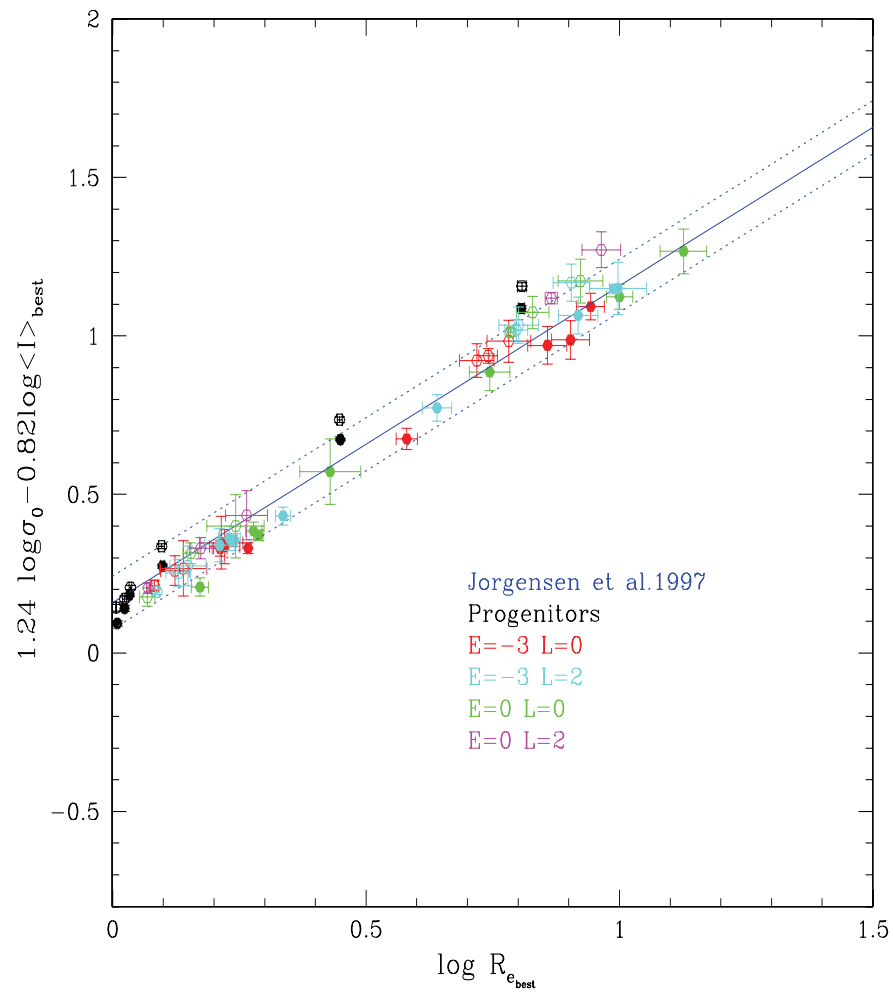


Figure 3.12: Same as Fig. 3.11 with structural parameters derived from a Sérsic fit of the surface brightness profile (cut at $\mu(R_{max}) = 27 \text{ mag arcsec}^{-2}$).

Figure 3.13: Same as Fig. 3.12 for $R_{max} = 5R_{eL}$.

same KR plot as in Fig. 3.14, but using photometric quantities obtained by the Sérsic fit of the surface brightness profiles considering different choices of R_{max} (see Sec. 3.3.1). Some global trends can be seen in the figures. Merging products have a brighter absolute magnitude, M_B , and a larger value of the mean surface brightness, $\langle\mu\rangle_e$. This is basically due to the fact that merging blows up the progenitor, increasing their radius and producing a fainter mean surface brightness value. The amount of blowing-up depends on the initial orbital energy of the simulation, being larger for $E = -3$ where more orbital energy is pumped into the system. In agreement with what found by Evstigneeva et al. (2004), after one merging generation, massive galaxy models ($M_B < -18$) are moved along the observed KR. In contrast to previous studies (see e.g. Evstigneeva et al. 2004; Nipoti et al. 2003), we find that one merging generation is not able to move low-mass galaxy models far away for the observed locus of galaxies in the M_B - $\langle\mu\rangle_e$ plane. Our simulation do not exclude the possibility of making bright elliptical galaxies by merging dwarf systems. In fact, as shown by De Lucia et al. (2006), massive ETGs result from several dissipationless mergers of low mass systems, while low mass systems ($M < 10^{11} M_\odot$) experienced on average only one dissipationless major merging event. As shown from our simulations, this prevents low mass systems to *escape* from the region occupied by ordinary galaxies in the $R_e - \langle\mu\rangle_e$ plane. As for the FP, we see that one- and two-component models show the same behaviour. Moreover, the results do not depend on the choice of the radial range where the fit of the surface brightness profile is performed, and does not change for different initial conditions of the simulations.

3.4.3 Faber-Jackson relation

The luminosity and central velocity dispersion of ETGs are strongly correlated (see e.g. Faber and Jackson 1976). The relation, also known as Faber-Jackson (hereafter FJ) relation, is approximately linear when considering magnitude and logarithm of velocity dispersion. Davies and Illingworth (1983) also suggested that a double power-law fit actually provides a better representation of the FJ relation. Recently, using a large sample of ETGs in the Sloan Digital Sky Survey, Bernardi et al. (2007) found the following correlation between σ_0 and the r-band absolute magnitude, M_r :

$$\log(\sigma_0) = 2.184 - 0.104(M_r + 21), \quad (3.5)$$

where σ_0 is measured within an aperture with adaptive size of $R_e/8$. The effect of dissipation-less merging on the FJ relation has been investigated by N-body simulations from Nipoti et al. (2003) (see Sec. 3.4.1). They found

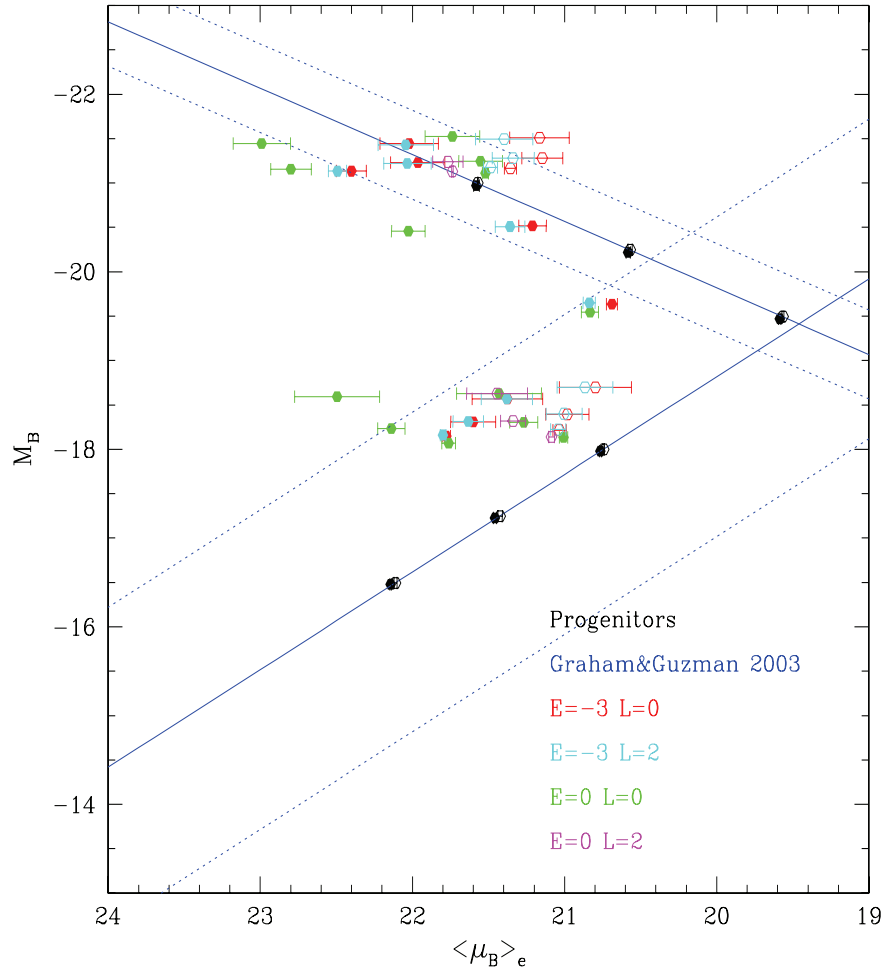


Figure 3.14: The non parametric $M_B - \langle \mu_B \rangle_e$ relation for all progenitors and MRs. Open symbols represent one-component progenitors and MRs, while filled circles represent two-component progenitors and MRs. In the bottom right corner of the figure we report the meaning of different colors. Solid and dashed lines represent the KR and its 1σ scatter from Graham and Guzmán (2003b).

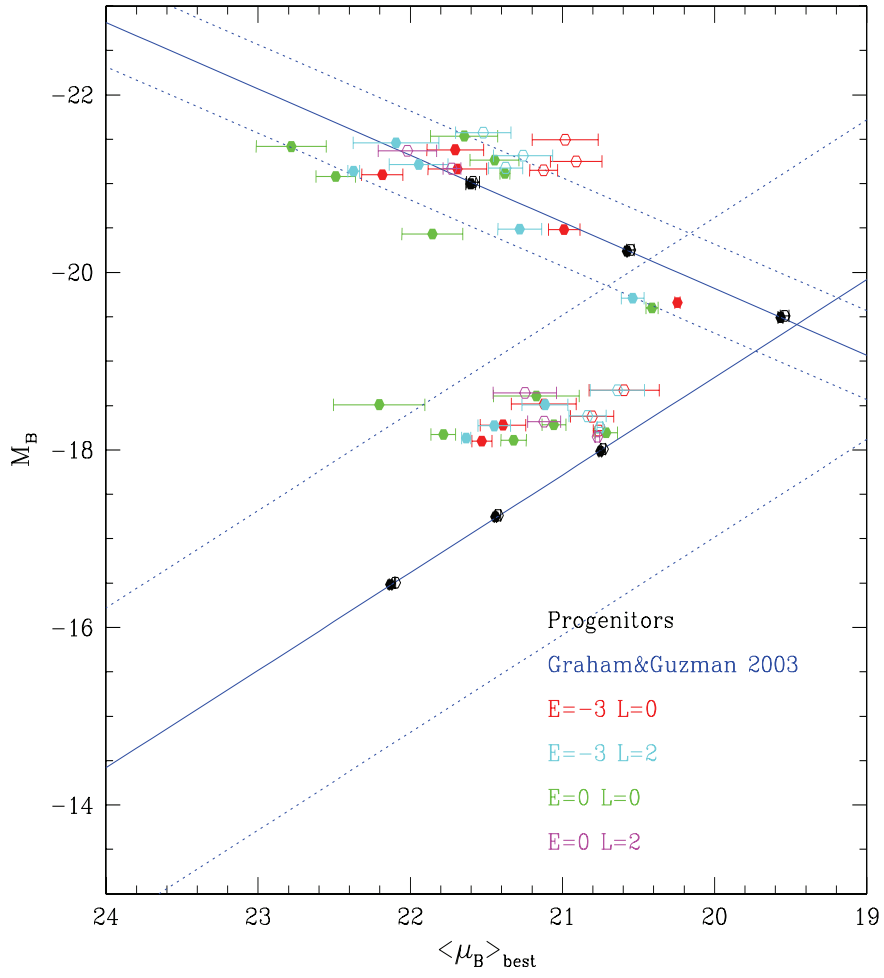


Figure 3.15: $M_B - \langle \mu_B \rangle_e$ relation of best-fitted parameter obtained performing the fit of the surface brightness profile with $R_{max} = 5 \cdot R_{e_L}$. Colors and symbols are the same as Fig. 3.14.

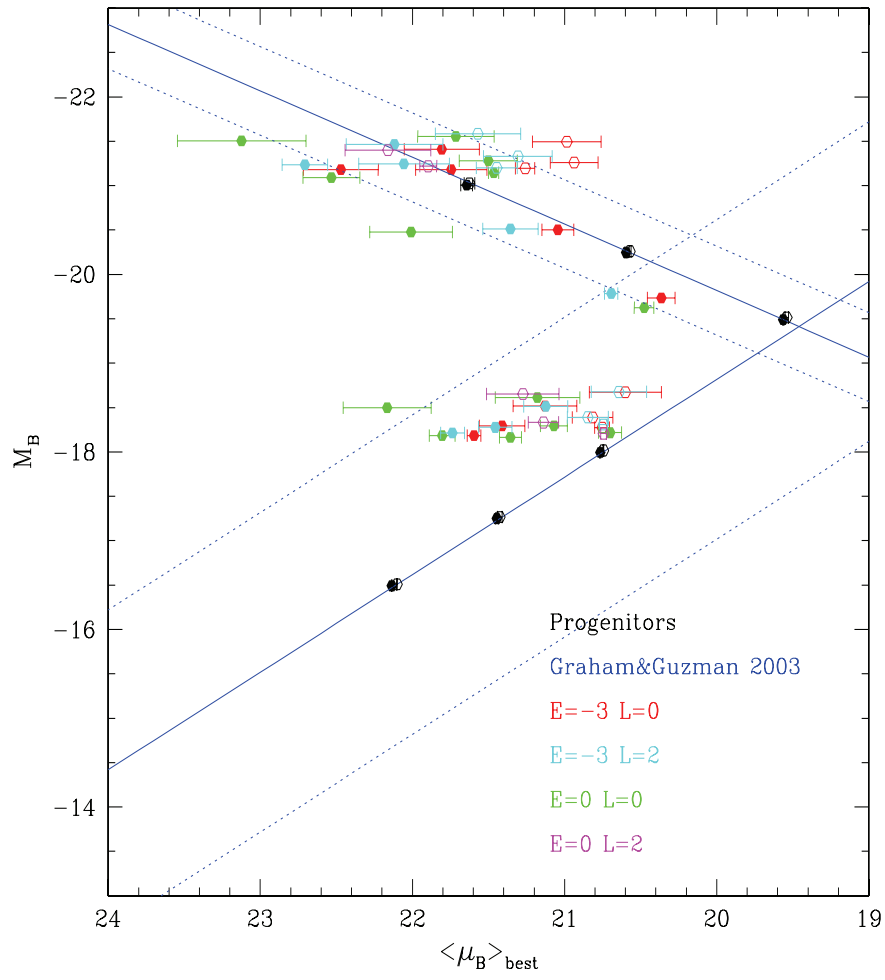


Figure 3.16: The $M_B - \langle \mu_B \rangle_e$ relation for best-fitted parameters as obtained when a constant surface brightness cut is applied in the fit of the surface brightness profile. Colors and symbols are the same as Fig. 3.14.

that merging end-products have σ_0 lower than that predicted by the observed FJ relation and that the discrepancy is even larger for merging simulations with significant angular momentum.

In Fig. 3.17 we present the $\sigma_0 - M_B$ relation of all our progenitors and MRs, and compare it with that of Bernardi et al. (2007) (see above). Values of σ_0 for the N-body simulations are measured within the same adaptive aperture as for the observations (see Sec. 3.2). Symbols are the same as in Fig. 3.11, with solid and dashed blue lines representing the FJ relation and its observational 1σ scatter from Bernardi et al. (2007). We converted B -band magnitudes of our models to r -band by using the $B - R$ color-magnitude relation of ETGs from Mercurio et al. (2006) and a constant color term of $r - R = 0.37$ from Fukugita et al. (1995). The plot shows that there is a mismatch between the slope of the L - σ relation for the progenitors and the observed slope of the FJ relation. This difference might be explained by the fact that the mass-to-light ratios we used to normalize the model parameters (see Sec. 2.3) were appropriate for dynamical models of ETGs that are built to match galaxy observed properties within one effective radius (see Cappellari et al. (2006)). A slight different mass-to-light versus mass relation might easily explain the effect seen in Fig. 3.17, bringing back the progenitors on top of the observations. The somewhat different trends we also see in the figure for bright ($M_B < -18$) and ordinary galaxies ($M_B > -18$) is likely explained by the fact that we considered two simple linear relations to describe the distribution of galaxies in the R_e - $\langle\mu\rangle_e$ plane (instead of a more continuous relation see Graham et al. (2006b)). However, when looking at MRs, it is quite remarkable that merged two-component models are very consistent with the observed relation. We note that also in this case initial conditions of the simulations do not change significantly the results.

3.4.4 The $M_B - n$ relation

As mentioned in Sec. 2.1.1, the Sérsic index n of ETGs correlates with galaxy luminosity, in the sense that brighter galaxies tend to have larger n (Caon et al. 1993; Graham et al. 1996; Graham and Guzmán 2003b), indicating *structural non-homology* in the class of ETGs, i.e. the fact that the profile slope of ETGs changes systematically along the galaxy sequence (see e.g. Davies 1988; Capaccioli 1989; Caon et al. 1993; Young and Currie 1994; D’Onofrio et al. 1994; Prugniel and Simien 1997). Since our N-body simulations are based on galaxy models described by the Sérsic galaxy profile, we can investigate in detail, how dissipation-less merging affects the luminosity- n relation of ETGs. In Figs. 3.18 and 3.19, we present the luminosity-size relation, $M_B - n$, for all progenitors and MRs. In the first plot, the best-

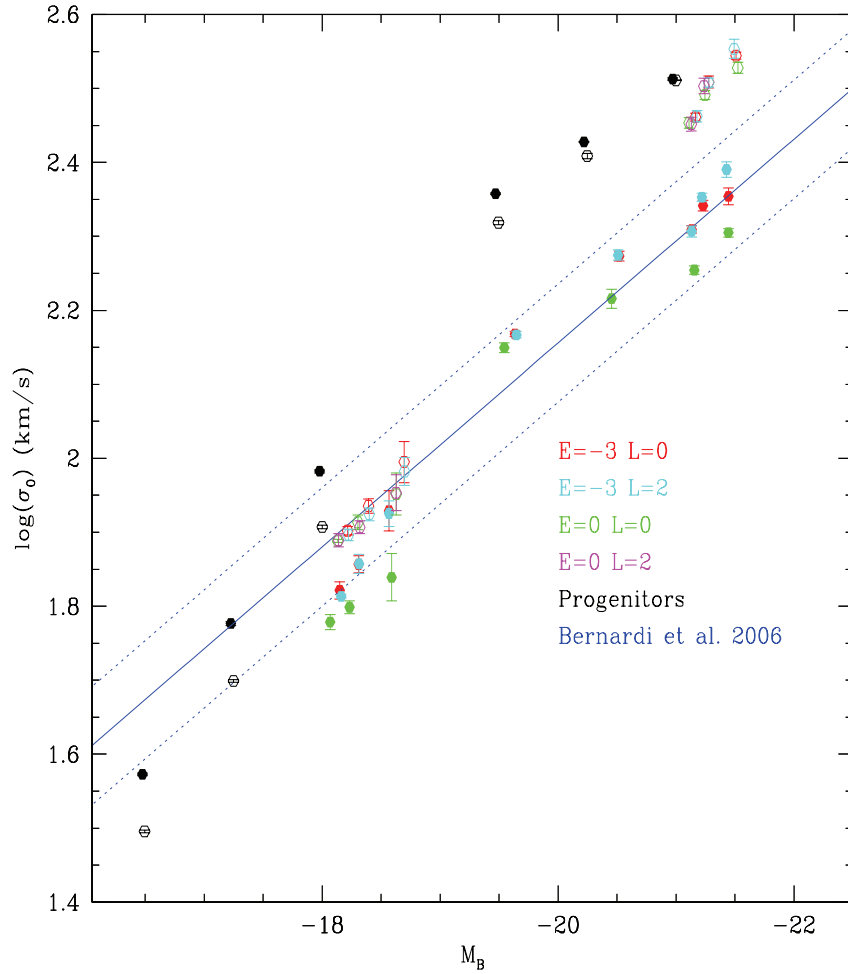


Figure 3.17: $\log\sigma_0 - M_B$ relation of all progenitors and MRs. Open symbols represent one-component progenitors and MRs, while filled points represent two-component progenitors and MRs. In the bottom right corner of the figure we report the meaning of different colors. Solid and dashed blue lines represent the FJ and its scatter from Bernardi et al. (2007).

fitted Sérsic indices are obtained for a constant surface brightness threshold of $27 \text{ mag arcsec}^{-2}$ in the fitting procedure, while in latter plot the fit is performed on the radial range $3 \cdot \epsilon_L < R < 5 \cdot R_{e_L}$ (see Sec. 3.4.1). Symbols are the same as in Fig. 3.11. Solid and dashed blue lines represent the $n - M_B$ relation and its observational 1σ scatter as derived from Trujillo et al. (2004) in the B-band. We find that the absolute magnitude, M_B , always becomes brighter after merging. However this does not necessarily correspond to an increase of n . In particular, MRs resulting from a merger between *ordinary* model galaxies are moved from the merging roughly parallel to the observed $n - M_B$ relation. We do not find the same behaviour for MRs of *bright* model galaxies. However, considering the large scatter of the $n - M_B$ relation, also in this case we can consider the properties of MRs essentially consistent with observations. No difference due to the choice of the fitting radial range neither to the initial conditions of the simulations is found.

3.5 Internal color gradients of ETGs

ETGs do not have uniform stellar populations, with their stars becoming bluer towards the galaxy outskirts. These internal color gradients were known to exist since the pioneering work of de Vaucouleurs (1961), and were interpreted as due to the presence of internal metallicity gradients in ETGs, with stars at the galaxy center being more metal rich and therefore redder than those in the galaxy periphery (Faber 1977). The major evidence for this interpretation came from spectroscopic measurements of absorption line strengths. The Mg_2 and Fe absorption-line strengths of ETGs decrease as a function of the distance to the galaxy center (Burstein et al. 1984; Efstathiou and Gorgas 1985; Thomsen and Baum 1989), hence favoring the interpretation of color gradients as changes in the metallicity content of galaxy stellar populations. Peletier et al. (1990) measured the $U - R$ and $B - R$ color profiles of a sample of 39 ETGs at redshift $z \sim 0$ and found that a pure metallicity gradient is able to explain simultaneously the radial change of both colors inside galaxies. They found the mean ratio of $U - R$ and $B - R$ color gradients to be 2.2 ± 0.5 , with this value being fully consistent with that of 2.1 that is expected in the case of a pure metallicity gradient. However, this result should be taken with some caution, since observational errors on color gradients are large and colors of stellar populations can be redder either a higher metallicity or an older age. This so-called age-metallicity degeneracy was first pointed out by Worthey et al. (1996). The age-metallicity degeneracy makes also difficult to interpret the origin of the color-magnitude (hereafter CM) relation of ETGs, for which brighter galaxies have redder colors (Bower

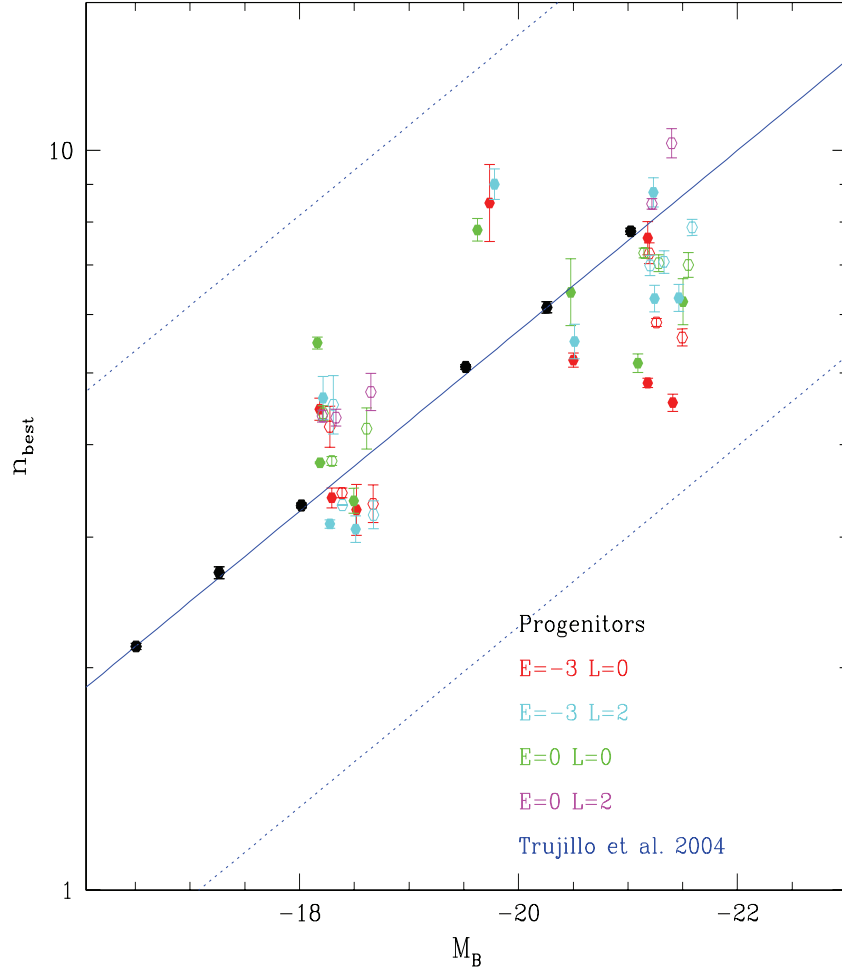


Figure 3.18: The $n_{best} - M_B$ relation as obtained when a constant surface brightness cut is applied in the fit of the surface brightness profile. Open symbols represent one-component progenitors and MRs, while filled points represent two-component progenitors and MRs. In the bottom right corner of the figure we report the meaning of different colors. Solid and dashed blue lines represent the $n - M_B$ relation and its scatter from Trujillo et al. (2004).

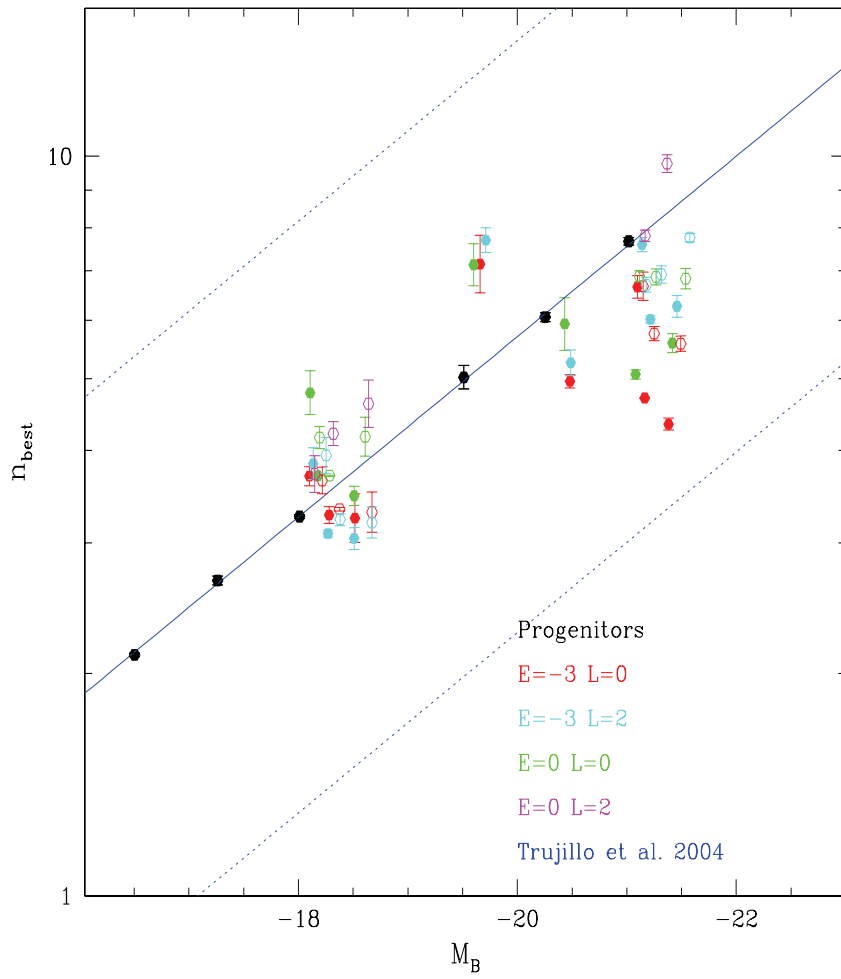


Figure 3.19: The $n_{best} - M_B$ relation as obtained by fitting of the surface brightness profile with $R_{max} = 5 \cdot R_{e_L}$. Colors and symbols are the same as Fig. 3.18.

et al. 1992a,b). As shown by Arimoto and Yoshii (1987) and Kawata (2001), the CM relation can be explained as a pure metallicity sequence, with the average metallicity of stellar populations increasing as a function of galaxy luminosity. This interpretation arises naturally in the framework of the so-called monolithic collapse model of galaxy formation, where the *galactic wind* mechanism would naturally produce a correlation between metal content of galaxies (and hence the color) and their mass (luminosity), but it can also be explained within a hierarchical merging picture of galaxy formation (De Lucia et al. 2006). On the other hand, Worthey et al. (1996) showed that the CM relation at redshift $z \sim 0$ can also be reproduced by a pure age sequence, where bright elliptical galaxies are older and thus redder than the fainter ones, and the metallicity of galaxy stellar populations does not change along the CM sequence. The most effective way of breaking the age-metallicity degeneracy is that of studying the evolution of the CM relation as a function of the look-back time (Kodama and Arimoto 1997). In fact, if the CM relation originates from an age sequence, it should evolve rapidly and should disappear beyond a certain redshift, as faint galaxies approach their formation epoch. On the contrary, if the CM relation is primarily driven from a metallicity change and all ETGs are essentially old, this relation should evolve passively and should be still in place at high redshifts. Following this approach, Kodama and Arimoto (1997) compared the CM relation of ETGs in intermediate redshift clusters (up to $z \sim 0.4$) with the predictions of both age and metallicity models. They found that the CM relation evolves very little with redshift, accordingly to what expected for a pure metallicity sequence. By adopting a similar approach to that of Kodama and Arimoto (1997), Tamura et al. (2000) analyzed the origin of color gradients in ETGs. They described the galaxy in terms of an inner and outer stellar populations, and used a stellar population synthesis code to estimate the difference of color indices (i.e. the color gradient) of these two stellar populations. They produced two models of color gradients, the age and the metallicity models. In the age model, the metallicity of both stellar populations is fixed to the same value, while the age varies from the galaxy center to outskirts. In the second model, metallicity is changed, while age is fixed to be old for both the inner and outer regions. Both models were calibrated to reproduce the color gradient of elliptical galaxies at $z \sim 0$. By evolving back in time both models, Tamura et al. (2000) compared model predictions with color gradients of distant elliptical galaxies (up to redshift $z \sim 1$) from the Hubble Deep Field north (Williams et al. 1996). They found that color gradients agree with those predicted from a pure metallicity gradient model (see Fig. 3.20), while they deviate significantly from predictions of a pure age gradient model even at $z \sim 0.3$ (see Fig. 3.21). The same conclusion was drawn from Saglia et al.

(2000) and Tamura and Ohta (2000), by studying ETGs in distant clusters.

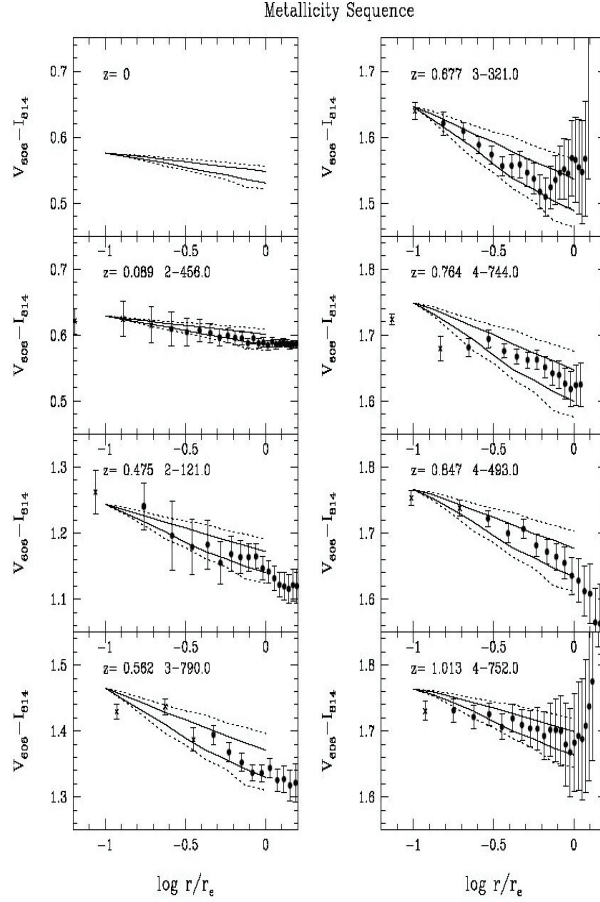


Figure 3.20: Observed color profiles of elliptical galaxies compared to the metallicity gradient model of Tamura et al. (2000). Circles represent the data points. Crosses refer to data points that excluded when deriving the slope of color profiles (i.e. the color gradient). The models show the predicted color gradients seen at each object’s redshift. Solid lines correspond to $\Delta(B - R)/\Delta \log(r/r_e) = -0.09 \pm 0.02 \text{ mag dex}^{-1}$ at $z = 0$ (i.e. 1σ error), and the dotted lines correspond to $\Delta(B - R)/\Delta \log(r/r_e) = -0.09 \pm 0.04 \text{ mag dex}^{-1}$ at $z = 0$ (i.e. 2σ error).

In the hierarchical framework of galaxy formation, ETGs can form through two main channels: (i) galaxy-galaxy merging of disk galaxies, involving gas dissipation, and (ii) dissipation-less merging of spheroidal systems in a given dark matter halo (see Sec. 1.1.2). In general, merging processes are expected to mix the stellar populations inside galaxies, hence washing out stellar population gradients. This has been long advocated as an evidence in favour of the hierarchical merging scenario for the formation of ETGs. In fact, monolithic collapse models predict stellar population gradients which are significantly

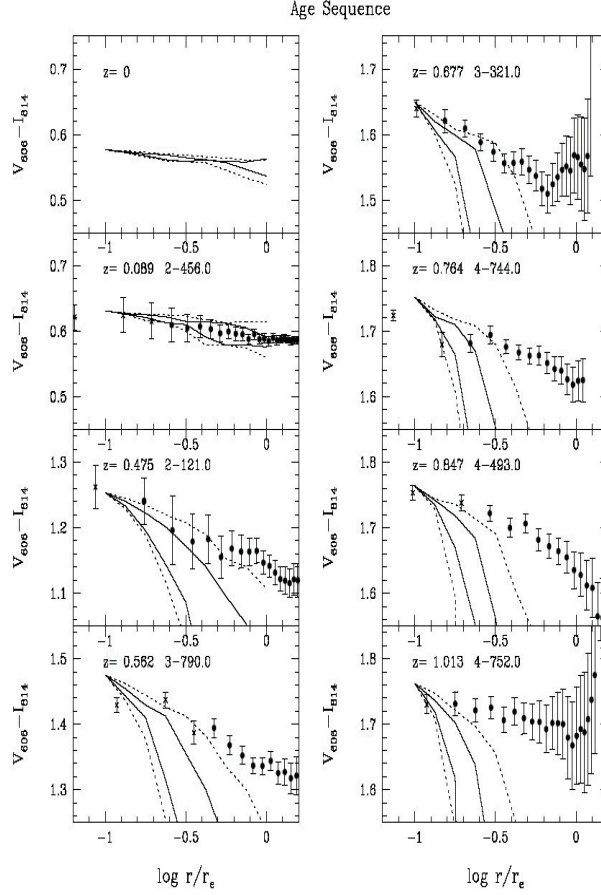


Figure 3.21: Same as Fig. 3.20 from Tamura et al. (2000), but for age gradient model. The plots correspond to different redshift intervals as shown in the upper-left corner of each panel.

steeper than those observed in ETGs (see e.g. Larson 1974a,b; Kawata 2001; La Barbera et al. 2004), implying that some physical mechanism, such as merging, is acting in making the gradients shallower than what expected in a pure collapse picture. Unfortunately, so far, the effect of dissipationless merging on the internal stellar population gradients of ETGs has been poorly investigated. The only work addressing this issue is that of White (1980), who presented a set of dissipation-less merging N-body simulations, analyzing how the merging flattens the initial metallicity gradient of the progenitors. Galaxies were represented by spherical, non-rotating and centrally dense N-body systems with 250 particles. All the merging simulations involved only pairs of equal-mass galaxies, with initial conditions given by either bound or parabolic orbits. The authors found that merger remnants

resemble spheroidal systems, having radially decreasing velocity dispersion and density profiles, well described by a power-law. White (1980) assigned a metallicity to particles in the progenitors according to their initial binding energy. The mean metallicity profile of a model was then derived by averaging particle's metallicities within radial bins (see Fig. 3.22). He concluded that dissipation-less merging is not very effective to mix the stellar population content of galaxies. The metallicity gradient of merger remnants is on average only 13% shallower than that of the progenitors. This finding questions the idea that merging can flatten stellar population gradients in galaxies, thus making troublesome the explanation of the shallow radial gradients observed in ETGs.

One should note that the White (1980) simulations had a very low number of particles, implying a poor spatial and mass resolution. Moreover, they consisted only of stellar matter models and no attempt was done to investigate the effect of unequal mass mergers. Taking advantage of the much better resolution of the one- and two-component models presented in this work (see Chapter 2), and the fact that our models represent more realistically the light and dark matter density profiles of ETGs, we re-analyze in the following sections the effect of dissipation-less merging on the internal population gradients of ETGs.

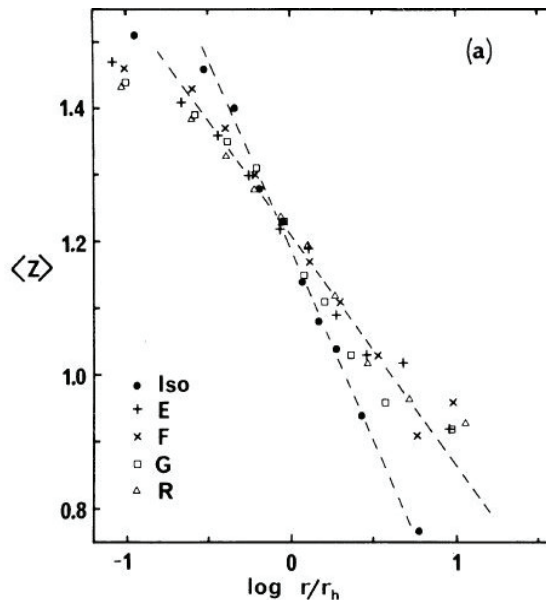


Figure 3.22: Mean metallicity as a function of projected radius for one initial model (Iso) and four merger remnants (E,F,G,R) formed from it by White (1980). The dashed lines are linear fit to *data*. Labels for each N-body system are reported in the lower-left corner of the figure.

3.5.1 Results

We investigate here how the internal metallicity gradient of model galaxies is changed from dissipation-less galaxy-galaxy encounters.

Assigning the metallicity profile

For both the one- and two-component Sérsic progenitors, the metallicity gradient is assigned by associating a given metallicity to each particle. Since there is no objective prescription to perform this association, we verified *a posteriori* that for systems in isolation the radial metallicity distribution of the particles is on average preserved. For each particle, we assign metallicity according to its three dimensional distance, r , to the galaxy center. We impose the constraint that, when projected in two dimensions, the radial metallicity distribution has to reproduce the observed metallicity profile of ETGs. Following La Barbera et al. (2004), this profile can be written as:

$$\log \frac{Z}{Z_{\odot}} = \log \left(\frac{3}{2} \right) + b \log \left(\frac{R}{0.1R_{eL}} \right), \quad (3.6)$$

where the logarithmic slope of the profile is $b \sim \log(0.6) \sim -0.22$. The central metallicity of the profile is $3/2$ of the solar value, Z_{\odot} . The de-projected metallicity profile of the system, $z(r)$, is then obtained by solving the Abell integral equation:

$$z(r)\rho_L(r) = -\frac{1}{\pi} \int_{-\infty}^r \frac{Z(x)I(x)}{\sqrt{x^2 - r^2}} dx \quad (3.7)$$

where $I(R)$ is the projected surface brightness profile of the model, $z(r)\rho_L(r)$ ($Z(R)I(R)$) is the luminosity-weighted deprojected (projected) metallicity profile of the system. For a given Sérsic law, we insert Eq. 3.6 into Eq. 3.7, and then we derive the function $z(r)$ by numerical integration of the Abell equation. For both the one- and two-component progenitors, the function $z(r)$ allows a metallicity value to be directly assigned to each particle.

In order to prove if the above procedure is self-consistent, we let the progenitors to evolve in isolation for $5Gyr$, looking at the time evolution of their initial metallicity profiles. As example, Fig. 3.23 shows the evolution of the projected metallicity profile of the progenitor $ML - 1$ in time steps of $1Gyr$. For each time snapshot, the metallicity profile is derived by taking the luminosity-weighted average of the particle's metallicity in radial bins. To this aim, we first select only particles in the range of $3\epsilon_L$ to $5R_e$. The lower cut ensures that we avoid the inner region of the profile which is blurred out by the smoothing of the gravitational potential. The upper radial cut

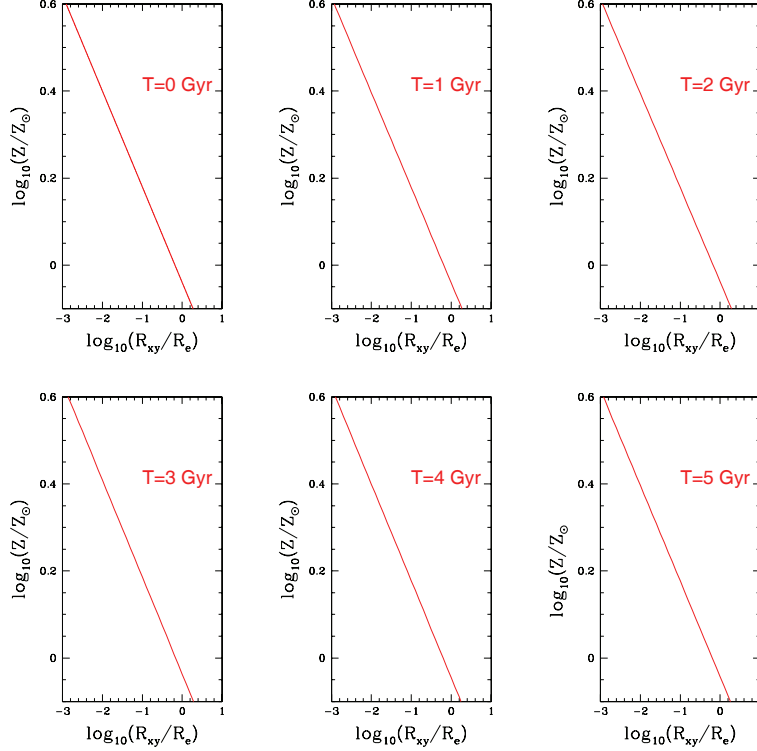


Figure 3.23: Evolution of the projected metallicity profile of the progenitor $ML - 1$ in time steps of 1Gyr .

is applied since the surface brightness profile of ETGs is usually measured within few effective radii (see the discussion above on the choice of R_{max}). We bin the selected particles according to the radial projected distance to the center. The bin size is chosen to be 0.01kpc up to 2kpc , and to 0.1kpc between 2 and 5kpc . We also changed the binning prescription, and we verified that this does not change our results. Finally, for each bin, we take the average metallicity of particles in that bin, by weighting each particle with the corresponding luminosity. All the panels in Fig. 3.23 have the same scale on both axes. We clearly see that the metallicity profile of the system in isolation remains constant as a function of time. The same result was obtained for all the one- and two-component Sérsic models, and for different two-dimensional projections of the progenitors (accordingly to what expected from spherical symmetry).

Metallicity profile of merger remnants

Fig. 3.24 shows the metallicity profiles of merger remnants, for one-component simulations with different orbital energy ($E = 0$ and $E = -3$) and no angular momentum ($L = 0$; see Sec. 3.3). The profiles have been computed by the luminosity-weighted binning procedure described in previous section. Fig. 3.25 shows the same profiles as in Fig. 3.24 but for the one-component merging simulations with angular momentum $L = 2$. Hereafter, we consider only a particular two-dimensional projection of the simulation end-products, though we verified that all the results do not change when considering the different projections. In all plots, the metallicity profile of the progenitors is also shown as a reference (dashed line). We see that metallicity profiles of the merging end-products are always shallower than those of the progenitors. Moreover, one can note that

- the flattening depends on the mass-ratios of the progenitors, with the final profile being flatter in the case of small mass-ratio mergers;
- for a given mass ratio, the flattening also depends on the mass of the most massive (hereafter the first rank) progenitor, with low mass progenitors producing merger remnants with shallower metallicity gradients; this is clearly seen when comparing upper and lower panels in Fig. 3.24 (and Fig. 3.25); lower panels (i.e. low mass progenitors) show on average flatter profiles;
- the orbital conditions also affect the profile of the merging end-products though we do not see any clear systematic trend of the profile slope with either E or L .

These results are summarized in Fig. 3.26, where for each one-component merging pair we plot the relative flattening of the metallicity profile, defined as $\frac{b_f - b}{b}$, where b is the slope of the metallicity profile of the progenitors ($b \sim -0.22$, see Eq. 3.6) and b_f is the slope of the metallicity profile of the corresponding merger remnant. The value of b_f is derived by a linear least-square fit of $\log Z$ as a function of $\log R$. For the most massive progenitors (labels from one to three in Fig. 3.26, the flattening of the profile slope is around 15% of the initial value, with a wide range of values between 5 and 40%. The flattening value of 15% is consistent with that of 13% found by White (1980). Progenitors with lower mass (labels from four to six in Fig. 3.26) have on average larger values of $\frac{b_f - b}{b}$, going from 25% up to 80% in the case of low mass-ratio mergers (label six in the figure). The above trends can be explained by the fact that low mass progenitors have on average lower Sérsic index. A lower n corresponds to a system with a less concentrated

surface brightness profile, which corresponds to have particles on average with a lower binding energy. This makes the radial mixing of particles more effective in the case of low mass progenitors, explaining the above trend of the flattening of the metallicity profile as a function of both the merging mass-ratio and the mass of the first rank progenitor. This is shown in Fig. 3.27, where we plot separately the metallicity profile of both progenitors at the end of the simulation $ML - 3$ (case $E = -3$, $L = 0$). One can note that after merging the profile of particles that were initially in the lower mass progenitor (G2) is flatter than that corresponding to particles of the first rank progenitor, indicating that radial mixing was stronger for the low massive system progenitor. We also verified that when further decreasing the mass of the second rank progenitor, the effect disappears and the merger remnant has a metallicity profile identical to the initial one. This simple test is shown in Fig. 3.28, where we consider the final profile resulting from a merging simulation similar to $ML - 3$ for which we decreased the total mass of the second rank progenitor. The final profile is indistinguishable from the initial one.

Figs. 3.29 and 3.30 are the same as Figs. 3.24 and 3.25 and show the profile of merging end-products of two-component models. The figures show the eight merging pairs as in Tab. 3.3, for simulation with $L = 0$ and $L = 2$, respectively. The results are the same as in the case of one-component models. The merging pairs $ML-1$, $ML-2$, and $ML-3$ ($ML-4$, $ML-5$, and $ML-6$) correspond here to two-component merging pairs $MD-1$, $MD-2$, and $MD-4$ ($MD-6$, $MD-7$, and $MD-8$) in Figs. 3.29 and 3.30. Even for the more realistic two-component models, we find that the flattening of the metallicity profile is larger for lower mass-ratio mergers and for lower mass progenitors. This is further shown in Fig. 3.31, (Fig. 3.26), but plotting two-component (instead of one-component) models. Once again, one sees that the flattening is stronger when decreasing both the merging mass-ratio and the mass of the first rank progenitor.

The analysis was also repeated by changing the initial logarithmic slope of the initial metallicity profiles from $b = -0.2$ to $b = -0.3$, with thus last value being consistent with that measured by Idiart et al. (2003). The results turned out to be the same as for the case with a shallower value of b .

3.6 Conclusion

We performed numerical simulations of one- and two-component galaxy models, exploring the effect of dry mergers on the observed scaling relation and internal color gradients of ETGs. The main results can be summarized

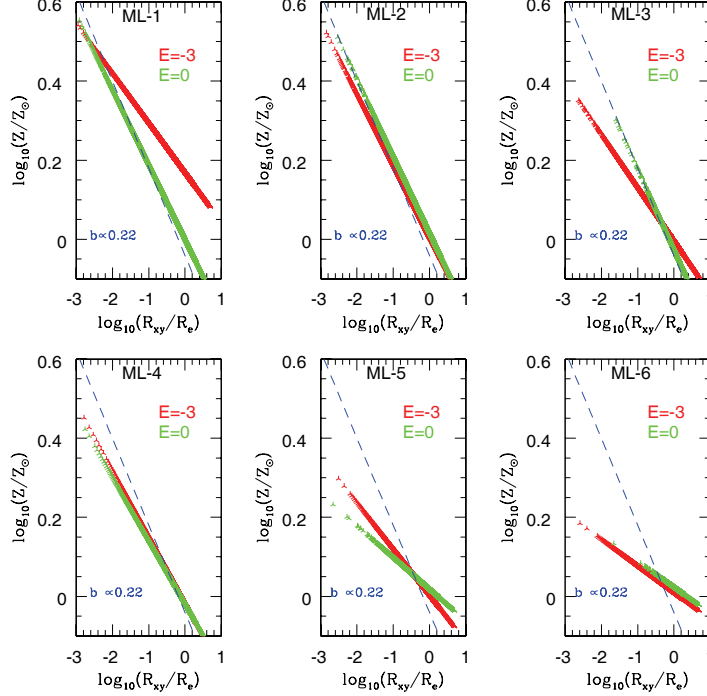


Figure 3.24: Mean metallicity as a function of projected radius for one-component progenitors (blue dashed line) and MRs (red and green points). Green and red colors refer to different values of E as reported in the upper right corner of each panel. The plots refer to the case $L = 0$. Only model pairs leading to merged systems are shown (see Sec. 3.1.1).

as follows.

- Remarkably, and in agreement with previous studies, all the merger remnants (MRs) for both one and two-component simulations and independently of the density profile and the initial orbital parameters are found to lie on the FP relation within the observed scatter. MRs follow a FP relation roughly parallel to that of the progenitors.
- After one merging generation, luminous galaxy models are moved along the observed KR. We also find that one merging generation is not able to move low-mass galaxy models far away for the observed locus of galaxies in the $M_B - \langle \mu \rangle_e$ plane. The result is the same for both one- and two-component models, and does not depend on the initial merging conditions (values of E and L). These findings are in agreement with a scenario whereby faint galaxies underwent on average non more than one single dissipationless encounter in the past, while bright galaxies

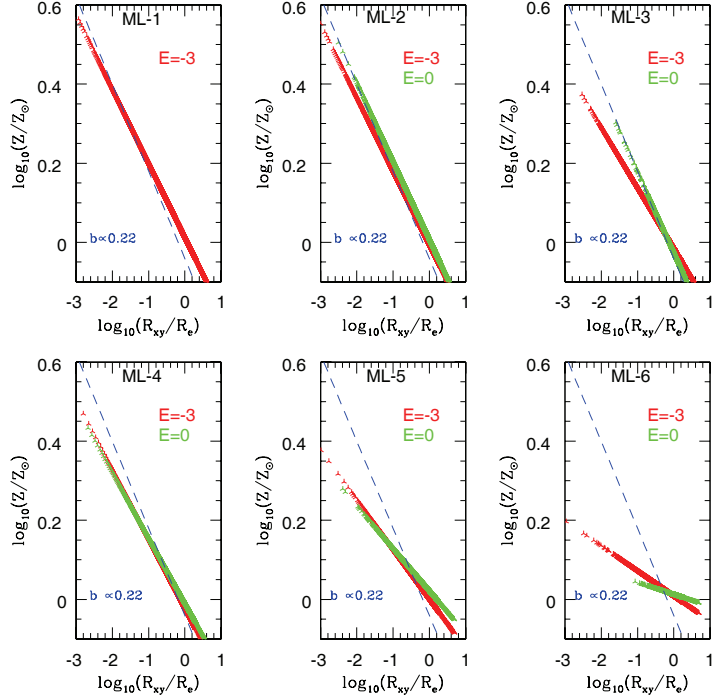


Figure 3.25: Same as Fig. 3.24 but for $L = 2$.

form through several dry mergers, as shown by semi-analytical models of galaxy formation (De Lucia et al. 2006).

- Although we see a mismatch between the FJ relation of MRs and progenitors (see discussion in Sec. 3.4.3) remarkably we find all the two-component merged models follow the observed relation. Also in this case the initial conditions of the simulations do not affect significantly the properties of MRs.
- For luminosity-Sérsic index relation, the properties of MRs are fully consistent with observations, taking into account the large scatter of the $n - M_B$ relation. No difference due to initial orbital parameters is found.
- Metallicity profiles of our MRs are always shallower than those of the progenitors. The flattening depends on the mass-ratios of the progenitors and on the mass of the most massive progenitor, in the sense that final metallicity profiles are flatter in the case of small mass-ratio mergers and for a lower mass of the first rank progenitor. The final profiles

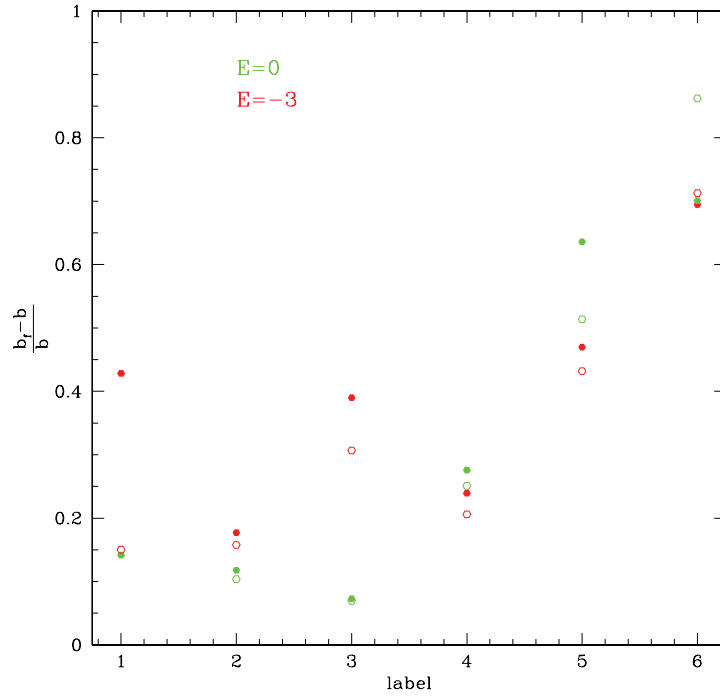


Figure 3.26: Relative flattening of the metallicity profile in one-component simulations. Different colors refer to different values of the initial orbital parameter E as reported in the upper-left corner of the figure. Filled symbols refer to cases with $L = 0$, while open symbols represent cases with $L = 2$.

of MRs also depend on the initial orbital parameters. In contrast to previous studies (White 1980), findings reconcile the hierarchical formation scenario of ETGs with observational results, allowing the shallow metallicity gradients of ETGs result of dissipationless galaxy merging.

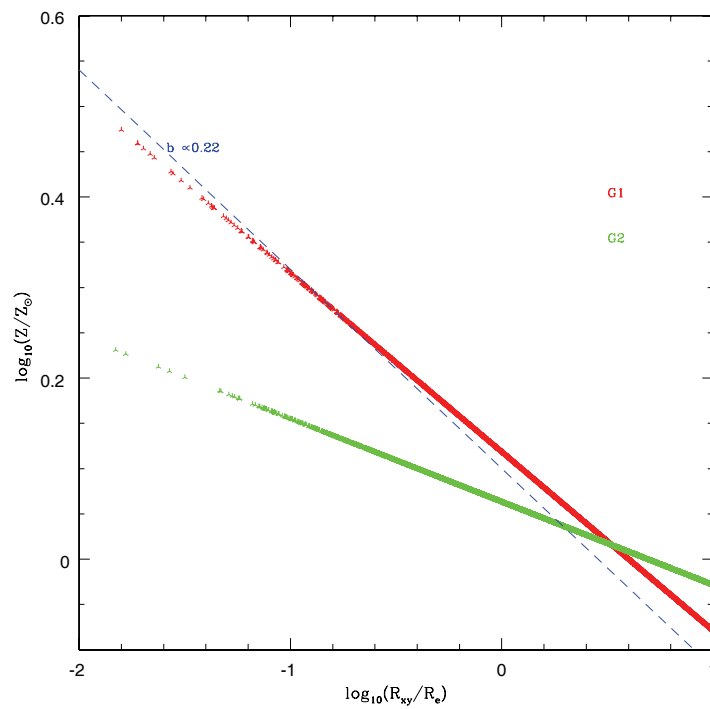


Figure 3.27: Mean metallicity as a function of projected radius for the model $ML - 3$. Red line represents the gradient for particles belonged to the most massive progenitor, while green points belonged to low-massive progenitor.

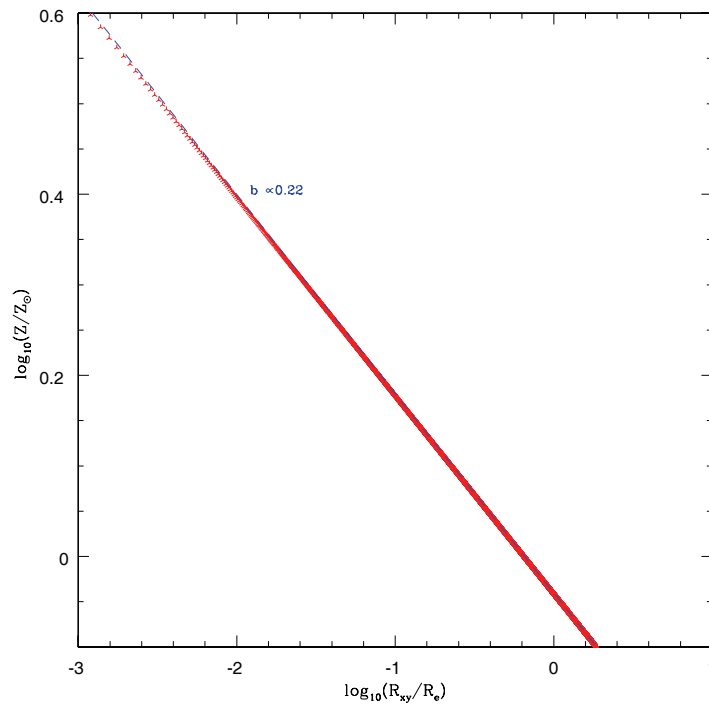


Figure 3.28: Final metallicity profile resulting from a merging simulation identical to *ML* – 3 (see Tab. 3.2) except than for a lower total mass of the second rank progenitor (see text for details).

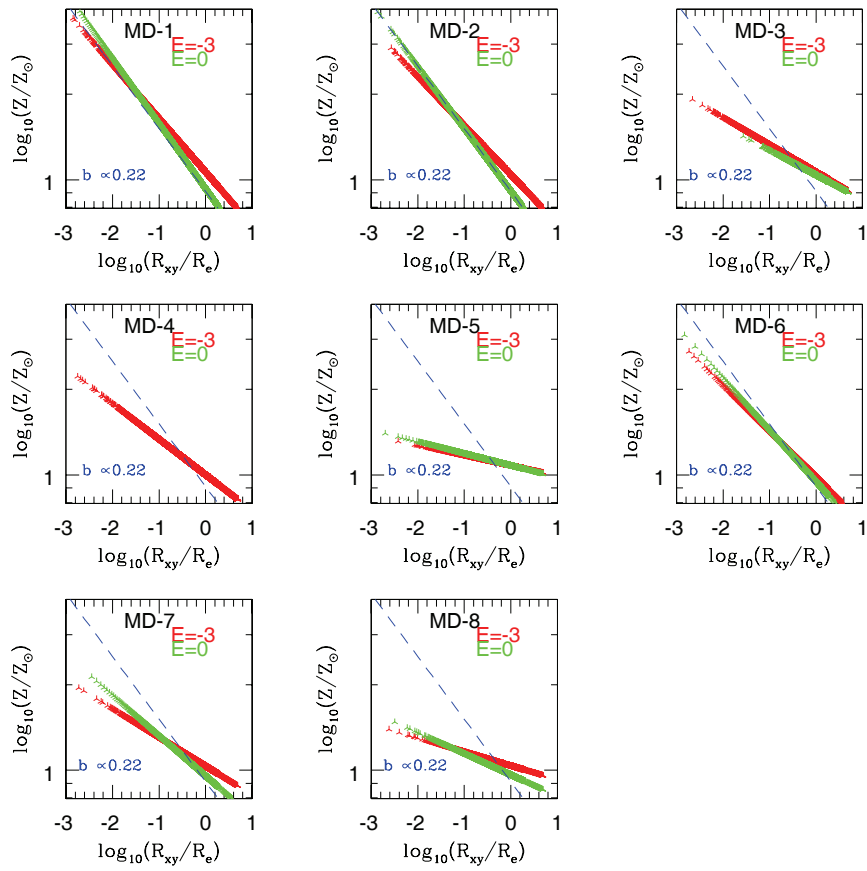


Figure 3.29: Same as Fig. 3.24 for two component simulations.

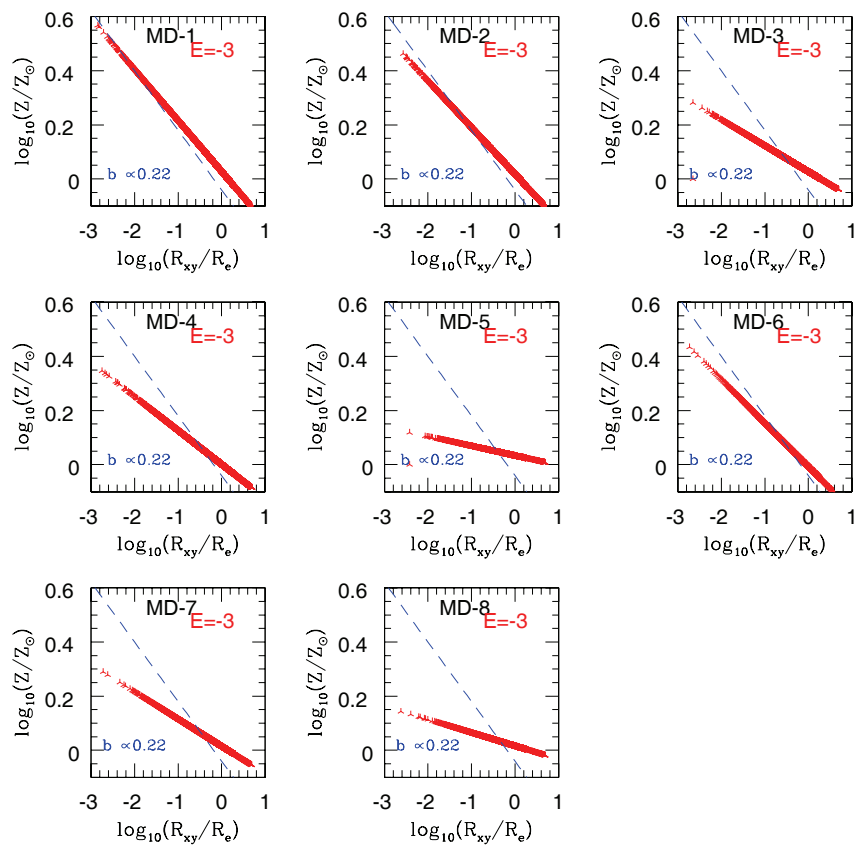


Figure 3.30: Same as Fig. 3.25 for two-component simulations.

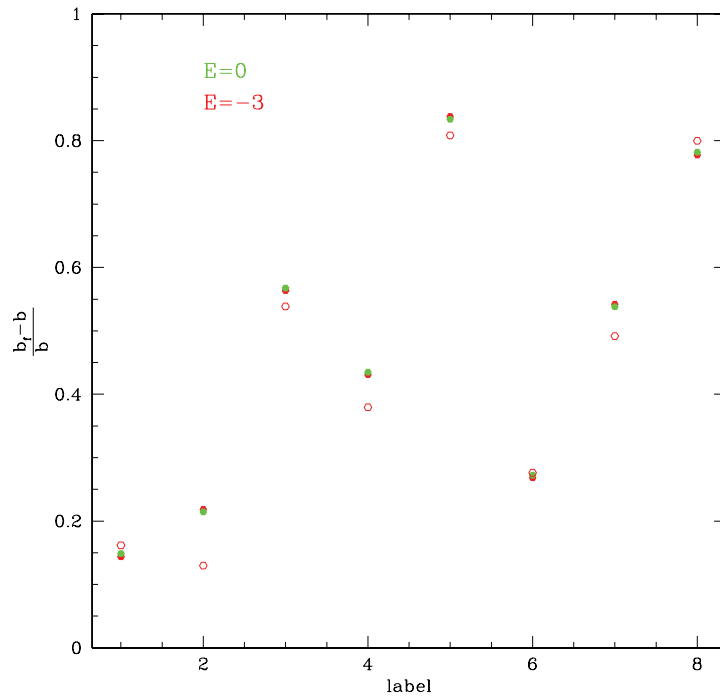


Figure 3.31: Same as Fig. 3.26 for two-component simulations.

Chapter 4

Disk dominated galaxies from major mergers: the role of the gaseous halo

We use hydrodynamical simulations to examine the structure of merger remnants resulting from major merger between systems that are gas dominated. We show that, in this case, a prominent disk survive. We analyze an extreme example with progenitor galaxies consisting of a dark matter halos, a gas halos, a pure gas disks and a small stellar bulges. The outline of this chapter is as follows. In Sec. 4.1 and 4.1.1 we discuss different scenario proposed in literature to rebuilding disk systems starting from a merger of late-type galaxies. Models of galaxies used as initial conditions are presented in Sec. 4.2, while in Sec. 4.3 and Sec. 4.4 we show and discuss the results of the merging simulation.

4.1 Introduction

As show in Chapter 1, Toomre (1977) was among the first to recognize that mergers can drive the evolution of galaxy types by changing disk into objects that resemble ellipticals. This idea was examined numerically by Barnes (1988, 1992) and Hernquist and Spergel (1992); Hernquist (1993a) in the limit where dissipative effect arising from gas dynamics are negligible; in these works they showed that mergers involving equal-mass galaxies do yield remnants with properties similar to those of observed ellipticals. Models of galaxy collisions including dissipation (Barnes and Hernquist 1996) showed that gas can loose angular momentum owing to gravitational torques and shock during merger events. In cases when the interstellar medium (ISM) is

isothermal and relatively cold and the gas fraction of the galaxies is small, the subsequent inflow of gas into the centers of the merger remnants forms a roughly spherical stellar distribution through a luminous starburst, leaving objects that have essentially no extended stellar disks.

While major mergers are the most striking examples of galaxy collisions, *minor* mergers between galaxies of different masses are probably more frequent. Simulations have shown that dissipationless minor mergers between spiral galaxies and smaller companions can cause significant perturbations to disks through dynamical heating (e.g., Velazquez and White 1999). This conclusion is unaffected by dissipation when the disks contain a small fraction of their mass in gas (Hernquist and Katz 1989).

All these studies were based on theoretical models in which the interstellar gas was at most a small fraction of the disk mass ($f_{gas} \leq 0.1$ in the progenitor disks) most of which was rapidly consumed in star formation. In pioneering work, Springel and Hernquist (2005) and Robertson et al. (2006) showed that, in merger simulations with a significant stellar feedback to allow the stable evolution of extremely gas rich disk ($f_{gas} \sim 1$) even a major merger can produce a disk-dominated remnant. Together with other recent investigations (Hopkins et al. 2008b), these works have led to growing consensus that a combination of strong stellar feedback and large gas content is essential to the survival of disk galaxies.

However, these previous works only considered the gas inside the disks of the galaxies and neglected the effect of gas accretion from the halo of the galaxies. Very recently, new cosmological simulations (Governato et al. 2008) have shown that the presence of fresh infalling gas during and after a major merger can produce an early-type spiral galaxy even though the initial gas fraction in the disk is moderate (10 – 20 %). The resulting galaxy exhibits the largest disk ever formed in a cosmological simulation. Hence the following question arises: are perhaps gas-rich mergers a new channel to form late-type spiral galaxies with an extended disk component, such as low surface brightness (LSB) galaxies? Due to its complexity, a cosmological simulation does not allow to clearly identify the role of gas accretion in preserving and/or re-building an extended disk. In addition, the tendency towards producing galaxies with excessive central mass concentration due to limited resolution (Mayer et al. 2008) does not render them a good tool to address this question. In this work we perform new high resolution simulations of disk mergers that contain for the first time an extended gas component in the halo in addition to the gas in the disk, thus miming the conditions found in cosmological simulations of Governato et al. (2008). Rather than using equilibrium models, we use galaxy realizations produced by more realistic collapse experiments in CDM halos (Kaufmann et al. 2006, 2007). We demonstrate that disks

not only survive the merger but can grow to a much larger size as new gas cools from the halo, thereby producing a galaxy that is much more disk-dominated than the progenitors. The final galaxy has properties resembling those of late-type LSB galaxies, with a tiny bulge component. Thus we suggest this scenario as solution of the problem of LSB formation in cosmological simulation. When cosmological simulations will be able to produce objects resembling our initial conditions, the LSB galaxies will naturally form by merging of these systems.

4.1.1 Cold and hot accretion

According to the conventional sketch of galaxy formation described in Chapter 1, gas falling into a dark matter potential well is shock heated to approximately the halo virial temperature, $T_{vir} = 10^6 (v_c/167 \text{ km s}^{-1})^2 \text{ K}$, putting it in quasi-hydrostatic equilibrium with the dark matter. Gas in the dense, inner regions of this shock-heated halo radiates its thermal energy, loses its pressure support, settles into a centrifugally supported disk, and forms stars (White and Rees 1978; Blumenthal et al. 1984). Over the last decade, the ideas of these seminal papers have been updated and extended into a powerful semi-analytic frame-work for galaxy formation calculations (White and Frenk 1991; Kauffmann et al. 1993; Mo et al. 1998; Somerville and Primack 1999). N-body and hydrodynamic simulations showed that a substantial fraction of the gas in these simulations does shock heat to $T \sim T_{vir}$, and some part of this gas does cool and settle into galaxies. There is, in fact, a long history of results suggesting that cold accretion could be an important element of galaxy formation. Binney (1977), using analytic models of protogalaxy collapse, argued that the amount of shock heating could be small for plausible physical conditions, with only a fraction of the gas reaching temperatures $T \sim T_{vir}$. Other examples are given by the first SPH simulations of forming galaxies (Katz and Gunn 1991), where most of the gas never heated above $T \sim 3 \times 10^4 \text{ K}$. However, several studies based on SPH simulations of cosmological volumes reveal the situation even more starkly. For example, Fardal et al. (2001) showed that most of the cooling radiation in their simulations comes from gas with $T < 2 \times 10^4 \text{ K}$ and in a recent work, using SPH simulations, Kereš et al. (2005) demonstrated that roughly half of the gas accreted by the simulated galaxies is never shock heated close to the halo virial temperature ($T \sim 10^6 \text{ K}$) but instead radiates its acquired gravitational energy from $T \lesssim 2.5 \times 10^5 \text{ K}$. The importance of this *cold accretion mode*, relative to the *hot accretion mode* envisioned in the traditional picture of galaxy formation, depends strongly on galaxy mass. Most galaxies below a baryonic mass $M_{gal} \sim 10^{10} M_\odot$ or dark halo mass

$M_D \sim 10^{11} M_\odot$ accrete primarily in cold mode, while more massive galaxies accrete primarily in hot mode. Since high mass galaxies are built from lower mass systems, even galaxies at the top end of the luminosity function today acquired a significant fraction of their mass via cold accretion. Globally, the increasing mass scale of galaxies means that cold accretion dominates at high redshift and hot accretion at low redshift. The ratio of cold to hot accretion is also environment dependent, mostly because higher mass galaxies are more common in dense environments, and partly because low mass systems in dense environments have a larger hot accretion fraction than their isolated counterparts.

4.2 Simulations and initial conditions

We have performed a suite of 4 major mergers simulations (1 : 3) of late-type systems with a large gas fraction in the halo ($f_{gh} \gg 0.5$) and an extended gas disk ($R_d \sim 19 kpc$). In each merger all progenitors are constructed starting from the model called M33B in Kaufmann et al. (2007). In this paper M33B is built to produce a low-mass spiral galaxy such M33. We underline that M33B is not a pre-defined equilibrium model, but in Kaufmann et al. (2007), the authors followed the gas cooling inside the dark halo producing a more realistic collapse experiment. We also note that our models are not peculiar because, for example in COSMOS, about 50% of found disk galaxies have very small bulge since $z = 1$ (Sargent et al. 2007).

At equilibrium the model consists of a low-massive dark halo, an hot gas halo out the virial radius, an extended gas disk and a small stellar bulge. The dark matter halo follows a NFW profile, while the gas disk attains a near exponential surface density profile over a large fraction of its extent (19 kpc), instead within a few hundred pc from the centre, a dense nucleus produces a central spike in the profile. The temperature of gas particles in the halo is $T \approx 2 \times 10^5 K$, while the mean density of this component is $\rho \approx 10^{-4} atm/cm^3$. The introduction of an hot gas halo in the progenitor models is the more important innovation respect to the previous paper that addressed this problem.

In order to simulate major merger events of M33-like systems, we performed a suite of 3 hydrodynamical simulations. Our merging models are named $M1$, $M2$, $M3$, respectively. In the $M1$ model, the progenitors are M33B and M33B3, this last progenitor has the same properties of M33B, but mass 1/3 of that. The $M1$ model is run without star formation prescription, for this reason we adopt a temperature floor $T_f = 30000 K$ that crudely mimic the effect of heating sources such as supernova explotions and radiation back-

grounds. In the $M2$ model we use the same progenitors as in $M1$, but without halo gas particles. In order to investigate the influence of the gas fraction on the disk survival, in the $M3$ model we merge M33B and M33B3 with star formation prescription. For this model, before to merge, progenitors are also evolved in isolation for 2 Gyr with star formation prescription. We use a parabolic orbit and a relative disk orientation of $\theta = 45$ for all models. Each progenitor contains $N_{gas} = 99983$ gas, $N_{star} = 2376$ stellar and $N_{DM} = 250000$ dark matter particles. The 85% of gas particles are hot ($T \sim 2 \times 10^5\text{ K}$) and they are in the halo (except for $M2$ model). In Tab. 4.1 we summarize all parameters of the most massive progenitor for each merging model, including the gas fraction.

The simulations were run with the parallel SPH+N-Body code GASOLINE, which is described in the Sec. 1.4.3.

Model	M_{1DM} (M_{\odot})	M_{1*} (M_{\odot})	M_{1g} (M_{\odot})	f_{gh}	r_{peri} (kpc)	r_{init} (kpc)	θ (deg)
$M1$	$2.23 \cdot 10^{11}$	$7.22 \cdot 10^7$	$1.41 \cdot 10^{10}$	85%	19	91	0
$M2$	$2.23 \cdot 10^{11}$	$7.22 \cdot 10^7$	$6.97 \cdot 10^{10}$	0%	19	91	0
$M3$	$2.23 \cdot 10^{11}$	$6.41 \cdot 10^8$	$2.52 \cdot 10^9$	55%	19	91	0

Table 4.1: *Col. 1:* merger model label. *Col. 2:* dark matter halo mass of the most massive progenitor, M_{1DM} , in units of M_{\odot} . *Col. 3:* stellar mass of the most massive progenitor, M_{1*} , in units of M_{\odot} . *Col. 4:* gas mass of the most massive progenitor, M_{1g} , in units of M_{\odot} . *Col. 5:* fraction of gas particles in the halo, f_{gh} . *Col. 6:* pericentric distance between two progenitors, r_{peri} , in units of kpc . *Col. 7:* initial distance between the progenitors, r_{init} , in units of kpc . *Col. 8:* relative progenitor disk orientation, θ

4.3 Results

We want to investigate if after merger events, the final systems exhibit a centrifugally supported object. To this aim we determine the structural and kinematic properties of the end-products starting from the set of positions and velocities in each simulation output file produced by GASOLINE.

First we analyze the gaseous v/σ ratio profile of all merger remnants. The velocity- and velocity dispersion profiles applying the TIPSYPY task/profile (www-hpcc.astro.washington.edu/tools/tools.html) on our final snapshots. In the upper panels of Fig. 4.1 we show our results. The gaseous v/σ ratio profile after 5 Gyr s starting the merger, is plotted by using red points for our final systems, while blue points represent the v/σ ratio profile for gas in

the disk of the most massive progenitors before to start the simulation. We note that for the merger remnants of $M1$ and $M3$ models the total gaseous rotational support exceeds $v/\sigma = 1$, for a wide range in radius and that in each of these merger remnants the size of the new gas disk exceeds the size of the gas disks in the progenitors. For the remnant of the $M2$ model we find that, although the v/σ exceeds 1, the profile is very noisy and the values of the v/σ ratio at fixed r are rather than those inferred for the other models. The maximum radius corresponding to $v/\sigma > 1$ for gas and stellar in the final disk are reported in Tab. 4.2 (col. 2 and 3). Hereafter we refer to this parameters as limit radius and we indicate them with R_{l_g} and R_{l_*} , respectively.

The mass of the gaseous and stellar structures in the remnant can be measured from the surface mass density profile. This quantity is obtained as function of the distance from the center of the system (given by the center-of-mass), by using the TIPSy task/profile. Fig. 4.2 (middle and bottom panels) shows our results analyzing the gas and stellar surface mass density profile respectively, as seen when looking onto the orbital plane. In the middle panels red points represent the gas in the end-products for all merger remnants as in the upper panels, while blue points are the gas in the disk of the most massive progenitors. In the bottom panel, green points represent the stars in the end-products for the final systems as in the upper panels. Each surface mass density profile in the final object is modeled by a single or a multi-component systems as a function of radius r which may include a single exponential disk:

$$\Sigma(r) = \Sigma_d e^{-r/R_d} \quad (4.1)$$

or a sum of this with a stellar spheroid given by a de Vaucouleurs (1948) profile:

$$\Sigma(r) = \Sigma_b 10^{-3.331[(r/R_b)^{1/4}-1]}. \quad (4.2)$$

In this second case the first component describes an exponential gas/stellar disk, while the second represents a very small central gas/stellar bulge formed by the starburst and by the old disks destroyed during the collision.

In Fig. 4.2 (middle and bottom panels), we overplot the best fitted surface mass density profile. For gas in $M1$ model we are able to fit the measured profile by using the sum of the exponential law plus the de Vaucouleurs law. In the $M2$ model, both gas and stars are described by using a simple de Vaucouleurs profile. Finally, in the $M3$ model gas is described by using a exponential profile, while stars can be fitted by the sum of the two considered law. All best fitted parameters are reported in Tab. 4.2. We note that for

Model	R_{lg} (kpc)	R_{l*} (kpc)	R_{dg} (kpc)	R_{bg} (kpc)	R_{d*} (kpc)	R_{b*} (kpc)	n_g	n_*	B/D	μ_{0B} (mag/arcsec ²)
<i>M1</i>	75	—	27.4	18.4	—	—	1.4	4	0.007	28.6
<i>M2</i>	—	—	—	13.2	—	20.8	3.5	4.6	1.4	22.2
<i>M3</i>	55	20	8.4	—	6.8	6.29	2.9	2.7	0.7	27.9

Table 4.2: *Col. 1*: merger model label; *Col. 2 – 3*: the limit radius for the gaseous and stellar disk (see text for definition) in units of *kpc*; *Col. 4 – 7*: the scale length from the fit bulge+disk for gas in the disk, R_{dg} , and bulge, R_{bg} , and for stars in the disk, R_{d*} , and bulge R_{b*} , respectively; *Col. 8 – 9*: the Sérsic index for the gas, n_g and stellar, n_* , component as obtained from a fit of the mass profile with a Sérsic law; *Col. 10 – 11*: the bulge to disk ratio and the central surface brightness in units of *mag arcsec*⁻² in B band for all merger remnants.

the stellar components it was always necessary to use the parametrization bulge + disk and that the inclusion of the feedback mechanism reduces the mass density of the gas disk because a lot of part of this component is used to form new stars.

For each models we also use a Sérsic law to fit the mass distribution in the merger remnants and we report in Tab. 4.2 the Sérsic index parameter.

4.4 Discussion and conclusion

Major mergers of disk galaxies play a prominent role in hierarchical models of galaxy formation. They are thought to be a primary path for the formation of large elliptical galaxies and to give rise to powerful starbursts events. Typically, semi-analytical models of galaxy formation make the simplifying assumption that the gas present in a major merger is completely consumed in a powerful burst, such that a spheroidal remnant without a disk component is formed. However, recently Springel and Hernquist (2005); Robertson et al. (2006); Hopkins et al. (2008b) show that gas-dominated mergers where the interacting systems have high gas fraction, allow the formation of rotationally supported disks in remnants if energetic feedback mechanisms limits the conversion of gas into stars. This stabilizes gas disks and allows mergers to produce large, smoothly distributed, rapidly rotating stellar disks.

The simulations we analyzed here provide evidence in favour of a new important ingredient for the formation of disk galaxies in the hierarchical scenario: disk can also form from disk-disk merging. The main novelty is that galaxy models have a gaseous halo in addition to gas in the disk, as expected from cosmological simulations (Governato et al. 2008). We perform a suite of 3 merger simulations to address the feasibility of such a scenario and we demonstrate that mergers between our progenitors having gas as the

dominant baryonic component, as typical in low mass galaxies, produce late-type galaxies rather than elliptical/S0 galaxies as a result of the mergers. We demonstrate that old stars violently relax into a hot spheroidal component, thus contributing to the bulge, as repeatedly demonstrated in the past (Barnes and Hernquist 1996; Hopkins et al. 2008b). Despite the high gas mass fraction in the disks the large disk is mostly built by the fresh infalling gas cooling from the halo that settles in a centrifugally supported disk structure after the merger. The gas cooling from the halo has a crucial role in producing a disk-dominated remnant, an effect that was never introduced previously. This is demonstrated in a test $M2$, where the gaseous halo was removed. In this case we find a galaxy with a much larger final bulge-to-disk ratio.

Gas particles in the halo have a temperature very close to the peak of the cooling function thus they cool very rapidly ($t_{cool} \sim 1.3 Gyr$). This gas settles in orbits with high angular momentum and is responsible for building a very extended outer disk in the merger remnant. According to Sec. 4.1.1, since our progenitors are low-mass systems, gas in the halo should accrete primarily in cold mode.

Final disk can extend out to $40 kpc$ and has a scale length ~ 2 times the initial one. New stars, forming in such a disk in the runs including SF, also have a scale length ~ 2 times that of the initial baryonic disk (in the $M1$ model the initial baryonic disk is entirely gaseous).

In order to understand if our scenario is able to reproduce LSB galaxies, we calculated (see the last column of Tab. 4.2) the central surface brightness of our merger remnants. Our values are similar to those inferred for observed LSB galaxies from de Blok and McGaugh (1997). These authors in fact put the threshold at $\mu_B = 23.2 mag arcsec^{-2}$ to distinguish between normal spiral and LSB galaxies. Very large scalelengths inferred from our models are very similar to the values obtained by Zwaan et al. (1995). Since LSB galaxies obey the same Tully-Fisher relation as normal spiral galaxies (Zwaan et al. 1995), these high values at fixed V_{max} , are necessary in order to reach the required value of L . Moreover, it is encouraging to note that our models can reproduce the observed high gas fraction for LSB galaxies, in fact de Blok and McGaugh (1997) derived for these systems in their sample $M_g/M_* > 10$. In the future work we will explore different initial conditions (progenitors mass, gas fraction and orbit) in order to explore in we are here in a favorable case, since the temperature of the particles in the halo favours rapidly cooling and the following disk formation.

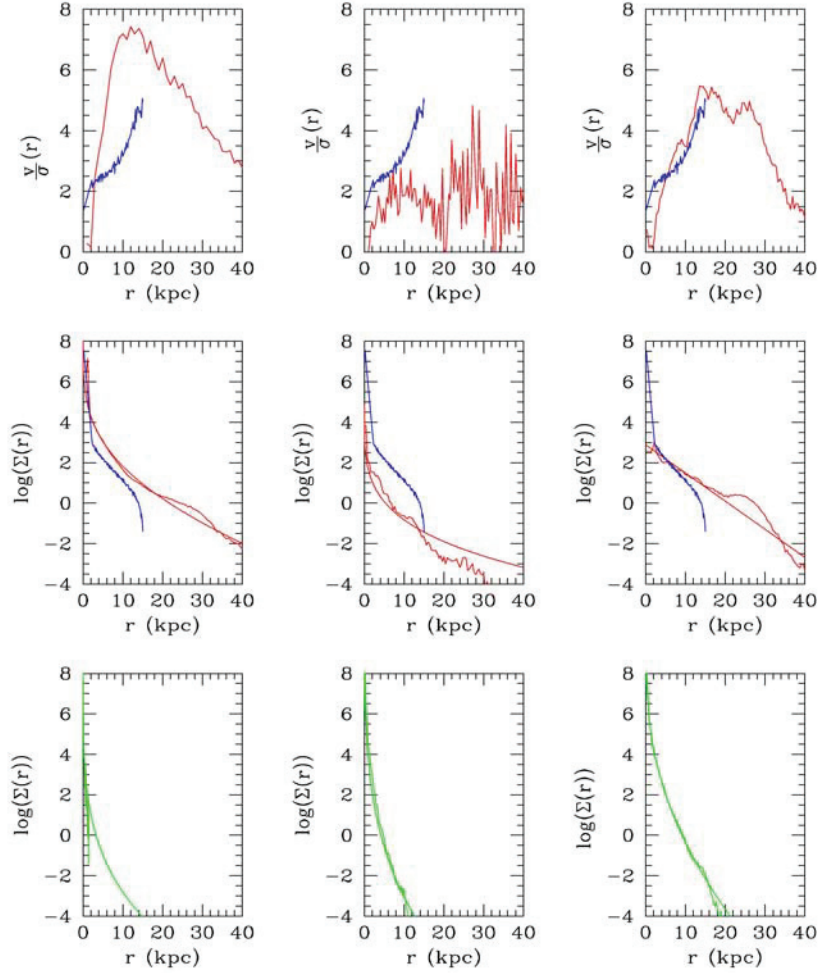


Figure 4.1: *Upper panels:* the gaseous v/σ ratio profile for merger remnants of $M1$, $M2$ and $M3$ models. Red points represent the gas after $5Gyrs$ in merger remnants, while blue points represent the gas in the disk of the most massive progenitors. *Middle panels:* surface mass density profiles for the gas in the remnants of models $M1$, $M2$ and $M3$. Red points represent the gas in merger remnants after $5Gyrs$, while blue points represent the gas in the disk of the most massive progenitors. We also over-plot the best fitted profile obtaining fitting the gaseous surface mass density profile of the merger remnants. *Bottom panels:* surface mass density profiles for the stellar components in the remnants $M1$, $M2$ and $M3$. We also over-plot the best fitted profile obtaining fitting the stellar surface mass density profile of the merger remnants.

Chapter 5

Formation and evolution of $S0$'s galaxies

The formation of $S0$ galaxies is still not well understood. In order to understand the observational features and the physical mechanisms that drive the formation of these systems in clusters, we selected from an high resolution cosmological simulation a galaxy cluster with the size of Virgo cluster and we developed an original scheme to identify elliptical, $S0$ and spiral galaxies candidates based on the merging history of substructures in simulated cluster. The scheme identifies subhaloes inside the simulated cluster at different times and traces their merging history. We think that this scheme may be used to put constraints on the $S0$ formation mechanism.

5.1 Introduction

Understanding the origin of the Hubble sequence remains a fundamental goal in extragalactic astronomy. The lasting utility of Hubble classification scheme lies in its ability to distinguish between both the dynamics and stellar populations of disk and spheroidal galaxies ($S0$ s). However, despite considerable progress in unraveling the time evolution of elliptical (E) and spiral (S) galaxies, there is still some disagreement concerning the origin of $S0$ s - a hybrid class with kinematic characteristics of disk galaxies but whose present-day stellar populations resemble those seen in Es. $S0$ s provide a useful exemplar of what could be an intermediate stage of a galaxy evolution. They also give us insight into galaxy formation and its relationship with environment. Hubble Space Telescope observations of distant galaxy clusters show that the fraction of $S0$ s, f_{S0} , declines when one looks back from the current epoch to an epoch $\sim 5 Gyr$ ago (Dressler et al. 1997; Smith

et al. 2005). The results presented by Treu et al. (2003) and Smith et al. (2005) are perhaps the most enlightening: they find a smaller increase in the bulge-dominated galaxy (E+S0) fraction (f_{E+S0}) with increasing density at $z \gtrsim 0.4$ than is seen at $z < 0.1$ but also find comparable f_{E+S0} values for low density regions ($\Sigma < 10 \text{ galaxies Mpc}^{-2}$) at $z \gtrsim 0.4$ and the current epoch. Smith et al. (2005) propose a simple model to explain these observations in which high-density regions at $z \sim 1$ would largely be comprised of Es with only a trace of S0s (e.g., $0 \leq f_{S0} \leq 0.1$). They consider various processes to transform S galaxies into S0s in order to increase f_{S0} with time to match the observed morphological population fractions at $z \sim 0.5$. The idea that star formation in S galaxies is cut off when they enter a denser environment therefore seems a plausible one. The mechanism by which this cessation is achieved is a topic of active debate and many scenarios have been proposed. These include close encounters or mergers, which increase the luminosity of the bulge component by heating the central parts of the disk or triggering a central star formation episode (Mihos and Hernquist 1994; Bekki 1998). Galaxy harassment (Moore et al. 1999) is predicted to have a similar effect. Other scenarios involve the interaction of a S galaxy with the intra-cluster gas by ram pressure stripping (Gunn and Gott 1972; Quilis et al. 2000; Vollmer et al. 2001) or over a longer period, by removal of gas from the galaxy halo (Larson et al. 1980), or by heating of gas within the galaxy by the intra-cluster medium (ICM) (thermal evaporation) (Cowie and Songaila 1977). These transformation scenarios can be separated in a number of ways, perhaps contrasting the effects of other galaxies against intra-cluster gas, or looking at gravitational versus hydrodynamical drivers. However, detailed studies of local S0s have failed to resolve the question of whether they are faded remnants of early spirals (Poggianti et al. 2001; Burstein et al. 2005), or if they instead have similar formation histories to ellipticals, but with different bulge-to-disk ratios. The most direct approach to resolving this debate would be to track directly the evolution in the S0 and elliptical fractions with lookback time, thus tracing the formation histories of the two classes independently. Considerable progress has been made in tracking the evolving fraction of spheroidals, f_{E+S0} , as a function of environmental density Σ (Smith et al. 2005; Postman et al. 2005; Capak et al. 2007). One suggestion is that only ellipticals were present in abundance at $z \simeq 1$ ($f_{S0} < 0.1$), with subsequent growth in f_{E+S0} arising primarily via a density-dependent transformation of S galaxies into S0s (Smith et al. 2005). This simple hypothesis could be tested by separating S0s from ellipticals, so that their fraction, f_{S0} , could be determined independently of that of ellipticals as a function of both Σ and z . If spiral transformations occurred, there should be fewer S0s in all over-dense environments at $z \simeq 1$.

Two key relationships that must be understood in the context of the above processes are the relative population fraction of the different morphological classes as functions of the local galaxy density and their location within the local gravitational potential well. The morphology-density relation (MDR) and the morphology-radius relation (MRR) have been well studied at low z (Dressler 1980; Postman and Geller 1984; Whitmore et al. 1993; Goto et al. 2003) and quantify many long-standing observations showing a preference for spheroidal systems to segregate in the cluster inner regions whereas the late-type galaxies tend to populate the outskirts of galaxy clusters.

The f_{S0} measured in all previous observational works, was inferred from f_{E+S0} rather than measured directly since it is very hard to distinguish between S0 and E galaxies from the data used in these studies. In order to understand the observational features and the physical mechanisms that drive the formation of S0s in clusters, in this chapter we present original scheme to identify E, S0 and S galaxies candidates in a simulated cluster based on the merging history of the subhaloes. The scheme consists in identifying subhaloes inside the galaxy cluster at different times and inferring their merging history. This scheme may predict different behaviour for S0s and Es that can be used to constrain better future observations of these systems and different mechanisms scenarios for their formation.

5.2 Formation of S0's: an overview

When Van den Bergh discussed his morphology classification system, he pointed out the existence of *anemic* galaxies that might represent the missing link between normal spirals and S0s. They are characterized by arms less pronounced than normal spirals, they are gas-poor, with low star formation activity, redder colors than normal spirals with similar bulge to disk ratios. The first interpretation of their existence was that, once the gas reservoir feeding the star formation is removed from cluster S galaxies, they become lenticulars (van den Bergh 1976). In a detailed analysis of the star forming properties of anemic galaxies, Elmegreen et al. (2002) concluded that their gas surface density is below the threshold for the star formation to take place and that because of the lack of supply of young stars with low velocity dispersion, the disk heats up, dumping spiral waves on time scales of a few revolutions. The anemic sequence would thus represent the intermediate phase between S galaxies and S0. However kinematic studies of nearby cluster and field S0 argue for a different nature of S galaxies and S0s. The larger scatter and a small zero point offset in the Tully-Fisher relation observed in Virgo and Coma cluster S0 galaxies compared to S indicate that S0s can

hardly be formed by simple gas removal from healthy S galaxies. In this picture much works in the past (Gunn and Gott 1972; Dressler 1980), as well as recent analytic arguments and numerical simulations (Bekki et al. 2002), discusses and suggests two main formation scenario for S0s. The **first scenario**, in which the S galaxies maintain their thin disk component, is a gradual transformation, with efficient stripping of the halo gas and, therefore, dramatically suppressed star formation. The **second scenario** is the rapid transformation of a S galaxy through a merger with another, less massive, disk galaxy. In contrast to the first case, this latter development would produce a red S0 with a thicker disk and a bigger bulge because of the triggered central starbursts and dynamical heating of both disks.

5.3 The morphology-density relation and its evolution with redshift

Morphology segregation is the strongest observational signature of a different nature of cluster galaxies. In his seminal work based on photographic plates of 55 nearby clusters including ~ 6000 galaxies Dressler (1980) showed that the fraction of ETGs (ellipticals and lenticulars) increases with the galaxy density and/or clustercentric radius (Whitmore et al. 1993)(Whitmore et al. 1993). This relation appears universal, as it holds over 6 orders of magnitude, from rich clusters to loose groups (Postman and Geller 1984). Whitmore et al. (1993) claim that the morphology-radius relation is independent of the number density within the central $0.5 Mpc$, of the X-ray luminosity or of the velocity dispersion of the cluster. f_E in the outer parts of clusters is \sim constant (10 to 16 %) at a distance $> 0.5 Mpc$. This fraction increases to 60 – 70% in the cluster center. f_{S0} rises moderately up to the central $0.2 Mpc$, then it drops sharply. On the other hand the fraction of S galaxies, f_S , decreases continuously from the outskirts ($\sim 60\%$) to the cluster center, where it drops to virtually 0%. Binggeli et al. (1990), Thuan et al. (1991) and (Sabatini et al. 2005) showed that segregation also affects dwarf galaxies, i.e. dwarf ellipticals are more frequent in dense environments while dwarf irregulars are ubiquitous. Vogt et al. (2004) showed that f_S depends inversely on the cluster X-ray temperature. They also found that, while the fraction of ellipticals is almost constant, there is a strong inverse correlation between f_S and f_{S0} constituting the remaining 85%, in other words the increase of f_S in the clusters outskirts compensates for the decrease of S0s. This effect holds in clusters of different richness, and extends beyond the virial radius. Both early- and late-type spirals are found in an

envelope surrounding the cluster core, at a mean distance of $1.5 h^{-1} Mpc$, while ellipticals are at $\sim 0.85 h^{-1} Mpc$. In distant clusters f_S is larger, f_E is \geq and the lenticular fraction is a factor of $\sim 2 - 3$ smaller than in nearby clusters (Dressler et al. 1997; Fasano et al. 2000; Postman et al. 2005).

Morphology segregation in the Coma cluster was widely studied by Andreon (1996) which showed that, while S galaxies are homogeneously distributed over the cluster, the early-type component concentrates along the direction marked by the supercluster structure. Furthermore he showed evidence for velocity segregation, with Es and S0s having significantly smaller dispersion ($\sim 700 km s^{-1}$) than S ($\sim 1300 km s^{-1}$). Moreover Kashikawa et al. (1998), showed a strong luminosity segregation in the magnitude range $-20 \leq M_R \leq -16$. Galaxies with high central light concentration have a clustering strength significantly dependent on luminosity, while objects with a low central concentration show almost no luminosity segregation. Gavazzi et al. (2006) affirm that to interpret this evidence in terms of morphology is not straightforward since, galaxy light profiles better correlate in shape with luminosity than with morphological type: both dE and low-luminosity late-type have exponential light profiles with low concentration indices.

The study of the galaxy morphology distribution in the Virgo cluster is made complex by projection effects due to the elongated $3-D$ structure of the cluster. Schindler et al. (1999) compared the distribution of galaxies cataloged in the Virgo cluster catalog with that of the X-ray emitting gas from the ROSAT All Sky Survey, and found that the two components have a similar distributions. They found no luminosity segregation and positive morphology segregation: S are more spread than Es and S0s, while nucleated dE¹ are more concentrated toward the cluster center than their non-nucleated counterparts. The SDSS and 2dF surveys made it possible to extend the study of morphology segregation to regions of low density contrast with respect to the *field*. They confirm the increase of the fraction of the red, bulge-dominated galaxies with galaxy density and cluster-centric distance (Goto et al. 2003; Hogg et al. 2003; Balogh et al. 2004; De Propris et al. 2004) that was known in rich nearby clusters.

Only a fully understanding of main physical processes acting in clusters can help to distinguish between two scenario proposed. For instance in the next section we present an overview of these processes.

¹Dwarf ellipticals that have central brightness enhancements (Binggeli et al. 1984).

5.3.1 Tidal interactions among galaxies

Tidal interactions among galaxy pairs act on gas, dust and stars, as well as on dark matter, with an efficiency depending on the gravitational bounding of the various components. This produces selective morphological transformations. Since tidal forces act as M/R^3 , if the typical galaxy radii are not too small compared to the average separation between galaxies, tidal interactions can be quite efficient at removing matter from galactic halos (Farouki and Shapiro 1981; Merritt 1983). For what concerns the star formation, both observations (Keel et al. 1985; Kennicutt et al. 1987) and simulations (Mihos et al. 1992; Iono et al. 2004) of interacting pairs show a major increase of the nuclear activity and a milder (if any) in the disk. It is intuitive that tidal interactions among galaxies are boosted in the dense cores of rich clusters of galaxies. However, due to the high relative velocities, tidal interactions among cluster galaxies, although more frequent, have significantly shorter duration than in the field ($t_{enc} \sim 10^8 \text{ yr}$), thus the effects of the perturbation are less severe. The simulations of Byrd and Valtonen (1990) (applied to S galaxies in clusters) show that tidal interactions produce enough gas inflow from the disk to the circumnuclear regions, provided that the perturbation parameter:

$$P_{gg} = (M_{comp}/M_{gal})/(d/r_{gal})^3 \quad (5.1)$$

is $P_{gg} \geq 0.006 - 0.1$ (depending on the halo to disk mass ratio), where M_{comp} is the companion mass, M_{gal} and r_{gal} are the mass and the visible disk radius of the S galaxy respectively and d is the separation between the two galaxies. A typical perturbation parameter P_{gg} for $\sim 10 \text{ kpc}$ radii galaxies in clusters can be roughly estimated assuming $M_{comp} \simeq M_{gal}$ and an average galaxy separation $\sim 200 \text{ kpc}$ inside a cluster of 2 Mpc radius including ~ 1000 objects. The resulting $P_{gg} \simeq 10.4$ is significantly smaller than the critical P_{gg} necessary for producing significant gas infall into the nucleus. This simple estimate is confirmed by (Fujita 1998), who claims that the typical perturbation induced by a single high-speed encounter among cluster galaxies is too small to significantly affect the star formation rate. His model incorporates a more realistic modeling of the star formation process based on clouds collisions, than the simple nuclear infall treated by Byrd and Valtonen (1990). Furthermore, as discussed by Merritt (1983) and by Byrd and Valtonen (1990), the frequency of galaxy-galaxy encounters in rich clusters, as measured by the inverse of the relaxation time $t_{relax} \simeq$ some 10^{10} yr , comparable to the age of the Universe, is negligibly small.

Okamoto and Nagashima (2001) and (Diaferio et al. 2001) with their hybrid N-body simulation and semi-analytical models, tried to reproduce the cluster

morphology-density or morphology-radius relations observed by Whitmore et al. (1993). They concluded that, while the distribution of elliptical galaxies in clusters can be obtained with major merging, this is not the case for the lenticular galaxies with intermediate bulge to disk ratios. Bulges can be formed by the merging of two equal mass galaxies, while the subsequent gas cooling can form disks (Diaferio et al. 2001) by unequal mass mergers of disk galaxies, where disk destruction is not complete and some rotation is retained, or minor mergers between S galaxies and their companions (the disk is heated but not destroyed). The morphology segregation is qualitatively well reproduced by the semi-analytical simulation of Springel et al. (2001). Okamoto and Nagashima (2001), however, remarked that this result is very sensitive to the assumed bulge to disk ratio of lenticular galaxies.

Among tidal interactions, Moore et al. (1999) proposed that the evolution of cluster galaxies is governed by the combined effect of multiple high speed galaxy-galaxy close (~ 50 kpc) encounters called *fly-by*. They named this process *galaxy harassment* and they observed that it depends on the collisional frequency, on the strength of the individual collisions, on the cluster's tidal field and on the distribution of the potential within galaxies. Simulations show that, at a fixed mean orbital radius, galaxies on elongated orbits experience greater harassment than objects on circular orbits. The multiple encounters heat the stellar component increasing the velocity dispersion and decreasing the angular momentum, meanwhile they make the gas to sink toward the galaxy center (Moore et al. 1996). Because of their different potential distribution, massive and dwarf galaxies react differently to galaxy harassment. N-body (both pure gravitational and hydro-dynamical) simulations of low mass ($L_*/5$ and $L_*/20$) S galaxies (represented by rotating exponential disks) in a Coma-like cluster show that, at any given galaxy radius, dark matter is more easily stripped than stars because of the different orbital distribution of the two components. At early stages a large fraction (up to 50%) of the stars are removed; the subsequent increase of binding energy, caused by the increase of the central density, makes further star stripping less efficient. The obtained stellar profiles are exponentials, when only stars are included in the initial conditions, and nucleated exponentials when the gas is added (Moore et al. 1998). The evolution of bright disk galaxies ($\sim L_*$) in clusters differs from that of low-mass systems, as it depends primarily on the depth of their potential wells and on the disk scale length. High surface brightness galaxies, those with central steeply rising rotation curves, are found relatively stable to galaxy harassment. Beside minor star losses, the effect of the interaction is a small (0.5 mag arcsec $^{-2}$) increase of the central surface brightness, an increase of the disk scale height (by a factor of 2–4) and of the central velocity dispersion, with the fading of spiral features

(Moore et al. 1999). These structural and kinematic properties resemble those of bright lenticulars. Low surface brightness galaxies, because of their low mass concentration (flat rotation curves and large disk scale lengths), are strongly perturbed by the interaction. They are expected to lose most (up to 50 – 90%) of their stars, to increase their central velocity dispersion and consequently their central surface brightness by $\sim 2 \text{ mag arcsec}^{-2}$ (Moore et al. 1999). Their resulting kinematic and structural properties resemble those of dE/dS0. Simulations of Virgo like clusters by Gnedin (2003) show that tidal heating is more effective in low- Ω_0 clusters. The maximum of the tidal forces do not always happen close to the cluster center, but during the encounters with massive galaxies or with unvirialized remnants of infalling groups of galaxies. These simulations also show that the collision rate of galaxies increases by 10 – 50% in the presence of substructures. In conclusion, galaxy harassment can effectively perturb low-luminosity galaxies because of their low-density cores and slowly rising rotation curves, thus contributing to the formation of cluster dwarf ellipticals (Moore et al. 1998), to the fueling of low-luminosity AGNs (Lake et al. 1998) and to the destruction of low surface brightness galaxies in clusters (Moore et al. 1999). The effects on massive objects should be less pronounced, with a minor increase of the disk star formation activity and an increase of the velocity dispersion in the bulge (Moore et al. 1996).

5.3.2 Ram-pressure stripping

Gunn and Gott (1972) first proposed that the inter-stellar medium (ISM) could be removed from galaxies moving at $\sim 1000 \text{ km s}^{-1}$ through the hot ($10^7 - 10^8 \text{ K}$) and dense ($\sim 10^3 - 10^4 \text{ atoms cm}^{-3}$) intergalactic medium by the ram-pressure mechanism. Ram-pressure can effectively remove the ISM if it overcomes the gravitational pressure anchoring the gas to the disk:

$$\rho_{IGM} V_{gal}^2 \geq 2\pi \Sigma_{star} \Sigma_{gas} \quad (5.2)$$

ρ_{IGM} is the density of the inter-galactic medium, V_{gal} the galaxy velocity inside the cluster, Σ_{star} is the star surface density and Σ_{gas} the gas surface density. Different N-body and SPH simulations exist in the literature trying to investigate the role of ram-pressure on gas stripping of both cluster early- and late-type galaxies, and on the possible transformation of S galaxy into S0s, or of dwarf irregulars into dSph. The various models (SPH, N-body) differ in the way they account for the cluster gas distribution (density profile), the galaxy orbits within the cluster (radial, circular, galaxy inclination with respect to the orbit), the potential distribution within the galaxy (disk vs.

bulge, with or without dark matter), the star formation (gas consumption and replenishment by recycled gas), the contribution of viscosity and/or thermal evaporation. In spite of these differences, assuming typical ICM densities and velocity dispersions observed in nearby clusters, all variations of the model concur at establishing that ram-pressure is sufficient to remove part of the ISM from galaxies on time scales comparable with their cluster crossing time (a few 10^9 yr). Radial orbits are more efficient because of the higher velocity, closer crossing to the cluster core. The efficiency of removal depends on the inclination of the galaxy disk with respect to the trajectory, with face-on interactions more efficient than edge-on or inclined encounters (Abadi et al. 1999; Quilis et al. 2000; Vollmer et al. 2001). However S galaxies on radial orbits should end up stripped because their interaction with the cluster ICM will sooner or later become face-on since the orientation of the galaxy rotation axis is conserved (Quilis et al. 2000). Because of their shallower potential well, gas removal is expected to act more efficiently on dwarf irregular galaxies than on giant S galaxies (Mori and Burkert 2000).

5.3.3 Strangulation

Galaxy strangulation, a process proposed more than 20 years ago by Larson et al. (1980) to explain the transformation of S galaxies into S0, has been recently invoked to also explain the mild gradient in the morphology fraction found outside one virial radius in a cluster at $z = 0.4$ (Treu et al. 2003). Emphasis is put on the large scale on which such a mechanism might be effective, contrary to other mechanisms previously described that, except galaxy harassment, are supposed to work on smaller scales (Treu et al. 2003). Since in normal galaxies the gas that feeds the star formation (on time scales as long as the Hubble time) comes from infall of an extended gas reservoir, the effect of removing the outer galaxy halo would be that of preventing further infall of gas into the disk. On time scales of a few Gyr the star formation would thus exhaust the available gas, quenching further star formation activity. The seminal idea of Larson et al. (1980) has been elaborated by Bekki et al. (2002). Their numerical simulations showed that even if a spiral orbits a cluster with a pericenter distance of ~ 3 core radii, $\sim 80\%$ of its halo is stripped within a few Gyr by the hydrodynamical interaction with the ICM plus the global tidal field of the cluster, preventing gas accretion into the disk, and consequently suppressing the star formation. In the end the spiral structure becomes less pronounced, and galaxies progressively becomes anemic, disk-dominated S0. They might coincide with the small percentage of passive, anemic galaxies found in the SDSS by Goto et al. (2003) at large clustercentric distances.

5.4 The morphology-density relation and its evolution with redshift

Morphology segregation is the strongest observational signature of a different nature of cluster galaxies. In his seminal work based on photographic plates of 55 nearby clusters including ~ 6000 galaxies Dressler (1980) showed that the fraction of ETGs (ellipticals and lenticulars) increases with the galaxy density and/or clustercentric radius (Whitmore et al. 1993)(Whitmore et al. 1993). This relation appears universal, as it holds over 6 orders of magnitude, from rich clusters to loose groups (Postman and Geller 1984). Whitmore et al. (1993) claim that the morphology-radius relation is independent of the number density within the central $0.5 Mpc$, of the X-ray luminosity or of the velocity dispersion of the cluster. f_E in the outer parts of clusters is \sim constant (10 to 16%) at a distance $> 0.5 Mpc$. This fraction increases to 60 – 70% in the cluster center. f_{S0} rises moderately up to the central $0.2 Mpc$, then it drops sharply. On the other hand the fraction of S galaxies, f_S , decreases continuously from the outskirts ($\sim 60\%$) to the cluster center, where it drops to virtually 0%. Binggeli et al. (1990), Thuan et al. (1991) and (Sabatini et al. 2005) showed that segregation also affects dwarf galaxies, i.e. dwarf ellipticals² are more frequent in dense environments while dwarf irregulars are ubiquitous. Vogt et al. (2004) showed that f_S depends inversely on the cluster X-ray temperature. They also found that, while the fraction of ellipticals is almost constant, there is a strong inverse correlation between f_S and f_{S0} constituting the remaining 85%, in other words the increase of f_S in the clusters outskirts compensates for the decrease of S0s. This effect holds in clusters of different richness, and extends beyond the virial radius. Both early- and late-type S galaxies are found in an envelope surrounding the cluster core, at a mean distance of $1.5 h^{-1} Mpc$, while ellipticals are at $\sim 0.85 h^{-1} Mpc$. Note that the morphology-density relation also affects distant ($z = 0.5$), rich, centrally-concentrated clusters, while it seems to avoid irregular ones (Dressler et al. 1997). In distant clusters f_S is larger, f_E is \geq and the lenticular fraction is a factor of $\sim 2 - 3$ smaller than in nearby clusters (Dressler et al. 1997; Fasano et al. 2000).

Morphology segregation in the Coma cluster was widely studied by Andreon (1996) which showed that, while S galaxies are homogeneously distributed over the cluster, the early-type component concentrates along the direction marked by the supercluster structure. Furthermore he showed evidence for velocity segregation, with Es and S0s having significantly smaller dispersion ($\sim 700 km s^{-1}$) than S ($\sim 1300 km s^{-1}$). Moreover Kashikawa

²Low-luminosity elliptical galaxies with smooth surface brightness profiles.

et al. (1998), showed a strong luminosity segregation in the magnitude range $-20 \leq M_R \leq -16$. Galaxies with high central light concentration have a clustering strength significantly dependent on luminosity, while objects with a low central concentration show almost no luminosity segregation. Gavazzi et al. (2006) affirm that to interpret this evidence in terms of morphology is not straightforward since, galaxy light profiles better correlate in shape with luminosity than with morphological type: both dE and low-luminosity late-type have exponential light profiles with low concentration indices.

The study of the galaxy morphology distribution in the Virgo cluster is made complex by projection effects due to the elongated 3-D structure of the cluster. Schindler et al. (1999) compared the distribution of galaxies cataloged in the Virgo cluster catalog with that of the X-ray emitting gas from the ROSAT All Sky Survey, and found that the two components have a similar distributions. They found no luminosity segregation and positive morphology segregation: S are more spread than Es and S0s, while nucleated dE are more concentrated toward the cluster center than their non-nucleated counterparts. The SDSS and 2dF surveys made it possible to extend the study of morphology segregation to regions of low density contrast with respect to the *field*. They confirm the increase of the fraction of the red, bulge-dominated galaxies with galaxy density and cluster-centric distance (Goto et al. 2003; Hogg et al. 2003; Balogh et al. 2004; De Propris et al. 2004) that was known in rich nearby clusters.

5.5 Our project

In order to investigate if it is possible to isolate the physical mechanisms that drive the formation of S0 galaxies in clusters, we selected from an high resolution cosmological simulation a galaxy cluster with the size of Virgo cluster and we developed an original scheme to identify elliptical, S0 and spiral galaxies candidates based on the merging history of substructures in simulated cluster.

5.5.1 Numerical method and cluster identification

In order to select galaxy cluster we use large cosmological simulation that followed the evolution of 216 millions of particles in a box of $90 Mpc$ (comoving) on side (D’Onghia et al. 2008). Cosmological parameters were taken from the best-fits for WMAP3 (Spergel 2006). This had present-day matter density parameters $\Omega_m = 0.238$; cosmological constant contribution $\Omega_\Lambda = 0.762$; baryonic contributions $\Omega_b = 0.042$; and Hubble parameters

$h = 0.73$ ($H_0 = 100 h \text{ km s}^{-1} \text{ Mpc}^{-1}$). The mass fluctuation spectrum had a spectral index $n = 0.951$, and was normalized by the linear rms fluctuation on $8 h^{-1} \text{ Mpc}$, $\sigma_8 = 0.75$. The initial conditions were generated with GRAFIC2 (Bertschinger 2001). The unperturbed particles positions were placed on a grid and initial displacements were assigned according to the Zeldovich approximation (Shandarin and Zeldovich 1989). The masses of the dark matter particles were set to $m_{DM} = 8.67 \times 10^7 h^{-1} M_\odot$. All runs started at redshifts sufficiently high to ensure that the absolute maximum density contrast is still in the linear regime. D'Onghia et al. (2008) followed particles evolution using the treecode PKDGRAV (see Chapter 1). Gravitational interactions between pairs of particles were softened in comoving coordinates with a spline softening length $\epsilon = 1.16 \text{ kpc}$; forces were completely Newtonian at twice this distance. The particles had individual time steps $\Delta t_i = 0.2 \sqrt{\epsilon a_i}$ where a is particle's acceleration. The node-opening angle (see Sec. 1.4.1) is $\theta = 0.7$ after $z = 2$ and $\theta = 0.55$ earlier to provide higher force accuracy when the density is nearly uniform.

Non-linear structures in this box with a minimum of 250 particles at $z = 0$ are identified using the classic friends-of-friends (FOF) algorithm with a linking length l equal to 0.2 times the mean comoving interparticle separation. For each FOF halo, we identify the most bound particle and adopt its position as the halo centre. Using this centre, we compute the *virial radius* of each halo, R_{vir} defined as the radius of a sphere of overdensity $\Delta(z = 0) = 93.5$ (relative to the critical density for closure)³. If a particle is a potential member of two groups, it is assigned to the most massive one. We select for our analysis an halo with masses $M = 1.44 \times 10^{14} M_\odot$, number particle $N = 1648438$ and virial radius $R_{vir} = 1.1 M_\odot$.

5.5.2 Substructures in hierarchical cosmological simulations

A basic step in the analysis of cosmological simulations is the identification of virialized particle groups, which specify the sites where luminous galaxies form. Perhaps the most popular technique employed for this task is the friends-of-friends (FOF) algorithm. It places any two particles with a separation less than some linking length b into the same group. In this way, particle groups are formed that correspond to regions approximately enclosed by isodensity contours with threshold value $\rho \propto 1/b^3$. For an appropriate

³The virial overdensity in a flat universe may be computed using the fitting formula proposed by Bryan and Norman (1998).

choice of b , groups are selected that are close to the virial overdensity predicted by the spherical collapse model. FOF is both simple and efficient, and its group catalogues agree quite well with the predictions of Press & Schechter theory. However, FOF has a tendency to link independent structures across feeble particle bridges occasionally, and in its standard form with a linking length of $b \simeq 0.2$ it is not capable of detecting substructure inside larger virialized objects. Using sufficiently high mass resolution, studies from Tormen et al. (1997, 1998); Ghigna et al. (1998); Klypin et al. (1999); Moore et al. (1999) were able to demonstrate that substructure in dense environments like groups or clusters may survive for a long time. The cores of the dark haloes of galaxies that fall into a cluster will thus remain intact, and orbit as self-gravitating objects in the smooth dark matter background of the cluster. In old simulations, haloes falling into clusters usually evaporated quickly, and the clusters exhibited little signs of substructure (e.g. Frenk et al. 1996). It now appears that sufficient numerical force and mass resolution is enough to resolve this *overmerging* problem. The identification of substructure within dark matter haloes is a challenging technical problem, and several algorithms to find *haloes within haloes* have been proposed. In hierarchical friends-of-friends (HFOF) algorithms (Klypin et al. 1999) the linking length of plain FOF is reduced in a sequence of discrete steps, thus selecting groups of higher and higher overdensity and eventually capturing true substructure. Clearly, the need for a well-posed physical definition of *substructure* arises early on in such an analysis. Most authors (Springel et al. 2001, e.g.) have required subhaloes to be locally overdense and self-bound. Note that this implies that any locally overdense region within a dense background needs to be treated with an unbinding procedure. This is because a small halo within a larger system represents only a relatively small fluctuation in density, and a substantial amount of mass within the overdense region will just stream through and not be gravitationally bound to the substructure itself. Group-finding techniques that use some criterion of self-boundness include the bound density maximum (BDM) algorithm (Klypin et al. 1999), where the bound subset of particles is evaluated iteratively in spheres around a local density maximum. In the method of Tormen et al. (1998), previous simulation outputs are used to track the infall of particle groups into larger systems. Once such a particle group from the field was accreted by a cluster, they simply determined the subset of those particles that still remained self-bound. Another approach is followed in DENMAX (Gelb and Bertschinger 1994) and its offspring SKID (Stadel 2001), where particles are moved along the local gradient in density towards a local density maximum. Particles ending up in the same maximum are then linked together as a group using FOF. SKID has been employed by (Ghigna et al. 1998) to find substructure in a rich cluster of galaxies, and

to study the statistical properties of the detected subgroups. Integrating the gradient of the density field and moving the particles is not without technical subtleties. For example, a suitable stopping condition is needed. The algorithm HOP of Eisenstein and Hut (1998) tries to avoid these difficulties by restricting the group search to the set of original particle positions, just as FOF does. In HOP, one first obtains an estimate of the local density for each particle, and then attaches it to its densest neighbour. In this way a set of disjoint particle groups are formed. However, a number of additional rules are needed to link and prune some of these groups. For example, HOP may split up a single virialized clump into several pieces of unphysical shape, which have to be joined using auxiliary criteria. Springel et al. (2001) built a new algorithm to detect substructure in dark matter haloes that incorporates ideas from SKID, HOP and FOF. For our purpose we use the subhalo finder AMIGA (Adaptive Mesh Investigations of Galaxy Assembly) (Gill et al. 2004) and we describe its main properties in the next section.

5.5.3 AMIGA

The halo finder AMIGA, essentially uses the adaptive grids of MLAPM (Knebe et al. 2001) to locate the satellites of the host halo. AMIGA's adaptive refinement meshes follow the density distribution by construction. Grid structure *surrounds* the satellites, as the satellites are simply manifestations of overdensities within (and exterior) to the underlying host halo. The advantage of reconstructing and using these grids to locate haloes is that they naturally follow the density field with the exact accuracy of the N-body code. No scaling length is required, in contrast with techniques such as FOF. Therefore AMIGA avoids one of the major complications inherent to most halo finding-schemes as a natural consequence of its construction. To locate appropriate haloes within the simulation outputs the code first build a list of *potential centres* for the haloes. Assuming that each of these peaks is the centre of a halo, it steps out in (logarithmically spaced) radial bins until the density reaches $\rho_{\text{satellite}}(r_{\text{vir}}) = \Delta_{\text{vir}}(z)\rho_b(z)$, where ρ_b is the universal background density, unless it reaches a point r_{trunc} where an upturn in the radial density profile is detected. The outer radius of the satellite is defined to be either r_{vir} or r_{trunc} , whichever is smaller, and dubbed r_{AHF} . Using all particles interior to r_{AHF} the code calculates other canonical properties for each halo such as its mass, rotation curve and velocity dispersion. To have the list of haloes by removing gravitationally unbound particles and duplicate haloes first, for each satellite a set of *duplicate candidates* is constructed based on the criterion that their centres lie within each others outer radii r_{AHF} . Secondly, this list is then checked by comparing the internal prop-

erties of the candidates. A candidate is affirmed to be a duplicate once its mass, velocity dispersion and centre of mass velocity vector agree to within 80 per cent. The code then keeps the halo with the higher central density and removes the other one from the satellite catalogue completely. With the complete set of haloes now in hand, the code proceeds to remove gravitationally unbound particles. This again is done in an iterative process. Starting with the halo centre, it calculates the kinetic and potential energy for each individual particle in the respective reference frame and all particles faster than two times the escape velocity are removed from the halo. Then it recalculates the centre, and proceeds through the process again. This pruning is halted when a given halo holds fewer than eight particles or when no further particles need to be removed. It finishes by recalculating the internal properties of the haloes with the radial density profiles of the satellites fitted to the functional form proposed by Navarro, Frenk & White in the range from $8h^{-1} \text{ kpc}$ to r_{AHF} .

5.5.4 Following the merger tree

For each simulation outputs, we compile a list of dark matter haloes by using AMIGA. We include only groups with at least 200 ($\sim 1.5 \cdot 10^{10} M_{\odot}$) particles in the halo catalogue. At $z = 0$ we find 116 subhaloes in our cluster with this property. For each halo, AMIGA is able to determine the most-bound particle within the group, where \check{S} most bound here refers to the particle with the minimum binding energy.

We follow the merger tree of the dark matter subhaloes from output to output. A subhalo H_B at redshift z_B is defined to be a progenitor of a subhalo H_A at redshift z_A , if at least the 20% of the particles of H_B are contained within H_A , and the most bound particle of H_B is contained in H_A , too. We iterate the procedure at previous redshift only for the most massive progenitor. In this way we are able to follow all subhaloes that AMIGA find at $z = 0$.

5.5.5 Defining E/S0 population

In order to determine which kind of galaxy (E, S0 or S) our subhaloes host at $z = 0$, we elaborated a new method that is able to determine a morphological classification without using semi-analytical models or hydrodynamical simulations.

First we divided our sample in two class: *early-* and *late-* subhaloes. The first class contains all subhalos that have at some redshift $v_c \geq 180 \text{ km/s}$ and the second $v_c \leq 180 \text{ km/s}$. This threshold is obtained following (Salucci

et al. 2007), where we found that disc masses M_D of spirals are in the range $10^9 M_\odot \leq M_D \leq 210^{11} M_\odot$. We put this upper bound value in the relation between the disc mass and the virial mass $M_D - M_{vir}$ by (Shankar et al. 2006):

$$M_D = 2.3 \times 10^{10} M_\odot \frac{[M_{vir}/(3 \times 10^{11} M_\odot)]^{3.1}}{1 + [M_{vir}/(3 \times 10^{11} M_\odot)]^{2.2}} \quad (5.3)$$

and we found $M_{vir} \sim 1 \times 10^{12} M_\odot$ that corresponds to $v_c \sim 180 \text{ km/s}$. We imposed that subhaloes in the first class can host E and S0 galaxies, while in the second we found S galaxies. In order to distinguish E from S0 galaxies in the early-type class we only looked at mass accretion history (hereafter MAH) of early-type subhaloes. First we found that all these subhaloes joined the cluster at $z \sim 0.5$, after that we compared the subhaloes mass at this redshift, $M_{0.5}$, to the subhaloes mass at $z = 0$, M_0 . If we found $M_{0.5} < M_0$ or $M_{0.5} > M_0$ we defined these objects S0 according to the first and the second formation scenario respectively (see Sec. 5.2), while if $M_{0.5} \sim M_0$ we defined this subhalo an E system. In Fig. 5.1 and 5.2 we show several examples of MAH of subhaloes (ordered in mass) found in our cluster.

5.6 Preliminary results and open issues

According to the classification presented in the last section, we determined at $z = 0$ the MRR and we compared it to the current data and previous works. In Fig. 5.3 we show the subhaloes fraction as function of the distance from the center of the cluster normalized to the virial radius of the cluster R_{vir} . Red points are our results obtained counting subhaloes in concentric circular shells given by a linear radial sampling. Blue points are derived from the Fig. 11 in Springel et al. (2001), where the authors obtained the galaxy fraction after to apply a semi-analytical model to a cluster simulation. Finally, green points are observations from Whitmore and Gilmore (1991). We note that given our classification we can reproduce the trends for the fraction of S0 and E as a function of the radius in reasonable agreement with the current observational data. In particular the fraction of candidate S galaxies in our simulations seems to decrease significantly from the outskirts toward the cluster center, whereas the fraction of S0 candidate galaxies seem to be more radius independent within half of the virial radius, although the large uncertainties. A similar trend is also followed by the radial distribution of the E galaxies in our sample.

We have also investigate another feature of galaxies: the luminosity function. By using data of Binggeli et al. (1987) for galaxies in Virgo cluster, we

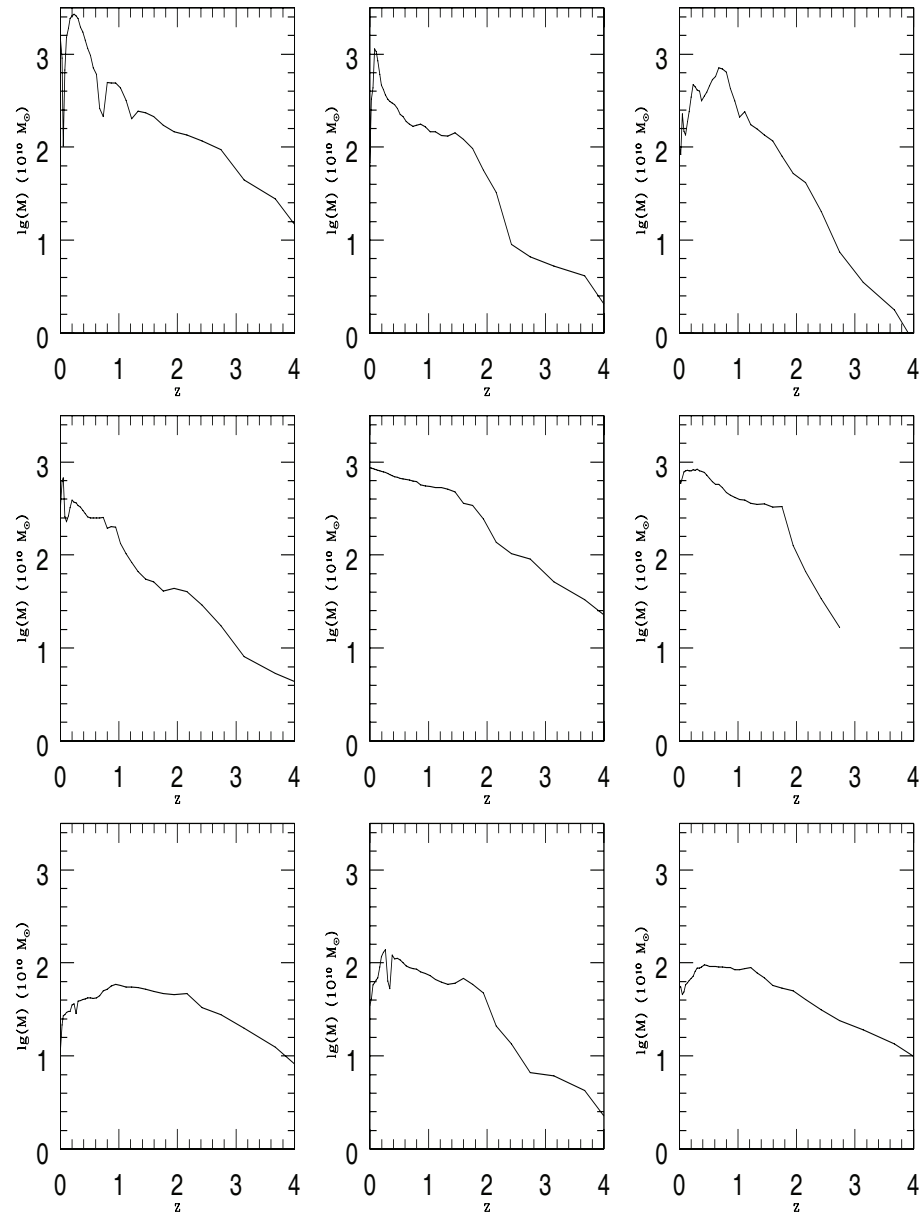


Figure 5.1: Mass accretion history for several subhaloes in our sample.

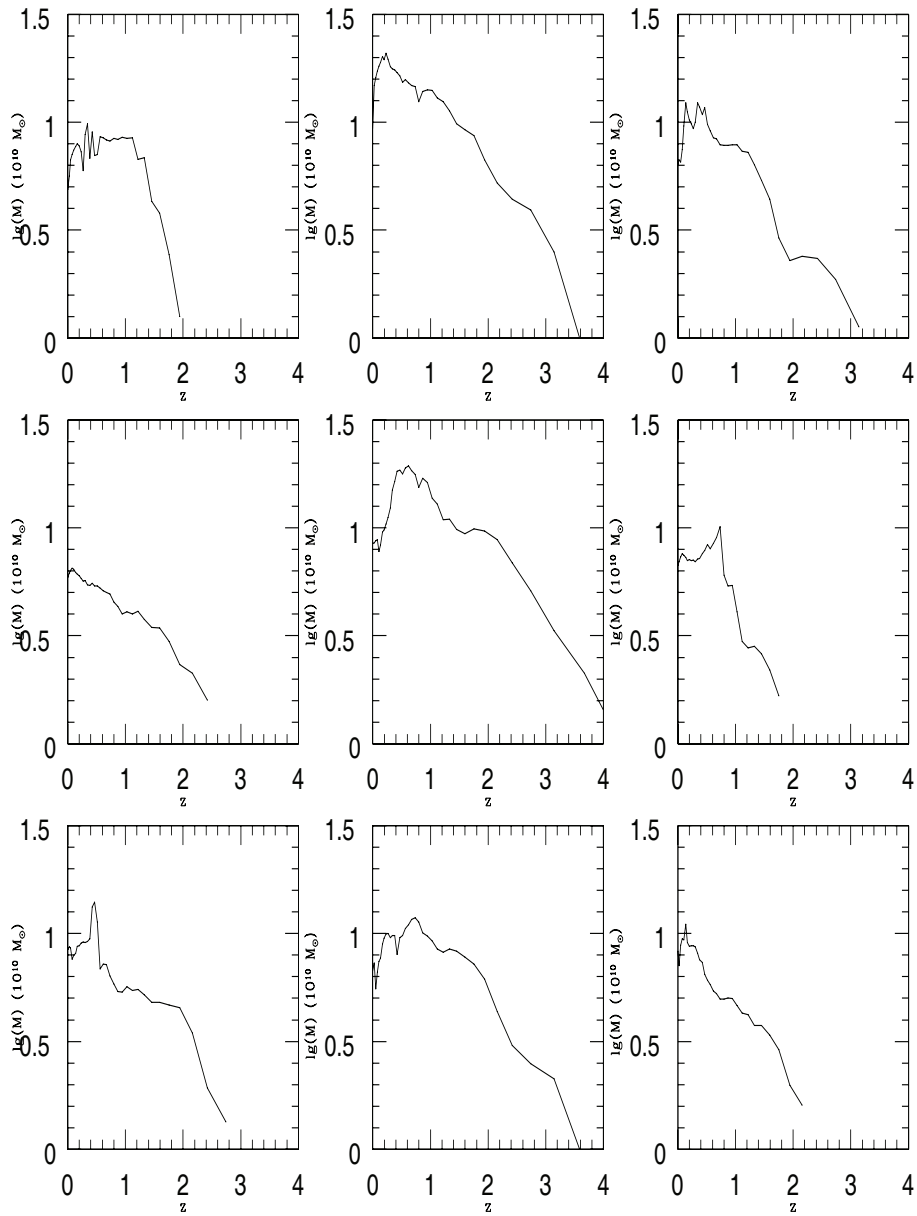


Figure 5.2: Mass accretion history for several subhaloes in our sample.

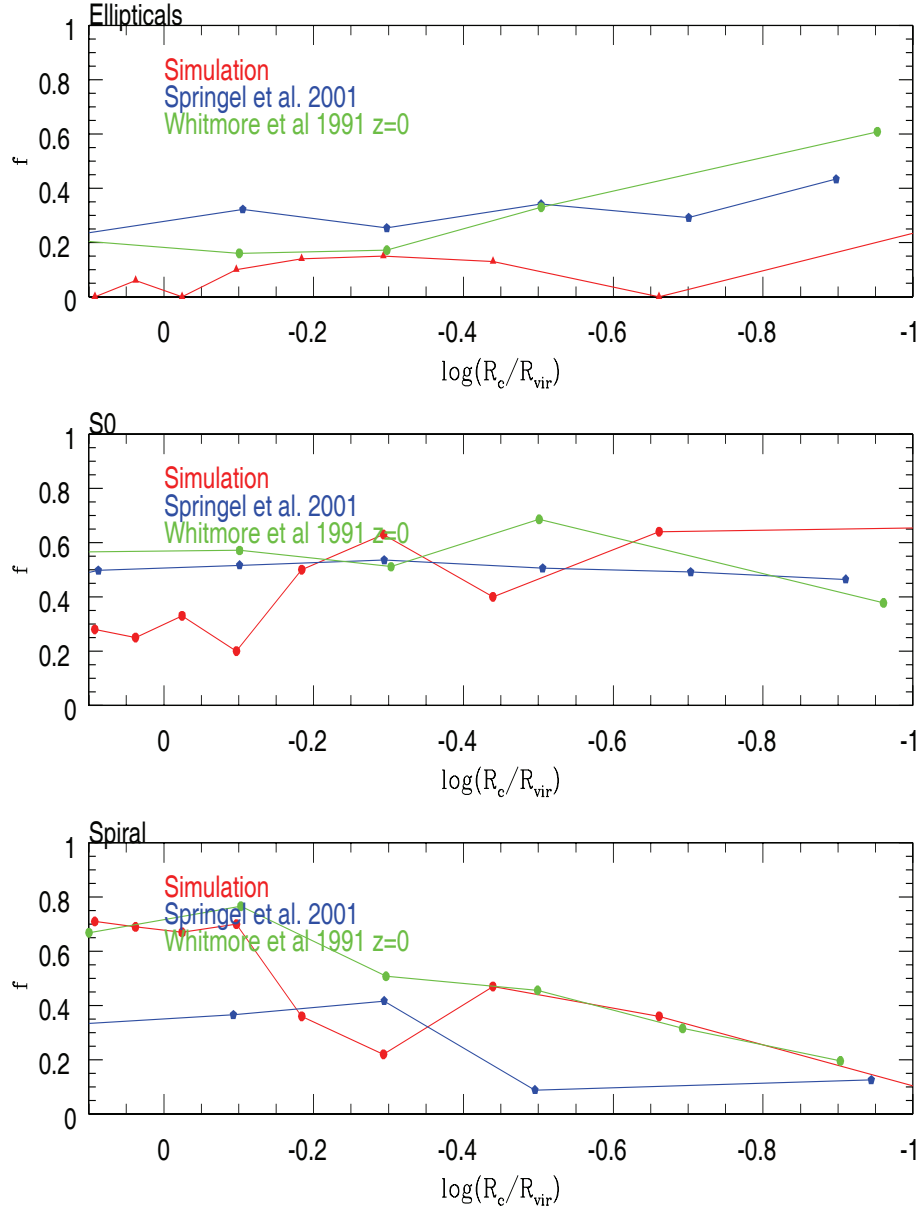


Figure 5.3: Morphological mix of galaxies as a function of clustercentric radius. From top to bottom, red points in the three panels show the relative fraction of E, S0, and S galaxies in spherical shells around the cluster center. Blue points are from Springel et al. (2001). Green points show the observational results of Whitmore and Gilmore (1991). Note that we here follow these authors in letting the radius decrease to the right, i.e., the cluster centre is found on the right-hand side of the diagrams.

reproduced the differential luminosity function for Es and S0s in this sample and we compared it to the differential velocity distribution function obtained by using our simulation. We use the velocity distribution because in our simulation we do not have baryonic component, thus we convert the luminosity of the data in velocity. In order to determine v_{max} for real galaxies in Virgo from the absolute magnitude, we determined the v_c ⁴ by using the Faber-Jackson relation (Faber and Jackson 1976) from (Bernardi et al. 2007):

$$\log \sigma_0 = 2.159 - 0.130(M_r + 21), \quad (5.4)$$

where we converted our M_B magnitude in r-band by using the constant color term $B - r = 1.32$ according to (Fukugita et al. 1995). After that, we derived v_{max} from σ_0 adopting the relation between these two quantities derived in Pizzella et al. (2005):

$$v_{max} = (1.32 \pm 0.09)\sigma_0 + (46 \pm 14) [km s^{-1}] \quad (5.5)$$

Fig. 5.4 shows the differential velocity distribution inferred from the real S0s in the Virgo cluster (red line) as compared to the S0 candidate galaxies (black line) obtained in our simulations. Binggeli et al. (1987), found that the observed distribution of S0s in Virgo cluster is bimodal with two peaks: one for the relatively low mass S0s (with maximum circular velocity around $85 km/s$) and the other for high mass S0s (with v_{max} around $150 km/s$). It is encouraging to note that our scheme can reproduce this bimodal distribution. However the simulation used for this work suffers of low resolution. Hence the number of substructures that we included in our analysis is lower than total abundance of the Virgo cluster members. As a future work, in order to further test the above subhalo finder algorithm and to better compare our results with observational data, we plan to analyze different simulated clusters with improved mass and spatial resolution.

⁴This is an approximation that may lead to a systematic underestimate of the true v_{max} at the sub-halo virial radius by some 10% (see Salucci et al. 2007).

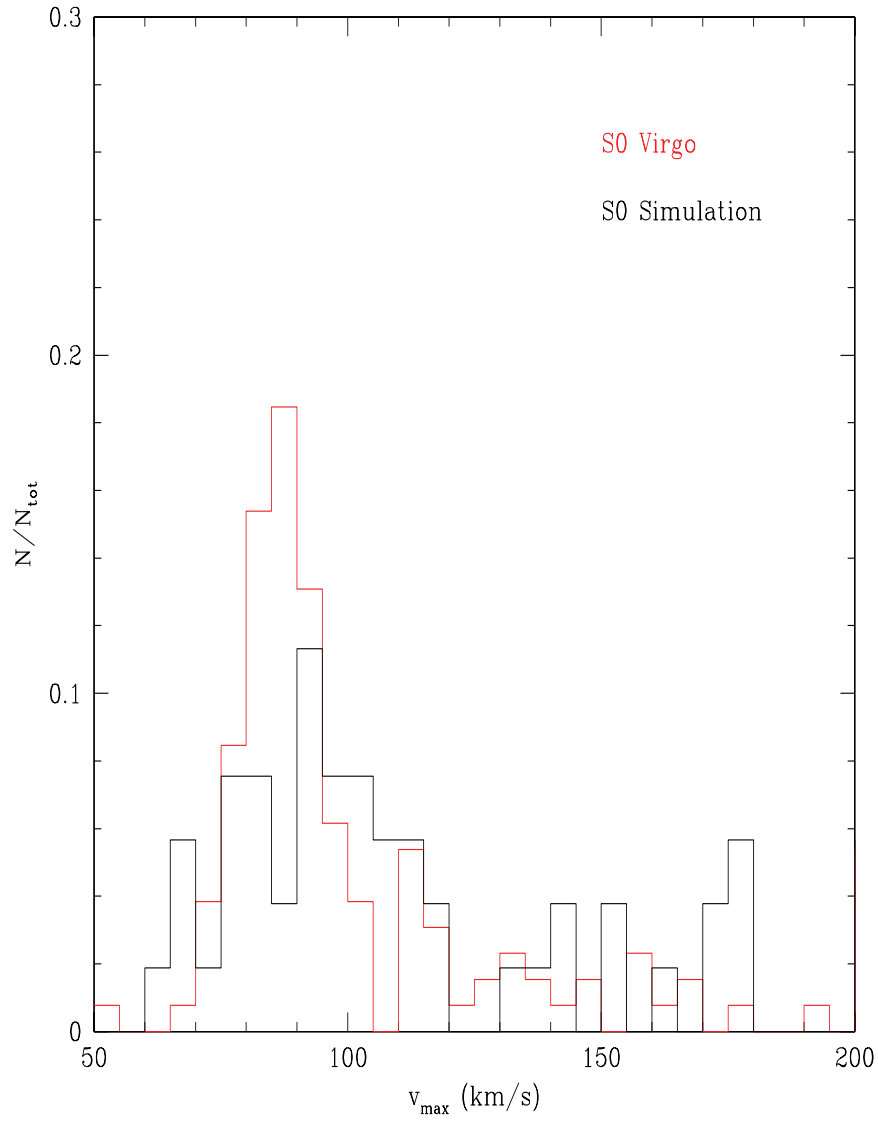


Figure 5.4: Differential velocity distribution inferred from the real S0s in the Virgo cluster (red line) as compared to the S0 candidate galaxies (black line) obtained in our simulations (see text for details).

Summary

In the present work we have used N-body techniques to study the effect of galaxy-galaxy encounters on the properties of different galaxy types, from spheroidal to gas-rich disk systems. The analysis has been mainly performed through newtonian simulations, though some part of the work also involved cosmological simulations. In particular, we explored (i) the effects of dissipationless merging on the scaling relation and internal color gradients of early-type galaxies; (ii) the issue of rebuilding late-type systems from mergers of gas-rich, disk-dominated galaxies; and (iii) we have analyzed the merging history of different galaxy types (E, S0, Sp) from cosmological simulations of clusters of galaxies.

The main results of this thesis are reported in the abstract, while the conclusions of (i) part are reported at the end of chapter 2 and 3, while conclusions of parts (ii) and (iii) are reported at the end of chapters 4 and 5.

Appendix A

Equilibrium of dark and luminous matter

We consider the Eddington formula (Eddington 1916):

$$f(\mathcal{E}) = \frac{1}{\sqrt{8\pi^2}} \left[\int_0^{\mathcal{E}} \frac{d^2\rho_T}{d\Psi_T^2} \frac{d\Psi_T}{\sqrt{\mathcal{E} - \Psi_T}} + \frac{1}{\sqrt{\mathcal{E}}} \left(\frac{d\rho_T}{d\Psi_T} \right)_{\Psi_T=0} \right], \quad (\text{A.1})$$

and we underline that we have no guarantee that the solution to equations A.1 will satisfy the physical requirement that it be nowhere negative. Indeed, it is possible to show (Binney and Tremaine 1994) that a spherical density distribution can be that of a system whose distribution function depends only on E if and only if

$$\frac{d^2\rho_T}{d\Psi_T^2} = \frac{d^2\rho_T}{dr^2} \left(\frac{d\Psi_T}{dr} \right)^{-2} - \frac{d\rho_T}{dr} \left(\frac{d\Psi_T}{dr} \right)^{-3}. \quad (\text{A.2})$$

$$\frac{d^2\Psi}{dr^2} = \left(\frac{d\Psi_T}{dr} \right)^{-3} \left[\frac{d^2\rho_T}{dr^2} \left(\frac{d\Psi_T}{dr} \right) - \left(\frac{d\rho_T}{dr} \right) \frac{d^2\Psi}{dr^2} \right] \geq 0. \quad (\text{A.3})$$

Considering that $\frac{d\Psi_T}{dr}$ is negative, then our condition become:

$$\left[\frac{d^2\rho_T}{dr^2} \left(\frac{d\Psi_T}{dr} \right) - \left(\frac{d\rho_T}{dr} \right) \frac{d^2\Psi}{dr^2} \right] \leq 0, \quad (\text{A.4})$$

and since $\Psi = -\Phi + \Phi_0$ we have:

$$\left[\frac{d^2\rho_T}{dr^2} \left(\frac{d\Phi_T}{dr} \right) - \left(\frac{d\rho_T}{dr} \right) \frac{d^2\Phi}{dr^2} \right] \geq 0. \quad (\text{A.5})$$

Now we insert $\Phi_T = \Phi_L + \Phi_{DH}$ and $\rho_T = \rho_L + \rho_{DH}$ and we obtain:

$$\left[\frac{d^2 \rho_T}{dr^2} \left(\frac{d\Phi_T}{dr} \right) - \left(\frac{d\rho_T}{dr} \right) \frac{d^2 \Phi}{dr^2} \right] = \left[\frac{d^2 \rho_{DH}}{dr^2} \frac{d\Phi_{DH}}{dr} - \frac{d\rho_{DH}}{dr} \frac{d^2 \Phi_{DH}}{dr^2} \right] \quad (\text{A.6})$$

$$\left[\frac{d^2 \rho_L}{dr^2} \frac{d\Phi_L}{dr} - \frac{d\rho_L}{dr} \frac{d^2 \Phi_L}{dr^2} \right] - \left[\frac{d\rho_L}{dr} \frac{d^2 \Phi_{DH}}{dr^2} - \frac{d\rho_{DH}}{dr} \frac{d^2 \Phi_L}{dr^2} \right] \geq 0 \quad (\text{A.7})$$

For our model the stellar mass density and dark matter density can be write as:

$$\rho_L(r) = \frac{\mathcal{M}_L b^{2n}}{R_{eL}^3 2\pi n \Gamma(2n)} \tilde{\rho}\left(\frac{r}{R_{eL}}\right), \quad (\text{A.8})$$

and

$$\rho_{DH}(r) = \frac{\mathcal{M}_{DH} b^{2m}}{R_{eDH}^3 2\pi m \Gamma(2m)} \tilde{\rho}\left(\frac{r}{R_{eDH}}\right), \quad (\text{A.9})$$

where $\tilde{\rho}\left(\frac{r}{R_e}\right) = \frac{b^n \alpha^{1-n}}{\pi} \mathcal{C}_n^0(\alpha)$. We have defined $x = \frac{r}{R_{eL}}$, $x_D = \frac{R_{eDH}}{R_{eL}}$ and $\mu = \frac{\mathcal{M}_{DH}}{\mathcal{M}_L}$. Now we calculate the derivatives to insert in A.6:

$$\frac{d\rho_L}{dr} = \frac{\mathcal{M}_L}{R_{eL}^4} \frac{b^{2n}}{2\pi n \Gamma(2n)} \frac{d\tilde{\rho}}{dx} \Big|_{x=r/R_{eL}}, \quad (\text{A.10})$$

$$\frac{d\rho_{DH}}{dr} = \frac{\mathcal{M}_L}{R_{eL}^4} \frac{\mu}{x_D^4} \frac{b^{2m}}{2\pi m \Gamma(2m)} \frac{d\tilde{\rho}}{dx} \Big|_{x=x/x_D}, \quad (\text{A.11})$$

$$\frac{d^2 \rho_L}{dr^2} = \frac{\mathcal{M}_L}{R_{eL}^5} \frac{b^{2n}}{2\pi n \Gamma(2n)} \frac{d^2 \tilde{\rho}}{dx^2} \Big|_{x=r/R_{eL}}, \quad (\text{A.12})$$

and

$$\frac{d^2 \rho_{DH}}{dr^2} = \frac{\mathcal{M}_L}{R_{eL}^5} \frac{\mu}{x_D^5} \frac{b^{2m}}{2\pi m \Gamma(2m)} \frac{d^2 \tilde{\rho}}{dx^2} \Big|_{x=x/x_D}. \quad (\text{A.13})$$

The derivatives of the gravitational potential are:

$$\frac{d\Phi_L}{dr} = \frac{G\mathcal{M}_L}{R_{eL}^2} \frac{\widetilde{M}(x)}{x^2} \Big|_{x=r/R_{eL}}, \quad (\text{A.14})$$

$$\frac{d\Phi_{DH}}{dr} = \frac{G\mathcal{M}_L}{R_{eL}^2} \frac{\mu}{x_D^2} \frac{\widetilde{M}(x/x_D)}{(x/x_D)^2} \Big|_{x=r/R_{eL}}, \quad (\text{A.15})$$

$$\frac{d^2 \Phi_L}{dr^2} = 4\pi G \frac{\mathcal{M}_L}{R_{eL}^3} \frac{b^{2n}}{2\pi n \Gamma(2n)} \widetilde{\Phi}_L(x) - \frac{2}{R_{eL}} \frac{1}{x} \frac{d\Phi_L}{dr} \quad (\text{A.16})$$

and

$$\frac{d^2\Phi_{DH}}{dr^2} = G \frac{\mathcal{M}_L}{R_{eL}^3} \frac{\mu}{x_D^3} \left[\frac{2b^{2m}}{m\Gamma(2m)} \tilde{\Phi}_{DH}(x/x_D) - \frac{2M(x/x_D)}{(x/x_D)^3} \right], \quad (\text{A.17})$$

where $\tilde{\Phi}(s) = \int_s^\infty \frac{\tilde{L}_n(x)}{x^2} dx$. By replacing these quantities in A.6 we can obtain the condition to impose on parameters so that $f_T(\varepsilon)$ is non negative.

Bibliography

- S. J. Aarseth. Dynamical evolution of clusters of galaxies, I. *MNRAS* , 126: 223–+, 1963.
- M. G. Abadi, B. Moore, and R. G. Bower. Ram pressure stripping of spiral galaxies in clusters. *MNRAS* , 308:947–954, October 1999.
- S. Andreon. The morphological segregation of galaxies in clusters. II. The properties of galaxies in the Coma cluster. *A&A* , 314:763–775, October 1996.
- N. Arimoto and Y. Yoshii. Chemical and photometric properties of a galactic wind model for elliptical galaxies. *A&A* , 173:23–38, February 1987.
- V. Avila-Reese. Understanding Galaxy Formation and Evolution. *ArXiv Astrophysics e-prints*, May 2006.
- V. Avila-Reese and C. Firmani. Properties of Disk Galaxies in a Hierarchical Formation Scenario. *Revista Mexicana de Astronomia y Astrofisica*, 36: 23–+, April 2000.
- V. Avila-Reese, C. Firmani, and X. Hernández. On the Formation and Evolution of Disk Galaxies: Cosmological Initial Conditions and the Gravitational Collapse. *ApJ* , 505:37–49, September 1998. doi: 10.1086/306136.
- R. Bacon, Y. Copin, G. Monnet, B. W. Miller, J. R. Allington-Smith, M. Bureau, C. M. Carollo, R. L. Davies, E. Emsellem, H. Kuntschner, R. F. Peletier, E. K. Verolme, and P. T. de Zeeuw. The SAURON project - I. The panoramic integral-field spectrograph. *MNRAS* , 326:23–35, September 2001. doi: 10.1046/j.1365-8711.2001.04612.x.
- M. L. Balogh, I. K. Baldry, R. Nichol, C. Miller, R. Bower, and K. Glazebrook. The Bimodal Galaxy Color Distribution: Dependence on Luminosity and Environment. *ApJL* , 615:L101–L104, November 2004. doi: 10.1086/426079.

- J. Barnes and P. Hut. A Hierarchical O(NlogN) Force-Calculation Algorithm. *Nature* , 324:446–449, December 1986.
- J. E. Barnes. Encounters of disk/halo galaxies. *ApJ* , 331:699–717, August 1988. doi: 10.1086/166593.
- J. E. Barnes. Evolution of compact groups and the formation of elliptical galaxies. *Nature* , 338:123–126, March 1989. doi: 10.1038/338123a0.
- J. E. Barnes. Transformations of galaxies. I - Mergers of equal-mass stellar disks. *ApJ* , 393:484–507, July 1992. doi: 10.1086/171522.
- J. E. Barnes and L. Hernquist. Transformations of Galaxies. II. Gasdynamics in Merging Disk Galaxies. *ApJ* , 471:115–+, November 1996. doi: 10.1086/177957.
- K. Bekki. The Fundamental Plane and Merger Scenario. I. Star Formation History of Galaxy Mergers and Origin of the Fundamental Plane. *ApJ* , 496:713–+, March 1998. doi: 10.1086/305411.
- K. Bekki, W. J. Couch, and Y. Shioya. Passive Spiral Formation from Halo Gas Starvation: Gradual Transformation into S0s. *ApJ* , 577:651–657, October 2002. doi: 10.1086/342221.
- E. F. Bell, C. Wolf, K. Meisenheimer, H.-W. Rix, A. Borch, S. Dye, M. Kleinheinrich, L. Wisotzki, and D. H. McIntosh. Nearly 5000 Distant Early-Type Galaxies in COMBO-17: A Red Sequence and Its Evolution since $z \sim 1$. *ApJ* , 608:752–767, June 2004. doi: 10.1086/420778.
- E. F. Bell, T. Naab, D. H. McIntosh, R. S. Somerville, J. A. R. Caldwell, M. Barden, C. Wolf, H.-W. Rix, S. V. Beckwith, A. Borch, B. Häussler, C. Heymans, K. Jahnke, S. Jogee, S. Koposov, K. Meisenheimer, C. Y. Peng, S. F. Sanchez, and L. Wisotzki. Dry Mergers in GEMS: The Dynamical Evolution of Massive Early-Type Galaxies. *ApJ* , 640:241–251, March 2006. doi: 10.1086/499931.
- R. Bender, P. Surma, S. Doebereiner, C. Moellenhoff, and R. Madejsky. Isophote shapes of elliptical galaxies. II - Correlations with global optical, radio and X-ray properties. *A&A* , 217:35–43, June 1989.
- A. J. Benson, R. G. Bower, C. S. Frenk, and S. D. M. White. Diffuse X-ray emission from late-type galaxy haloes. *MNRAS* , 314:557–565, May 2000.

- M. Bernardi, R. K. Sheth, E. Tundo, and J. B. Hyde. Selection Bias in the $M - \sigma$ and $M - L$ Correlations and Its Consequences. *ApJ* , 660:267–275, May 2007. doi: 10.1086/512719.
- E. Bertschinger. Multiscale Gaussian Random Fields and Their Application to Cosmological Simulations. *ApJS* , 137:1–20, November 2001. doi: 10.1086/322526.
- B. Binggeli and H. Jerjen. Is the shape of the luminosity profile of dwarf elliptical galaxies an useful distance indicator? *A&A* , 333:17–26, May 1998.
- B. Binggeli, A. Sandage, and M. Tarenghi. Studies of the Virgo Cluster. I - Photometry of 109 galaxies near the cluster center to serve as standards. *AJ* , 89:64–82, January 1984. doi: 10.1086/113484.
- B. Binggeli, G. A. Tammann, and A. Sandage. Studies of the Virgo cluster. VI - Morphological and kinematical structure of the Virgo cluster. *AJ* , 94:251–277, August 1987. doi: 10.1086/114467.
- B. Binggeli, M. Tarenghi, and A. Sandage. The abundance and morphological segregation of dwarf galaxies in the field. *A&A* , 228:42–60, February 1990.
- J. Binney. The physics of dissipational galaxy formation. *ApJ* , 215:483–491, July 1977.
- J. Binney and S. Tremaine. *Galactic Dynamics*. 1994.
- M. R. Blanton, D. Eisenstein, D. W. Hogg, D. J. Schlegel, and J. Brinkmann. Relationship between Environment and the Broadband Optical Properties of Galaxies in the Sloan Digital Sky Survey. *ApJ* , 629:143–157, August 2005. doi: 10.1086/422897.
- G. R. Blumenthal, S. M. Faber, J. R. Primack, and M. J. Rees. Formation of galaxies and large-scale structure with cold dark matter. *Nature* , 311: 517–525, October 1984.
- R. G. Bower. The evolution of groups of galaxies in the Press-Schechter formalism. *MNRAS* , 248:332–352, January 1991.
- R. G. Bower, J. R. Lucey, and R. S. Ellis. Precision photometry of early-type galaxies in the Coma and Virgo clusters: A test of the universality of the colour-magnitude relation. I - The data. II. Analysis. *MNRAS* , 254: 589–613, February 1992a.

- R. G. Bower, J. R. Lucey, and R. S. Ellis. Precision Photometry of Early Type Galaxies in the Coma and Virgo Clusters - a Test of the Universality of the Colour / Magnitude Relation - Part Two - Analysis. *MNRAS* , 254: 601–+, February 1992b.
- G. Bruzual A. Spectral evolution of galaxies. I - Early-type systems. *ApJ* , 273:105–127, October 1983. doi: 10.1086/161352.
- G. L. Bryan and M. L. Norman. Statistical Properties of X-Ray Clusters: Analytic and Numerical Comparisons. *ApJ* , 495:80–+, March 1998. doi: 10.1086/305262.
- J. S. Bullock, A. Dekel, T. S. Kolatt, A. V. Kravtsov, A. A. Klypin, C. Porciani, and J. R. Primack. A Universal Angular Momentum Profile for Galactic Halos. *ApJ* , 555:240–257, July 2001. doi: 10.1086/321477.
- K. Bundy, R. S. Ellis, C. J. Conselice, J. E. Taylor, M. C. Cooper, C. N. A. Willmer, B. J. Weiner, A. L. Coil, K. G. Noeske, and P. R. M. Eisenhardt. The Mass Assembly History of Field Galaxies: Detection of an Evolving Mass Limit for Star-Forming Galaxies. *ApJ* , 651:120–141, November 2006. doi: 10.1086/507456.
- A. Burkert. The Structure of Dark Matter Halos in Dwarf Galaxies. *ApJL* , 447:L25+, July 1995. doi: 10.1086/309560.
- D. Burstein, S. M. Faber, C. M. Gaskell, and N. Krumm. Old stellar populations. I - A spectroscopic comparison of galactic globular clusters, M31 globular clusters, and elliptical galaxies. *ApJ* , 287:586–609, December 1984. doi: 10.1086/162718.
- D. Burstein, L. C. Ho, J. P. Huchra, and L. M. Macri. The K-Band Luminosities of Galaxies: Do S0s Come from Spiral Galaxies? *ApJ* , 621: 246–255, March 2005. doi: 10.1086/427408.
- G. Busarello, M. Capaccioli, S. Capozziello, G. Longo, and E. Puddu. The relation between the virial theorem and the fundamental plane of elliptical galaxies. *A&A* , 320:415–420, April 1997.
- G. Byrd and M. Valtonen. Tidal generation of active spirals and S0 galaxies by rich clusters. *ApJ* , 350:89–94, February 1990. doi: 10.1086/168362.
- N. Caon, M. Capaccioli, and M. D’Onofrio. On the Shape of the Light Profiles of Early Type Galaxies. *MNRAS* , 265:1013–+, December 1993.

- M. Capaccioli. Photometry of early-type galaxies and the $R \propto r^{1/4}$ law. In H. G. Corwin, Jr. and L. Bottinelli, editors, *World of Galaxies (Le Monde des Galaxies)*, pages 208–227, 1989.
- M. Capaccioli, E. V. Held, H. Lorenz, and M. Vietri. Photographic and CCD surface photometry of the standard elliptical galaxy NGC 3379. *AJ* , 99: 1813–1822, June 1990. doi: 10.1086/115459.
- M. Capaccioli, N. Caon, and M. D’Onofrio. Families of galaxies in the $\mu(e)$ - $R(e)$ plane. *MNRAS* , 259:323–327, November 1992.
- P. Capak, R. G. Abraham, R. S. Ellis, B. Mobasher, N. Scoville, K. Sheth, and A. Koekemoer. The Effects of Environment on Morphological Evolution at $0 < z < 1.2$ in the COSMOS Survey. *ApJS* , 172:284–294, September 2007. doi: 10.1086/518424.
- H. V. Capelato, R. R. de Carvalho, and R. G. Carlberg. Mergers of Dissipationless Systems: Clues about the Fundamental Plane. *ApJ* , 451:525–+, October 1995. doi: 10.1086/176240.
- M. Cappellari, R. Bacon, M. Bureau, M. C. Damen, R. L. Davies, P. T. de Zeeuw, E. Emsellem, J. Falcón-Barroso, D. Krajnović, H. Kuntschner, R. M. McDermid, R. F. Peletier, M. Sarzi, R. C. E. van den Bosch, and G. van de Ven. The SAURON project - IV. The mass-to-light ratio, the virial mass estimator and the Fundamental Plane of elliptical and lenticular galaxies. *MNRAS* , 366:1126–1150, March 2006. doi: 10.1111/j.1365-2966.2005.09981.x.
- R. G. Carlberg. Dissipative formation of an elliptical galaxy. *ApJ* , 286: 403–415, November 1984. doi: 10.1086/162615.
- R. G. Carlberg, H. M. P. Couchman, and P. A. Thomas. Cosmological velocity bias. *ApJL* , 352:L29–L32, April 1990. doi: 10.1086/185686.
- P. Catelan and T. Theuns. Non-linear evolution of the angular momentum of protostructures from tidal torques. *MNRAS* , 282:455–469, September 1996.
- B. Catinella, R. Giovanelli, and M. P. Haynes. Template Rotation Curves for Disk Galaxies. *ApJ* , 640:751–761, April 2006. doi: 10.1086/500171.
- R. Cen and J. P. Ostriker. Galaxy formation and physical bias. *ApJL* , 399: L113–L116, November 1992. doi: 10.1086/186620.

- A. Cimatti, E. Daddi, M. Mignoli, L. Pozzetti, A. Renzini, G. Zamorani, T. Broadhurst, A. Fontana, P. Saracco, F. Poli, S. Cristiani, S. D’Odorico, E. Giallongo, R. Gilmozzi, and N. Menci. The K20 survey. I. Disentangling old and dusty star-forming galaxies in the ERO population. *A&A* , 381: L68–L72, January 2002. doi: 10.1051/0004-6361:20011696.
- A. Cimatti, E. Daddi, and A. Renzini. Mass downsizing and “top-down” assembly of early-type galaxies. *A&A* , 453:L29–L33, July 2006. doi: 10.1051/0004-6361:20065155.
- L. Ciotti. Stellar systems following the $R \propto 1/m$ luminosity law. *A&A* , 249:99–106, September 1991.
- L. Ciotti and G. Bertin. Analytical properties of the $R^{1/m}$ law. *A&A* , 352: 447–451, December 1999.
- L. Ciotti and B. Lanzoni. Stellar systems following the $R^{1/m}$ luminosity law. II. Anisotropy, velocity profiles, and the fundamental plane of elliptical galaxies. *A&A* , 321:724–732, May 1997.
- L. Ciotti, B. Lanzoni, and A. Renzini. The tilt of the fundamental plane of elliptical galaxies - I. Exploring dynamical and structural effects. *MNRAS* , 282:1–12, September 1996.
- L. Ciotti, B. Lanzoni, and M. Volonteri. The Importance of Dry and Wet Merging on the Formation and Evolution of Elliptical Galaxies. *ApJ* , 658: 65–77, March 2007. doi: 10.1086/510773.
- S. Cole. Modeling galaxy formation in evolving dark matter halos. *ApJ* , 367:45–53, January 1991. doi: 10.1086/169600.
- S. Cole and N. Kaiser. Sunyaev-Zel’dovich fluctuations in the cold dark matter scenario. *MNRAS* , 233:637–648, August 1988.
- S. Cole and C. Lacey. The structure of dark matter haloes in hierarchical clustering models. *MNRAS* , 281:716–+, July 1996.
- L. L. Cowie and A. Songaila. Thermal evaporation of gas within galaxies by a hot intergalactic medium. *Nature* , 266:501–503, April 1977.
- C. C. Dantas, H. V. Capelato, R. R. de Carvalho, and A. L. B. Ribeiro. Dissipationless collapse of spherical protogalaxies and the fundamental plane. *A&A* , 384:772–779, March 2002. doi: 10.1051/0004-6361:20020073.

- C. C. Dantas, H. V. Capelato, A. L. B. Ribeiro, and R. R. de Carvalho. ‘Fundamental Plane’-like relations from collisionless stellar dynamics: a comparison of mergers and collapses. *MNRAS* , 340:398–410, April 2003. doi: 10.1046/j.1365-8711.2003.06272.x.
- J. K. Davies. *Photometric monitoring of early type emission line stars*. PhD thesis, AA(Council for National Academic Awards (England).), 1988.
- R. L. Davies and G. Illingworth. Dynamics of yet more ellipticals and bulges. *ApJ* , 266:516–530, March 1983. doi: 10.1086/160799.
- W. J. G. de Blok and S. S. McGaugh. The dark and visible matter content of low surface brightness disc galaxies. *MNRAS* , 290:533–552, September 1997.
- G. De Lucia, V. Springel, S. D. M. White, D. Croton, and G. Kauffmann. The formation history of elliptical galaxies. *MNRAS* , 366:499–509, February 2006. doi: 10.1111/j.1365-2966.2005.09879.x.
- R. De Propris, M. Colless, J. A. Peacock, W. J. Couch, S. P. Driver, M. L. Balogh, I. K. Baldry, C. M. Baugh, J. Bland-Hawthorn, T. Bridges, R. Cannon, S. Cole, C. Collins, N. Cross, G. Dalton, G. Efstathiou, R. S. Ellis, C. S. Frenk, K. Glazebrook, E. Hawkins, C. Jackson, O. Lahav, I. Lewis, S. Lumsden, S. Maddox, D. Madgwick, P. Norberg, W. Percival, B. A. Peterson, W. Sutherland, and K. Taylor. The 2dF Galaxy Redshift Survey: the blue galaxy fraction and implications for the Butcher-Oemler effect. *MNRAS* , 351:125–132, June 2004. doi: 10.1111/j.1365-2966.2004.07756.x.
- G. de Vaucouleurs. Recherches sur les Nebuleuses Extragalactiques. *Annales d’Astrophysique*, 11:247–+, January 1948.
- G. de Vaucouleurs. Integrated Colors of Bright Galaxies in the u, b, V System. *ApJS* , 5:233–+, January 1961.
- W. Dehnen. Towards optimal softening in three-dimensional N-body codes - I. Minimizing the force error. *MNRAS* , 324:273–291, June 2001.
- A. Diaferio, G. Kauffmann, M. L. Balogh, S. D. M. White, D. Schade, and E. Ellingson. The spatial and kinematic distributions of cluster galaxies in a Λ CDM universe: comparison with observations. *MNRAS* , 323:999–1015, May 2001. doi: 10.1046/j.1365-8711.2001.04303.x.

- G. Djorgovski and B. X. Santiago. The Meaning and the Implications of the Fundamental Plane. In I. J. Danziger, W. W. Zeilinger, and K. Kjaer, editors, *Structure, Dynamics and Chemical Evolution of Elliptical Galaxies*, pages 59–+, 1993.
- S. Djorgovski and M. Davis. Fundamental properties of elliptical galaxies. *ApJ*, 313:59–68, February 1987. doi: 10.1086/164948.
- E. D’Onghia, M. Mapelli, and B. Moore. Merger and ring galaxy formation rates at $z <= 2$. *MNRAS*, 389:1275–1283, September 2008. doi: 10.1111/j.1365-2966.2008.13625.x.
- M. D’Onofrio, M. Capaccioli, and N. Caon. On the Shape of the Light Profiles of Early Type Galaxies - Part Two - the - Diagram. *MNRAS*, 271:523–+, December 1994.
- A. Dressler. Galaxy morphology in rich clusters - Implications for the formation and evolution of galaxies. *ApJ*, 236:351–365, March 1980. doi: 10.1086/157753.
- A. Dressler, D. Lynden-Bell, D. Burstein, R. L. Davies, S. M. Faber, R. Terlevich, and G. Wegner. Spectroscopy and photometry of elliptical galaxies. I - A new distance estimator. *ApJ*, 313:42–58, February 1987. doi: 10.1086/164947.
- A. Dressler, A. J. Oemler, W. J. Couch, I. Smail, R. S. Ellis, A. Barger, H. Butcher, B. M. Poggianti, and R. M. Sharples. Evolution since $Z = 0.5$ of the Morphology-Density Relation for Clusters of Galaxies. *ApJ*, 490:577–+, December 1997. doi: 10.1086/304890.
- J. Dubinski and R. G. Carlberg. The structure of cold dark matter halos. *ApJ*, 378:496–503, September 1991. doi: 10.1086/170451.
- A. S. Eddington. On the radiative equilibrium of the stars. *MNRAS*, 77:16–35, November 1916.
- G. Efstathiou and J. Gorgas. Line-Strength Gradients in NGC5813. *MNRAS*, 215:37P–+, July 1985.
- D. J. Eisenstein and P. Hut. HOP: A New Group-Finding Algorithm for N-Body Simulations. *ApJ*, 498:137–+, May 1998. doi: 10.1086/305535.
- D. M. Elmegreen, B. G. Elmegreen, J. A. Frogel, P. B. Eskridge, R. W. Pogge, A. Gallagher, and J. Iams. Arm Structure in Anemic Spiral Galaxies. *AJ*, 124:777–781, August 2002. doi: 10.1086/341613.

- A. E. Evrard, F. J. Summers, and M. Davis. Two-fluid simulations of galaxy formation. *ApJ* , 422:11–36, February 1994. doi: 10.1086/173700.
- E. A. Evstigneeva, R. R. de Carvalho, A. L. Ribeiro, and H. V. Capelato. Merging of low-mass systems and the origin of the Fundamental Plane. *MNRAS* , 349:1052–1058, April 2004. doi: 10.1111/j.1365-2966.2004.07583.x.
- S. M. Faber. *The Evolution of Galaxies and Stellar Populations*. 1977.
- S. M. Faber and R. E. Jackson. Velocity dispersions and mass-to-light ratios for elliptical galaxies. *ApJ* , 204:668–683, March 1976.
- S. M. Faber, S. Tremaine, E. A. Ajhar, Y.-I. Byun, A. Dressler, K. Gebhardt, C. Grillmair, J. Kormendy, T. R. Lauer, and D. Richstone. The Centers of Early-Type Galaxies with HST. IV. Central Parameter Relations. *AJ* , 114:1771–+, November 1997. doi: 10.1086/118606.
- S. M. Faber, J.-S. Huang, K. G. Noeske, K. Bundy, DEEP2 Team, IRAC GTO Team, and Palomar K-band Team. IRAC and K-band Colors of Galaxies as a Function of Redshift. In *Bulletin of the American Astronomical Society*, volume 37 of *Bulletin of the American Astronomical Society*, pages 1298–+, December 2005.
- S. M. Fall and G. Efstathiou. Formation and rotation of disc galaxies with haloes. *MNRAS* , 193:189–206, October 1980.
- M. A. Fardal, N. Katz, J. P. Gardner, L. Hernquist, D. H. Weinberg, and R. Davé. Cooling Radiation and the Ly α Luminosity of Forming Galaxies. *ApJ* , 562:605–617, December 2001. doi: 10.1086/323519.
- R. Farouki and S. L. Shapiro. Computer simulations of environmental influences on galaxy evolution in dense clusters. II - Rapid tidal encounters. *ApJ* , 243:32–41, January 1981. doi: 10.1086/158563.
- R. T. Farouki and S. L. Shapiro. Simulations of merging disk galaxies. *ApJ* , 259:103–115, August 1982. doi: 10.1086/160151.
- G. Fasano, B. M. Poggianti, W. J. Couch, D. Bettoni, P. Kjærgaard, and M. Moles. The Evolution of the Galactic Morphological Types in Clusters. *ApJ* , 542:673–683, October 2000. doi: 10.1086/317047.
- C. Firmani and V. Avila-Reese. Disc galaxy evolution models in a hierarchical formation scenario: structure and dynamics. *MNRAS* , 315:457–472, July 2000.

- C. Firmani and V. Avila-Reese. Physical processes behind the morphological Hubble sequence. In V. Avila-Reese, C. Firmani, C. S. Frenk, and C. Allen, editors, *Revista Mexicana de Astronomia y Astrofisica Conference Series*, volume 17 of *Revista Mexicana de Astronomia y Astrofisica Conference Series*, pages 107–120, June 2003.
- C. Firmani and A. V. Tutukov. Bursting and stationary star formation in disks and nuclei of galaxies. *A&A* , 288:713–730, August 1994.
- R. A. Flores and J. R. Primack. Observational and theoretical constraints on singular dark matter halos. *ApJL* , 427:L1–L4, May 1994. doi: 10.1086/187350.
- C. S. Frenk, A. E. Evrard, S. D. M. White, and F. J. Summers. Galaxy Dynamics in Clusters. *ApJ* , 472:460–+, December 1996. doi: 10.1086/178079.
- Y. Fujita. Quantitative Estimates of Environmental Effects on the Star Formation Rate of Disk Galaxies in Clusters of Galaxies. *ApJ* , 509:587–594, December 1998. doi: 10.1086/306518.
- M. Fukugita, K. Shimasaku, and T. Ichikawa. Galaxy Colors in Various Photometric Band Systems. *PASP*, 107:945–+, October 1995.
- T. Fukushige and J. Makino. On the Origin of Cusps in Dark Matter Halos. *ApJL* , 477:L9+, March 1997. doi: 10.1086/310516.
- T. Fukushige and J. Makino. Structure of Dark Matter Halos from Hierarchical Clustering. *ApJ* , 557:533–545, August 2001. doi: 10.1086/321666.
- T. Fukushige and J. Makino. Structure of Dark Matter Halos from Hierarchical Clustering. II. Dependence of Cosmological Models in Cluster-sized Halos. *ApJ* , 588:674–679, May 2003. doi: 10.1086/374206.
- G. Gavazzi, K. O’Neil, A. Boselli, and W. van Driel. H I observations of galaxies. II. The Coma Supercluster. *A&A* , 449:929–935, April 2006. doi: 10.1051/0004-6361:20053844.
- J. M. Gelb and E. Bertschinger. Cold dark matter. 1: The formation of dark halos. *ApJ* , 436:467–490, December 1994. doi: 10.1086/174922.
- O. E. Gerhard. N-body simulations of disc-halo galaxies - Isolated systems, tidal interactions and merging. *MNRAS* , 197:179–208, October 1981.
- O. E. Gerhard. Intrinsic principal axes twists in N-body models of elliptical galaxies. *MNRAS* , 203:19P–23P, April 1983.

- O. E. Gerhard and S. M. Fall. Tidal interactions of disc galaxies. *MNRAS* , 203:1253–1268, June 1983.
- S. Ghigna, B. Moore, F. Governato, G. Lake, T. Quinn, and J. Stadel. Dark matter haloes within clusters. *MNRAS* , 300:146–162, October 1998.
- S. Ghigna, B. Moore, F. Governato, G. Lake, T. Quinn, and J. Stadel. Density Profiles and Substructure of Dark Matter Halos: Converging Results at Ultra-High Numerical Resolution. *ApJ* , 544:616–628, December 2000. doi: 10.1086/317221.
- S. P. D. Gill, A. Knebe, and B. K. Gibson. The evolution of substructure - I. A new identification method. *MNRAS* , 351:399–409, June 2004. doi: 10.1111/j.1365-2966.2004.07786.x.
- R. A. Gingold and J. J. Monaghan. Smoothed particle hydrodynamics - Theory and application to non-spherical stars. *MNRAS* , 181:375–389, November 1977.
- O. Y. Gnedin. Dynamical Evolution of Galaxies in Clusters. *ApJ* , 589: 752–769, June 2003. doi: 10.1086/374774.
- T. Goto, C. Yamauchi, Y. Fujita, S. Okamura, M. Sekiguchi, I. Smail, M. Bernardi, and P. L. Gomez. The morphology-density relation in the Sloan Digital Sky Survey. *MNRAS* , 346:601–614, December 2003. doi: 10.1046/j.1365-2966.2003.07114.x.
- F. Governato, B. Willman, L. Mayer, A. Brooks, G. Stinson, O. Valenzuela, J. Wadsley, and T. Quinn. Forming disc galaxies in Λ CDM simulations. *MNRAS* , 374:1479–1494, February 2007. doi: 10.1111/j.1365-2966.2006.11266.x.
- F. Governato, L. Mayer, and C. Brook. The Formation of Galaxy Disks. *ArXiv e-prints*, January 2008.
- A. Graham and M. Colless. Some effects of galaxy structure and dynamics on the Fundamental Plane. *MNRAS* , 287:221–239, May 1997.
- A. Graham, T. R. Lauer, M. Colless, and M. Postman. Brightest Cluster Galaxy Profile Shapes. *ApJ* , 465:534–+, July 1996. doi: 10.1086/177440.
- A. W. Graham and R. Guzmán. HST Photometry of Dwarf Elliptical Galaxies in Coma, and an Explanation for the Alleged Structural Dichotomy between Dwarf and Bright Elliptical Galaxies. *AJ* , 125:2936–2950, June 2003a. doi: 10.1086/374992.

- A. W. Graham and R. Guzmán. HST Photometry of Dwarf Elliptical Galaxies in Coma, and an Explanation for the Alleged Structural Dichotomy between Dwarf and Bright Elliptical Galaxies. *AJ* , 125:2936–2950, June 2003b. doi: 10.1086/374992.
- A. W. Graham, D. Merritt, B. Moore, J. Diemand, and B. Terzić. Empirical Models for Dark Matter Halos. III. The Kormendy Relation and the $\log \rho_e - \log R_e$ Relation. *AJ* , 132:2711–2716, December 2006a. doi: 10.1086/508992.
- A. W. Graham, D. Merritt, B. Moore, J. Diemand, and B. Terzić. Empirical Models for Dark Matter Halos. II. Inner Profile Slopes, Dynamical Profiles, and ρ/σ^3 . *AJ* , 132:2701–2710, December 2006b. doi: 10.1086/508990.
- J. E. Gunn and J. R. I. Gott. On the Infall of Matter Into Clusters of Galaxies and Some Effects on Their Evolution. *ApJ* , 176:1–+, August 1972.
- L. Hernquist. An analytical model for spherical galaxies and bulges. *ApJ* , 356:359–364, June 1990. doi: 10.1086/168845.
- L. Hernquist. Structure of merger remnants. II - Progenitors with rotating bulges. *ApJ* , 409:548–562, June 1993a. doi: 10.1086/172686.
- L. Hernquist. N-body realizations of compound galaxies. *ApJS* , 86:389–400, June 1993b. doi: 10.1086/191784.
- L. Hernquist and N. Katz. TREESPH - A unification of SPH with the hierarchical tree method. *ApJS* , 70:419–446, June 1989. doi: 10.1086/191344.
- L. Hernquist and J. C. Mihos. Excitation of Activity in Galaxies by Minor Mergers. *ApJ* , 448:41–+, July 1995. doi: 10.1086/175940.
- L. Hernquist and D. N. Spergel. Formation of shells in major mergers. *ApJL* , 399:L117–L120, November 1992. doi: 10.1086/186621.
- D. W. Hogg, M. R. Blanton, D. J. Eisenstein, J. E. Gunn, D. J. Schlegel, I. Zehavi, N. A. Bahcall, J. Brinkmann, I. Csabai, D. P. Schneider, D. H. Weinberg, and D. G. York. The Overdensities of Galaxy Environments as a Function of Luminosity and Color. *ApJL* , 585:L5–L9, March 2003. doi: 10.1086/374238.
- P. F. Hopkins, T. J. Cox, and L. Hernquist. Dissipation and the Fundamental Plane: Observational Tests. *ArXiv e-prints*, June 2008a.

- P. F. Hopkins, T. J. Cox, J. D. Younger, and L. Hernquist. How Do Disks Survive Mergers? *ArXiv e-prints*, 806, June 2008b.
- T. P. Idiart, R. Michard, and J. A. de Freitas Pacheco. New UBVRI color distributions in E-type galaxies. II. Central and mean metallicities color distributions in E-type galaxies. II. *A&A* , 398:949–957, February 2003. doi: 10.1051/0004-6361:20021718.
- D. Iono, M. S. Yun, and J. C. Mihos. Radial Gas Flows in Colliding Galaxies: Connecting Simulations and Observations. *ApJ* , 616:199–220, November 2004. doi: 10.1086/424797.
- W. Jaffe. The Envelopes of Spherical Galaxies. In P. T. de Zeeuw, editor, *Structure and Dynamics of Elliptical Galaxies*, volume 127 of *IAU Symposium*, pages 511–+, 1987.
- A. Jenkins, C. S. Frenk, F. R. Pearce, P. A. Thomas, R. Hutchings, J. M. Colberg, S. D. M. White, H. M. P. Couchman, J. A. Paacock, G. P. Efstathiou, and A. H. Nelson. The Virgo consortium: simulations of dark matter and galaxy clustering. In M. Persic and P. Salucci, editors, *Dark and Visible Matter in Galaxies and Cosmological Implications*, volume 117 of *Astronomical Society of the Pacific Conference Series*, pages 348–+, 1997.
- I. Jorgensen, M. Franx, and P. Kjaergaard. The Fundamental Plane for cluster E and S0 galaxies. *MNRAS* , 280:167–185, May 1996.
- N. Kashikawa, M. Sekiguchi, M. Doi, Y. Komiyama, S. Okamura, K. Shimasaku, M. Yagi, and N. Yasuda. The Morphology Dependence of Luminosity Segregation in the Coma Cluster. *ApJ* , 500:750–+, June 1998. doi: 10.1086/305758.
- N. Katz and J. E. Gunn. Dissipational galaxy formation. I - Effects of gas-dynamics. *ApJ* , 377:365–381, August 1991. doi: 10.1086/170367.
- N. Katz, L. Hernquist, and D. H. Weinberg. Galaxies and gas in a cold dark matter universe. *ApJL* , 399:L109–L112, November 1992. doi: 10.1086/186619.
- N. Katz, D. H. Weinberg, and L. Hernquist. Cosmological Simulations with TreeSPH. *ApJS* , 105:19–+, July 1996. doi: 10.1086/192305.
- G. Kauffmann, S. D. M. White, and B. Guiderdoni. The Formation and Evolution of Galaxies Within Merging Dark Matter Haloes. *MNRAS* , 264:201–+, September 1993.

- T. Kaufmann, L. Mayer, J. Wadsley, J. Stadel, and B. Moore. Cooling flows within galactic haloes: the kinematics and properties of infalling multi-phase gas. *MNRAS* , 370:1612–1622, August 2006. doi: 10.1111/j.1365-2966.2006.10599.x.
- T. Kaufmann, L. Mayer, J. Wadsley, J. Stadel, and B. Moore. Angular momentum transport and disc morphology in smoothed particle hydrodynamics simulations of galaxy formation. *MNRAS* , 375:53–67, February 2007. doi: 10.1111/j.1365-2966.2006.11314.x.
- D. Kawata. Effects of Type II and Type Ia Supernovae Feedback on the Chemodynamical Evolution of Elliptical Galaxies. *ApJ* , 558:598–614, September 2001. doi: 10.1086/322309.
- W. C. Keel, R. C. Kennicutt, Jr., E. Hummel, and J. M. van der Hulst. The effects of interactions on spiral galaxies. I - Nuclear activity and star formation. *AJ* , 90:708–730, May 1985. doi: 10.1086/113779.
- R. C. Kennicutt, Jr., K. A. Roettiger, W. C. Keel, J. M. van der Hulst, and E. Hummel. The effects of interactions on spiral galaxies. II - Disk star-formation rates. *AJ* , 93:1011–1023, May 1987. doi: 10.1086/114384.
- R. C. Kennicutt, Jr., P. Tamblyn, and C. E. Congdon. Past and future star formation in disk galaxies. *ApJ* , 435:22–36, November 1994. doi: 10.1086/174790.
- D. Kereš, N. Katz, D. H. Weinberg, and R. Davé. How do galaxies get their gas? *MNRAS* , 363:2–28, October 2005. doi: 10.1111/j.1365-2966.2005.09451.x.
- S. Khochfar and A. Burkert. The Importance of Spheroidal and Mixed Mergers for Early-Type Galaxy Formation. *ApJL* , 597:L117–L120, November 2003. doi: 10.1086/379845.
- I. King. The structure of star clusters. I. an empirical density law. *AJ* , 67:471–+, October 1962.
- A. Klypin, A. V. Kravtsov, O. Valenzuela, and F. Prada. Where Are the Missing Galactic Satellites? *ApJ* , 522:82–92, September 1999. doi: 10.1086/307643.
- A. Knebe, A. Green, and J. Binney. Multi-level adaptive particle mesh (MLAPM): a c code for cosmological simulations. *MNRAS* , 325:845–864, August 2001. doi: 10.1046/j.1365-8711.2001.04532.x.

- T. Kodama and N. Arimoto. Origin of the colour-magnitude relation of elliptical galaxies. *A&A* , 320:41–53, April 1997.
- J. Kormendy. Brightness distributions in compact and normal galaxies. II - Structure parameters of the spheroidal component. *ApJ* , 218:333–346, December 1977.
- J. Kormendy and R. C. Kennicutt, Jr. Secular Evolution and the Formation of Pseudobulges in Disk Galaxies. *ARA&A*, 42:603–683, September 2004.
- F. La Barbera, P. Merluzzi, G. Busarello, M. Massarotti, and A. Mercurio. Probing galaxy evolution through the internal colour gradients, the Kormendy relations and the Photometric Plane of cluster galaxies at $z\sim 0.2$. *A&A* , 425:797–812, October 2004. doi: 10.1051/0004-6361:20047157.
- F. La Barbera, G. Busarello, P. Merluzzi, I. de la Rosa, G. Coppola, and C. P. Haines. The SDSS-UKIDSS Fundamental Plane of Early-type Galaxies. *ArXiv e-prints*, July 2008.
- C. Lacey and S. Cole. Merger rates in hierarchical models of galaxy formation. *MNRAS* , 262:627–649, June 1993.
- C. Lacey and J. Silk. Tidally triggered galaxy formation. I - Evolution of the galaxy luminosity function. *ApJ* , 381:14–32, November 1991. doi: 10.1086/170625.
- G. Lake, N. Katz, and B. Moore. The Formation of Quasars in Low-Luminosity Hosts via Galaxy Harassment. *ApJ* , 495:152–+, March 1998. doi: 10.1086/305265.
- R. B. Larson. Effects of supernovae on the early evolution of galaxies. *MNRAS* , 169:229–246, November 1974a.
- R. B. Larson. Dynamical models for the formation and evolution of spherical galaxies. *MNRAS* , 166:585–616, March 1974b.
- R. B. Larson, B. M. Tinsley, and C. N. Caldwell. The evolution of disk galaxies and the origin of S0 galaxies. *ApJ* , 237:692–707, May 1980. doi: 10.1086/157917.
- J. Loveday, G. Efstathiou, B. A. Peterson, and S. J. Maddox. Large-scale structure in the universe - Results from the Stromlo-APM redshift survey. *ApJL* , 400:L43–L46, December 1992. doi: 10.1086/186645.

- L. B. Lucy. A numerical approach to the testing of the fission hypothesis. *AJ* , 82:1013–1024, December 1977.
- A. H. Maller, A. Dekel, and R. Somerville. Modelling angular-momentum history in dark-matter haloes. *MNRAS* , 329:423–430, January 2002. doi: 10.1046/j.1365-8711.2002.04983.x.
- M. Masjedi, D. W. Hogg, and M. R. Blanton. The Growth of Luminous Red Galaxies by Merging. *ApJ* , 679:260–268, May 2008. doi: 10.1086/586696.
- B. Mathiesen and A. E. Evrard. Constraints on Ω_0 and cluster evolution using the ROSAT $\log N - \log S$ relation. *MNRAS* , 295:769–780, April 1998.
- L. Mayer, F. Governato, and T. Kaufmann. The formation of disk galaxies in computer simulations. *ArXiv e-prints*, January 2008.
- R. M. McDermid, E. Emsellem, K. L. Shapiro, R. Bacon, M. Bureau, M. Cappellari, R. L. Davies, T. de Zeeuw, J. Falcón-Barroso, D. Krajnović, H. Kuntschner, R. F. Peletier, and M. Sarzi. The SAURON project - VIII. OASIS/CFHT integral-field spectroscopy of elliptical and lenticular galaxy centres. *MNRAS* , 373:906–958, December 2006. doi: 10.1111/j.1365-2966.2006.11065.x.
- A. Mercurio, P. Merluzzi, C. P. Haines, A. Gargiulo, N. Krusanova, G. Busarello, F. L. Barbera, M. Capaccioli, and G. Covone. Shapley Optical Survey - I. Luminosity functions in the supercluster environment. *MNRAS* , 368:109–120, May 2006. doi: 10.1111/j.1365-2966.2006.10106.x.
- D. Merritt. Relaxation and tidal stripping in rich clusters of galaxies. I - Evolution of the mass distribution. *ApJ* , 264:24–48, January 1983. doi: 10.1086/160571.
- D. Merritt. Optimal Smoothing for N-Body Codes. *AJ* , 111:2462–+, June 1996. doi: 10.1086/117980.
- D. Merritt, J. F. Navarro, A. Ludlow, and A. Jenkins. A Universal Density Profile for Dark and Luminous Matter? *ApJL* , 624:L85–L88, May 2005. doi: 10.1086/430636.
- J. C. Mihos and L. Hernquist. Star-forming galaxy models: Blending star formation into TREESPH. *ApJ* , 437:611–624, December 1994. doi: 10.1086/175025.

- J. C. Mihos and L. Hernquist. Gasdynamics and Starbursts in Major Mergers. *ApJ* , 464:641–+, June 1996. doi: 10.1086/177353.
- J. C. Mihos, D. O. Richstone, and G. D. Bothun. Models of star formation in interacting and merging disk galaxies. *ApJ* , 400:153–162, November 1992. doi: 10.1086/171980.
- R. H. Miller and B. F. Smith. Galaxy collisions - A preliminary study. *ApJ* , 235:421–436, January 1980. doi: 10.1086/157646.
- H. J. Mo and S. D. M. White. An analytic model for the spatial clustering of dark matter haloes. *MNRAS* , 282:347–361, September 1996.
- H. J. Mo, Y. P. Jing, and S. D. M. White. The correlation function of clusters of galaxies and the amplitude of mass fluctuations in the Universe. *MNRAS* , 282:1096–1104, October 1996.
- H. J. Mo, S. Mao, and S. D. M. White. The formation of galactic discs. *MNRAS* , 295:319–336, April 1998.
- J. J. Monaghan. Smoothed particle hydrodynamics. *ARA&A*, 30:543–574, 1992. doi: 10.1146/annurev.aa.30.090192.002551.
- B. Moore. Evidence against Dissipationless Dark Matter from Observations of Galaxy Haloes. *Nature* , 370:629–+, August 1994. doi: 10.1038/370629a0.
- B. Moore, N. Katz, G. Lake, A. Dressler, and A. Oemler. Galaxy harassment and the evolution of clusters of galaxies. *Nature* , 379:613–616, February 1996. doi: 10.1038/379613a0.
- B. Moore, G. Lake, and N. Katz. Morphological Transformation from Galaxy Harassment. *ApJ* , 495:139–+, March 1998. doi: 10.1086/305264.
- B. Moore, S. Ghigna, F. Governato, G. Lake, T. Quinn, J. Stadel, and P. Tozzi. Dark Matter Substructure within Galactic Halos. *ApJL* , 524:L19–L22, October 1999. doi: 10.1086/312287.
- M. Mori and A. Burkert. Gas Stripping of Dwarf Galaxies in Clusters of Galaxies. *ApJ* , 538:559–568, August 2000. doi: 10.1086/309140.
- T. Naab and A. Burkert. Statistical Properties of Collisionless Equal- and Unequal-Mass Merger Remnants of Disk Galaxies. *ApJ* , 597:893–906, November 2003. doi: 10.1086/378581.

- R. Narayan and S. D. M. White. Gravitational lensing in a cold dark matter universe. *MNRAS* , 231:97P–+, April 1988.
- J. F. Navarro, C. S. Frenk, and S. D. M. White. The assembly of galaxies in a hierarchically clustering universe. *MNRAS* , 275:56–66, July 1995.
- J. F. Navarro, C. S. Frenk, and S. D. M. White. A Universal Density Profile from Hierarchical Clustering. *ApJ* , 490:493–+, December 1997. doi: 10.1086/304888.
- J. F. Navarro, E. Hayashi, C. Power, A. R. Jenkins, C. S. Frenk, S. D. M. White, V. Springel, J. Stadel, and T. R. Quinn. The inner structure of Λ CDM haloes - III. Universality and asymptotic slopes. *MNRAS* , 349:1039–1051, April 2004. doi: 10.1111/j.1365-2966.2004.07586.x.
- J. Negroponte and S. D. M. White. Simulations of mergers between disc-halo galaxies. *MNRAS* , 205:1009–1029, December 1983.
- C. Nipoti, P. Londrillo, and L. Ciotti. Galaxy merging, the fundamental plane of elliptical galaxies and the $M_{BH} - \sigma_0$ relation. *MNRAS* , 342:501–512, June 2003. doi: 10.1046/j.1365-8711.2003.06554.x.
- T. Okamoto and M. Nagashima. Morphology-Density Relation for Simulated Clusters of Galaxies in Cold Dark Matter-dominated Universes. *ApJ* , 547:109–116, January 2001. doi: 10.1086/318375.
- J. P. Ostriker and S. D. Tremaine. Another evolutionary correction to the luminosity of giant galaxies. *ApJL* , 202:L113–L117, December 1975.
- M. A. Pahre, S. G. Djorgovski, and R. R. de Carvalho. The Near-Infrared Fundamental Plane of Elliptical Galaxies. *ApJL* , 453:L17+, November 1995. doi: 10.1086/309740.
- M. A. Pahre, R. R. de Carvalho, and S. G. Djorgovski. Near-Infrared Imaging of Early-Type Galaxies. IV. The Physical Origins of the Fundamental Plane Scaling Relations. *AJ* , 116:1606–1625, October 1998. doi: 10.1086/300545.
- P. J. E. Peebles. Origin of the Angular Momentum of Galaxies. *ApJ* , 155:393–+, February 1969.
- R. F. Peletier, R. L. Davies, G. D. Illingworth, L. E. Davis, and M. Cawson. CCD surface photometry of galaxies with dynamical data. II - UBR photometry of 39 elliptical galaxies. *AJ* , 100:1091–1142, October 1990. doi: 10.1086/115582.

- M. Persic, P. Salucci, and F. Stel. The universal rotation curve of spiral galaxies - I. The dark matter connection. *MNRAS* , 281:27–47, July 1996.
- A. Pizzella, E. M. Corsini, E. Dalla Bontà, M. Sarzi, L. Coccato, and F. Bertola. On the Relation between Circular Velocity and Central Velocity Dispersion in High and Low Surface Brightness Galaxies. *ApJ* , 631:785–791, October 2005. doi: 10.1086/430513.
- B. M. Poggianti, T. J. Bridges, D. Carter, B. Mobasher, M. Doi, M. Iye, N. Kashikawa, Y. Komiyama, S. Okamura, M. Sekiguchi, K. Shimasaku, M. Yagi, and N. Yasuda. Ages of S0 and Elliptical Galaxies in the Coma Cluster. *ApJ* , 563:118–123, December 2001. doi: 10.1086/323767.
- M. Postman and M. J. Geller. The morphology-density relation - The group connection. *ApJ* , 281:95–99, June 1984. doi: 10.1086/162078.
- M. Postman, M. Franx, N. J. G. Cross, B. Holden, H. C. Ford, G. D. Illingworth, T. Goto, R. Demarco, P. Rosati, J. P. Blakeslee, K.-V. Tran, N. Benítez, M. Clampin, G. F. Hartig, N. Homeier, D. R. Ardila, F. Bartko, R. J. Bouwens, L. D. Bradley, T. J. Broadhurst, R. A. Brown, C. J. Burrows, E. S. Cheng, P. D. Feldman, D. A. Golimowski, C. Gronwall, L. Infante, R. A. Kimble, J. E. Krist, M. P. Lesser, A. R. Martel, S. Mei, F. Menanteau, G. R. Meurer, G. K. Miley, V. Motta, M. Sirianni, W. B. Sparks, H. D. Tran, Z. I. Tsvetanov, R. L. White, and W. Zheng. The Morphology-Density Relation in $z \sim 1$ Clusters. *ApJ* , 623:721–741, April 2005. doi: 10.1086/428881.
- F. Prada, A. A. Klypin, E. Simonneau, J. Betancort-Rijo, S. Patiri, S. Gottlöber, and M. A. Sanchez-Conde. How Far Do They Go? The Outer Structure of Galactic Dark Matter Halos. *ApJ* , 645:1001–1011, July 2006. doi: 10.1086/504456.
- W. H. Press and P. Schechter. Formation of Galaxies and Clusters of Galaxies by Self-Similar Gravitational Condensation. *ApJ* , 187:425–438, February 1974.
- P. Prugniel and F. Simien. The fundamental plane of early-type galaxies: non-homology of the spatial structure. *A&A* , 321:111–122, May 1997.
- V. Quilis, B. Moore, and R. Bower. Gone with the Wind: The Origin of S0 Galaxies in Clusters. *Science*, 288:1617–1620, June 2000.
- P. J. Quinn, L. Hernquist, and D. P. Fullagar. Heating of galactic disks by mergers. *ApJ* , 403:74–93, January 1993. doi: 10.1086/172184.

- B. Robertson, J. S. Bullock, T. J. Cox, T. Di Matteo, L. Hernquist, V. Springel, and N. Yoshida. A Merger-driven Scenario for Cosmological Disk Galaxy Formation. *ApJ* , 645:986–1000, July 2006. doi: 10.1086/504412.
- N. Roos and C. A. Norman. Galaxy collisions and their influence on the dynamics and evolution of groups and clusters of galaxies. *A&A* , 76: 75–85, June 1979.
- S. Sabatini, J. Davies, W. van Driel, M. Baes, S. Roberts, R. Smith, S. Linder, and K. O’Neil. The dwarf low surface brightness galaxy population of the Virgo Cluster - II. Colours and HI line observations. *MNRAS* , 357:819–833, March 2005. doi: 10.1111/j.1365-2966.2005.08608.x.
- R. P. Saglia, C. Maraston, L. Greggio, R. Bender, and B. Ziegler. The evolution of the color gradients of early-type cluster galaxies. *A&A* , 360: 911–934, August 2000.
- P. Salucci, A. Lapi, C. Tonini, G. Gentile, I. Yegorova, and U. Klein. The universal rotation curve of spiral galaxies - II. The dark matter distribution out to the virial radius. *MNRAS* , 378:41–47, June 2007. doi: 10.1111/j.1365-2966.2007.11696.x.
- M. T. Sargent, C. M. Carollo, S. J. Lilly, C. Scarlata, R. Feldmann, P. Kampczyk, A. M. Koekemoer, N. Scoville, J.-P. Kneib, A. Leauthaud, R. Massey, J. Rhodes, L. A. M. Tasca, P. Capak, H. J. McCracken, C. Porciani, A. Renzini, Y. Taniguchi, D. J. Thompson, and K. Sheth. The Evolution of the Number Density of Large Disk Galaxies in COSMOS. *ApJS* , 172:434–455, September 2007. doi: 10.1086/516584.
- C. Scannapieco, P. B. Tissera, S. D. M. White, and V. Springel. Effects of Supernova Feedback on the Formation of Galaxy Disks. *ArXiv e-prints*, 804, April 2008.
- S. Schindler, B. Binggeli, and H. Böhringer. Morphology of the Virgo cluster: Gas versus galaxies. *A&A* , 343:420–438, March 1999.
- M. Schmidt. The Rate of Star Formation. *ApJ* , 129:243–+, March 1959.
- F. Schweizer. *Observational Evidence for Interactions and Mergers*, pages 105–274. *Galaxies: Interactions and Induced Star Formation Saas-Fee Advanced Course 26 Lecture Notes 1996*. Kennicutt, R.C., Jr.; Schweizer, F.; Barnes, J.E., p. 105-274, 1996.

- F. Schweizer and P. Seitzer. Remnant of a “Wet” Merger: NGC 34 and Its Young Massive Clusters, Young Stellar Disk, and Strong Gaseous Outflow. *AJ* , 133:2132–2155, May 2007. doi: 10.1086/513317.
- J. L. Sérsic. *Atlas de galaxias australes*. Cordoba, Argentina: Observatorio Astronomico, 1968, 1968.
- S. F. Shandarin and Y. B. Zeldovich. The large-scale structure of the universe: Turbulence, intermittency, structures in a self-gravitating medium. *Reviews of Modern Physics*, 61:185–220, April 1989.
- F. Shankar, A. Lapi, P. Salucci, G. De Zotti, and L. Danese. New Relationships between Galaxy Properties and Host Halo Mass, and the Role of Feedbacks in Galaxy Formation. *ApJ* , 643:14–25, May 2006. doi: 10.1086/502794.
- R. K. Sheth and G. Tormen. Large-scale bias and the peak background split. *MNRAS* , 308:119–126, September 1999.
- J. Silk and M. J. Rees. Quasars and galaxy formation. *A&A* , 331:L1–L4, March 1998.
- G. P. Smith, T. Treu, R. S. Ellis, S. M. Moran, and A. Dressler. Evolution since $z = 1$ of the Morphology-Density Relation for Galaxies. *ApJ* , 620:78–87, February 2005. doi: 10.1086/426930.
- R. S. Somerville and J. R. Primack. Semi-analytic modelling of galaxy formation: the local Universe. *MNRAS* , 310:1087–1110, December 1999.
- J. Sommer-Larsen, M. Götz, and L. Portinari. Galaxy Formation: Cold Dark Matter, Feedback, and the Hubble Sequence. *ApJ* , 596:47–66, October 2003. doi: 10.1086/377685.
- D. N. Spergel. Cosmic Microwave Background: Probing the Universe from $Z = 6 - 1100$. *The Universe at $z > 6$, 26th meeting of the IAU, Joint Discussion 7, 17-18 August 2006, Prague, Czech Republic, JD07, #6, 7*, August 2006.
- V. Springel. The cosmological simulation code GADGET-2. *MNRAS* , 364:1105–1134, December 2005. doi: 10.1111/j.1365-2966.2005.09655.x.
- V. Springel and L. Hernquist. Cosmological smoothed particle hydrodynamics simulations: the entropy equation. *MNRAS* , 333:649–664, July 2002. doi: 10.1046/j.1365-8711.2002.05445.x.

- V. Springel and L. Hernquist. Formation of a Spiral Galaxy in a Major Merger. *ApJL* , 622:L9–L12, March 2005. doi: 10.1086/429486.
- V. Springel, S. D. M. White, G. Tormen, and G. Kauffmann. Populating a cluster of galaxies - I. Results at $z=0$. *MNRAS* , 328:726–750, December 2001. doi: 10.1046/j.1365-8711.2001.04912.x.
- S. Sridhar and R. Nityananda. Time-Dependent Dynamics of a Planar Galaxy Model. *MNRAS* , 245:713–+, August 1990.
- J. G. Stadel. *Cosmological N-body simulations and their analysis*. PhD thesis, AA(UNIVERSITY OF WASHINGTON), 2001.
- M. Stiavelli, B. W. Miller, H. C. Ferguson, J. Mack, B. C. Whitmore, and J. M. Lotz. The Nuclear Cusp Slopes of Dwarf Elliptical Galaxies. *AJ* , 121:1385–1394, March 2001. doi: 10.1086/319425.
- G. Stinson, A. Seth, N. Katz, J. Wadsley, F. Governato, and T. Quinn. Star formation and feedback in smoothed particle hydrodynamic simulations - I. Isolated galaxies. *MNRAS* , 373:1074–1090, December 2006. doi: 10.1111/j.1365-2966.2006.11097.x.
- H. Susa, M. Sasaki, and T. Tanaka. Probability Distribution of Primordial Angular Momentum and Formation of Massive Black Holes. *Progress of Theoretical Physics*, 92:961–+, November 1994.
- N. Tamura and K. Ohta. Color Gradients in Early-Type Galaxies in Clusters at Redshift 0.37-0.56. *AJ* , 120:533–539, August 2000. doi: 10.1086/301460.
- N. Tamura, C. Kobayashi, N. Arimoto, T. Kodama, and K. Ohta. Origin of Color Gradients in Elliptical Galaxies. *AJ* , 119:2134–2145, May 2000. doi: 10.1086/301333.
- B. Thomsen and W. A. Baum. Magnesium gradients in elliptical galaxies. III - Results and interpretation. *ApJ* , 347:214–230, December 1989. doi: 10.1086/168111.
- T. X. Thuan, J.-M. Alimi, J. R. I. Gott, and S. E. Schneider. Northern dwarf and low surface brightness galaxies. IV - The large-scale space distribution. *ApJ* , 370:25–48, March 1991. doi: 10.1086/169791.
- A. Toomre. Gravitational interactions between galaxies. In J. R. Shakeshaft, editor, *The Formation and Dynamics of Galaxies*, volume 58 of *IAU Symposium*, pages 347–363, 1974.

- A. Toomre. Mergers and Some Consequences. In B. M. Tinsley and R. B. Larson, editors, *Evolution of Galaxies and Stellar Populations*, pages 401–+, 1977.
- A. Toomre. What amplifies the spirals. In S. M. Fall and D. Lynden-Bell, editors, *Structure and Evolution of Normal Galaxies*, pages 111–136, 1981.
- G. Tormen, F. R. Bouchet, and S. D. M. White. The structure and dynamical evolution of dark matter haloes. *MNRAS* , 286:865–884, April 1997.
- G. Tormen, A. Diaferio, and D. Syer. Survival of substructure within dark matter haloes. *MNRAS* , 299:728–742, September 1998.
- G. Toth and J. P. Ostriker. Galactic disks, infall, and the global value of Omega. *ApJ* , 389:5–26, April 1992. doi: 10.1086/171185.
- S. C. Trager, S. M. Faber, G. Worthey, and J. J. González. The Stellar Population Histories of Early-Type Galaxies. II. Controlling Parameters of the Stellar Populations. *AJ* , 120:165–188, July 2000. doi: 10.1086/301442.
- K.-V. H. Tran, P. van Dokkum, M. Franx, G. D. Illingworth, D. D. Kelson, and N. M. F. Schreiber. Spectroscopic Confirmation of Multiple Red Galaxy-Galaxy Mergers in MS 1054-03 ($z = 0.83$)1,. *ApJL* , 627:L25–L28, July 2005. doi: 10.1086/432090.
- T. Treu, R. S. Ellis, J.-P. Kneib, A. Dressler, I. Smail, O. Czoske, A. Oemler, and P. Natarajan. A Wide-Field Hubble Space Telescope Study of the Cluster Cl 0024+16 at $z = 0.4$. I. Morphological Distributions to 5 Mpc Radius. *ApJ* , 591:53–78, July 2003. doi: 10.1086/375314.
- I. Trujillo, A. Burkert, and E. F. Bell. The Tilt of the Fundamental Plane: Three-Quarters Structural Nonhomology, One-Quarter Stellar Population. *ApJL* , 600:L39–L42, January 2004. doi: 10.1086/381528.
- S. van den Bergh. A new classification system for galaxies. *ApJ* , 206:883–887, June 1976.
- F. C. van den Bosch. The origin of the density distribution of disc galaxies: a new problem for the standard model of disc formation. *MNRAS* , 327:1334–1352, November 2001. doi: 10.1046/j.1365-8711.2001.04861.x.
- F. C. van den Bosch, A. Burkert, and R. A. Swaters. The angular momentum content of dwarf galaxies: new challenges for the theory of galaxy formation. *MNRAS* , 326:1205–1215, September 2001. doi: 10.1046/j.1365-8711.2001.04656.x.

- P. G. van Dokkum. The Recent and Continuing Assembly of Field Elliptical Galaxies by Red Mergers. *AJ* , 130:2647–2665, December 2005. doi: 10.1086/497593.
- P. G. van Dokkum, M. Franx, D. Fabricant, D. D. Kelson, and G. D. Illingworth. A High Merger Fraction in the Rich Cluster MS 1054-03 at $Z = 0.83$: Direct Evidence for Hierarchical Formation of Massive Galaxies. *ApJL* , 520:L95–L98, August 1999. doi: 10.1086/312154.
- H. Velazquez and S. D. M. White. Sinking satellites and the heating of galaxy discs. *MNRAS* , 304:254–270, April 1999.
- M. A. W. Verheijen. *The Ursa Major Cluster of Galaxies: TF-relations and dark matter*. PhD thesis, PhD thesis, Univ. Groningen, The Netherlands , (1997), 1997.
- N. P. Vogt, M. P. Haynes, R. Giovanelli, and T. Herter. M/L, $H\alpha$ Rotation Curves, and H I Gas Measurements for 329 Nearby Cluster and Field Spirals. III. Evolution in Fundamental Galaxy Parameters. *AJ* , 127:3325–3337, June 2004. doi: 10.1086/420703.
- B. Vollmer, V. Cayatte, C. Balkowski, and W. J. Duschl. Ram Pressure Stripping and Galaxy Orbits: The Case of the Virgo Cluster. *ApJ* , 561:708–726, November 2001. doi: 10.1086/323368.
- J. W. Wadsley, J. Stadel, and T. Quinn. Gasoline: a flexible, parallel implementation of TreeSPH. *New Astronomy*, 9:137–158, February 2004. doi: 10.1016/j.newast.2003.08.004.
- I. R. Walker, J. C. Mihos, and L. Hernquist. Quantifying the Fragility of Galactic Disks in Minor Mergers. *ApJ* , 460:121–+, March 1996. doi: 10.1086/176956.
- M. S. Warren, P. J. Quinn, J. K. Salmon, and W. H. Zurek. Dark halos formed via dissipationless collapse. I - Shapes and alignment of angular momentum. *ApJ* , 399:405–425, November 1992. doi: 10.1086/171937.
- R. H. Wechsler, J. S. Bullock, J. R. Primack, A. V. Kravtsov, and A. Dekel. Concentrations of Dark Halos from Their Assembly Histories. *ApJ* , 568:52–70, March 2002. doi: 10.1086/338765.
- V. Weidemann. The initial-final mass relation - Galactic disk and Magellanic Clouds. *A&A* , 188:74–84, December 1987.

- M. L. Weil, V. R. Eke, and G. Efstathiou. The formation of disc galaxies. *MNRAS* , 300:773–789, November 1998.
- K. E. Whitaker and P. G. van Dokkum. Hubble Space Telescope Images of Red Mergers: How Dry Are They? *ApJL* , 676:L105–L108, April 2008. doi: 10.1086/587516.
- S. D. M. White. Simulations of merging galaxies. *MNRAS* , 184:185–203, July 1978.
- S. D. M. White. Further simulations of merging galaxies. *MNRAS* , 189:831–852, December 1979.
- S. D. M. White. Mixing processes in galaxy mergers. *MNRAS* , 191:1P–4P, April 1980.
- S. D. M. White. Simulations of galaxy mergers. In E. Athanassoula, editor, *Internal Kinematics and Dynamics of Galaxies*, volume 100 of *IAU Symposium*, pages 337–344, 1983.
- S. D. M. White. Dissipationless formation of elliptical galaxies. In P. T. de Zeeuw, editor, *Structure and Dynamics of Elliptical Galaxies*, volume 127 of *IAU Symposium*, pages 339–349, 1987.
- S. D. M. White and C. S. Frenk. Galaxy formation through hierarchical clustering. *ApJ* , 379:52–79, September 1991. doi: 10.1086/170483.
- S. D. M. White and M. J. Rees. Core condensation in heavy halos - A two-stage theory for galaxy formation and clustering. *MNRAS* , 183:341–358, May 1978.
- S. D. M. White, G. Efstathiou, and C. S. Frenk. The amplitude of mass fluctuations in the universe. *MNRAS* , 262:1023–1028, June 1993.
- B. C. Whitmore and D. M. Gilmore. On the interpretation of the morphology-density relation for galaxies in clusters. *ApJ* , 367:64–68, January 1991. doi: 10.1086/169602.
- B. C. Whitmore, D. M. Gilmore, and C. Jones. What determines the morphological fractions in clusters of galaxies? *ApJ* , 407:489–509, April 1993. doi: 10.1086/172531.
- R. E. Williams, B. Blacker, M. Dickinson, W. V. D. Dixon, H. C. Ferguson, A. S. Fruchter, M. Giavalisco, R. L. Gilliland, I. Heyer, R. Katsanis, Z. Levay, R. A. Lucas, D. B. McElroy, L. Petro, M. Postman, H.-M. Adorf,

- and R. Hook. The Hubble Deep Field: Observations, Data Reduction, and Galaxy Photometry. *AJ*, 112:1335–+, October 1996. doi: 10.1086/118105.
- G. Worthey, S. C. Trager, and S. M. Faber. The Galaxian Age-Metallicity Relation. In A. Buzzoni, A. Renzini, and A. Serrano, editors, *ASP Conf. Ser. 86: Fresh Views of Elliptical Galaxies*, pages 203–+, 1996.
- C. K. Young and M. J. Currie. A New Extragalactic Distance Indicator Based on the Surface Brightness Profiles of Dwarf Elliptical Galaxies. *MNRAS*, 268:L11+, May 1994.
- J. D. Younger and G. L. Bryan. Cosmological Simulations of the Pre-heating Scenario for Galaxy Cluster Formation: Comparison to Analytic Models and Observations. *ApJ*, 666:647–657, September 2007. doi: 10.1086/520619.
- J. Zavala, V. Avila-Reese, H. Hernández-Toledo, and C. Firmani. The luminous and dark matter content of disk galaxies. *A&A*, 412:633–650, December 2003. doi: 10.1051/0004-6361:20031135.
- E. Zucca, O. Ilbert, S. Bardelli, L. Tresse, G. Zamorani, S. Arnouts, L. Pozzetti, M. Bolzonella, H. J. McCracken, D. Bottini, B. Garilli, V. Le Brun, O. Le Fèvre, D. Maccagni, J. P. Picat, R. Scaramella, M. Scodeggio, G. Vettolani, A. Zanicelli, C. Adami, M. Arnaboldi, A. Cappi, S. Charlot, P. Ciliegi, T. Contini, S. Foucaud, P. Franzetti, I. Gavignaud, L. Guzzo, A. Iovino, B. Marano, C. Marinoni, A. Mazure, B. Meneux, R. Merighi, S. Paltani, R. Pellò, A. Pollo, M. Radovich, M. Bondi, A. Bongiorno, G. Busarello, O. Cucciati, L. Gregorini, F. Lamareille, G. Mathez, Y. Mellier, P. Merluzzi, V. Ripepi, and D. Rizzo. The VIMOS VLT Deep Survey. Evolution of the luminosity functions by galaxy type up to $z = 1.5$ from first epoch data. *A&A*, 455:879–890, September 2006. doi: 10.1051/0004-6361:20053645.
- M. A. Zwaan, J. M. van der Hulst, W. J. G. de Blok, and S. S. McGaugh. The Tully-Fisher relation for low surface brightness galaxies: implications for galaxy evolution. *MNRAS*, 273:L35–L38, March 1995.